2005

# Non-silicon Microfabricated Nanostructured Chemical Sensors For Electric Nose Application

Jianwei Gong
*University of Central Florida*

# NON-SILICON MICROFABRICATED NANOSTRUCTURED CHEMICAL SENSORS FOR ELECTRIC NOSE APPLICATION

by

JIANWEI GONG
B. S. Beijing Institute of Technology, 1998
M.S. Beijing Institute of Technology, 2001

A dissertation submitted in partial fulfillment of the requirements
for the degree of Doctor of Philosophy
in the Department of Mechanical, Materials, and Aerospace Engineering
in the College of Engineering and Computer Science
at the University of Central Florida
Orlando, Florida

Spring Term
2005

Major Professor: Dr. Quanfang Chen

# ABSTRACT

A systematic investigation has been performed for “Electric Nose”, a system that can identify gas samples and detect their concentrations by combining sensor array and data processing technologies.

Non-silicon based microfabricatition has been developed for micro-electro-mechanical-system (MEMS) based gas sensors. Novel sensors have been designed, fabricated and tested. Nanocrystalline semiconductor metal oxide (SMO) materials include $SnO_2$, $WO_3$ and $In_2O_3$ have been studied for gas sensing applications. Different doping material such as copper, silver, platinum and indium are studied in order to achieve better selectivity for different targeting toxic gases including hydrogen, carbon monoxide, hydrogen sulfide etc. Fundamental issues like sensitivity, selectivity, stability, temperature influence, humidity influence, thermal characterization, drifting problem etc. of SMO gas sensors have been intensively investigated. A novel approach to improve temperature stability of SMO (including tin oxide) gas sensors by applying a temperature feedback control circuit has been developed. The feedback temperature controller that is compatible with MEMS sensor fabrication has been invented and applied to gas sensor array system. Significant improvement of stability has been achieved compared to SMO gas sensors without temperature compensation under the same ambient conditions.

Single walled carbon nanotube (SWNT) has been studied to improve $SnO_2$ gas sensing property in terms of sensitivity, response time and recovery time. Three times of better sensitivity has been achieved experimentally.

The feasibility of using TSK Fuzzy neural network algorithm for Electric Nose has been exploited during the research. A training process of using TSK Fuzzy neural network with input/output pairs from individual gas sensor cell has been developed. This will make electric nose smart enough to measure gas concentrations in a gas mixture. The model has been proven valid by gas experimental results conducted.

This work is dedicated to my family, my advisor and my fellow colleagues.

# ACKNOWLEDGMENT

This work was made possible through the generous support in part of University of Central Florida in-house research and in part of TYCO SAFETY PRODUCTS-SENSORMATIC. I would like to acknowledge Dr. Ming-Ren Lian, Dr. Nen-Chin Liu, Prof. Kevin R. Coffey, Prof. Hyoung Jin Cho, Prof. Michael Georgiopoulos, Prof. Jayanta Kapat, Mr. Claude Daoust and Dr. Weifeng Fei for the valuable discussions. I would also like to thank Mr. Ravi Todi, Mr. Kevin R. C., Mr. Quinones Raul and Mr. Stephen Corry, UCF-Cirent Materials Characterization Facility and TYCO SAFETY PRODUCTS-SENSORMATIC for their instrument supports.

# TABLE OF CONTENTS

# LIST OF FIGURES

# LIST OF TABLES

# 1 BACKGROUND INTRODUCTION

## 1.1 MEMS Technology

Micro-Electro-Mechanical Systems, or MEMS, is a rapidly growing technology for the fabrication of miniature devices using microfabrication processes similar to those used in the integrated circuit industry. MEMS technology provides a new avenue to integrate mechanical, fluidic, optical, magnetic, thermal, chemical, biological and electronic functionality on very small devices, ranging from 0.1 microns to one millimeter. Therefore, MEMS are usually also being referred as Micro Systems Technology, Micro sensors and Actuators or Micromachined Transducers. MEMS devices have two important advantages over conventional counterparts. First, like integrated circuits, the fabrication methods of MEMS allow a massive parallel production of multiple devices in one processing step, so that cost of production can be reduced substantially. Second, they can be directly incorporated with integrated circuits, so that far more complicated systems can be made than with other technologies, chemical sensors for example.[1,2,3,4]

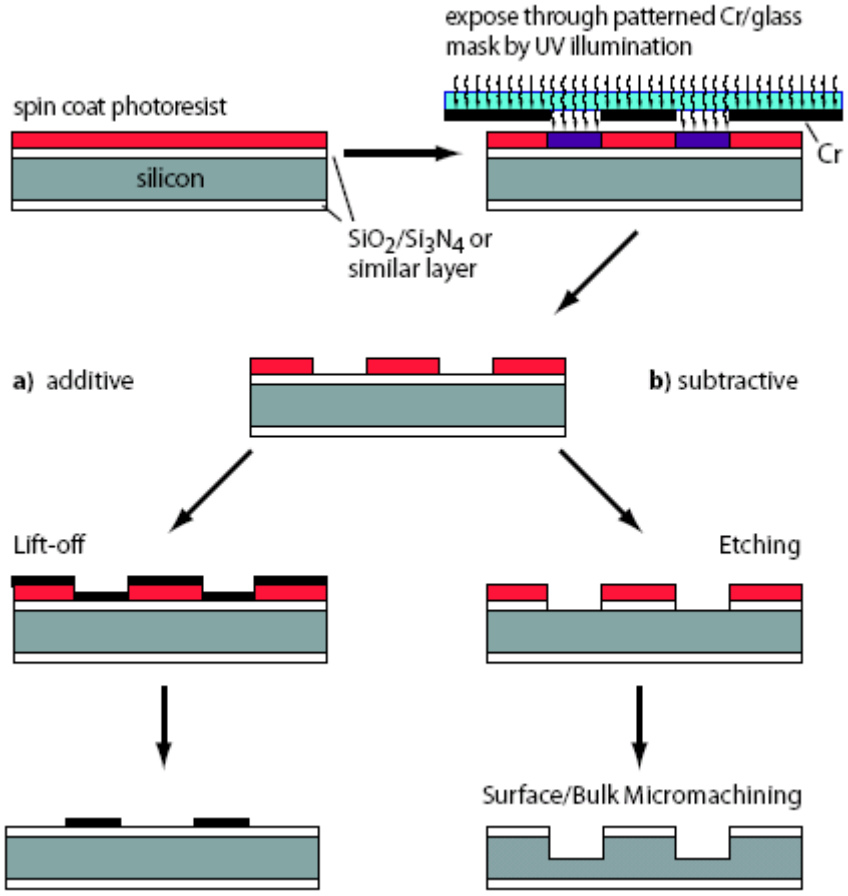


Figure 1 Basic micromachining process (Adapted from Martin 5)

Three basic techniques of micromachining are pattern definition (Lithography), deposition of material (evaporation, sputtering, spin-on etc) and removing of material (etching etc.) Figure 1 shows the basic micromachining process: after exposing a photoresist with UV light through a patterned mask (Cr metal patterned on a glass plate), the image is developed by dissolving the unexposed resist areas (negative resist, not shown), respectively the exposed areas (positive resist). For further processing, there are two approaches. a) Lift-off process: Additive process by depositing another layer of material on top, subsequent removal of the resist and thus releasing the patterned material.

b) Surface micromachining: subtractive approach by dry or wet chemical etching in which the photoresist protects areas from the etchant. Furthermore, the underlying layer, e.g. $SiO_2$ may serve as additional mask for deep etching into silicon, called bulk micromachining.[1,2,3,4,5]

## 1.2 Chemical Sensors

Chemical sensors are devices that convert a chemical state into an electrical signal. The 'chemical state', can be understood different concentrations or partial pressures of molecules or ions in a gas, liquid or solid phase.

### *1.2.1 Gas sensing techniques*

Gas sensor can be considered as interface between the chemical world and the electronics as is indicated in Figure 2. The different transduction principles and the magnitudes that can be measured are [6]:

- Electrochemical: voltages, currents, impedance
- Mechanical: weight, size, shape
- Thermal: heat flow, heat content
- Magnetic: field strength, field detection
- Radiant: frequency, intensity

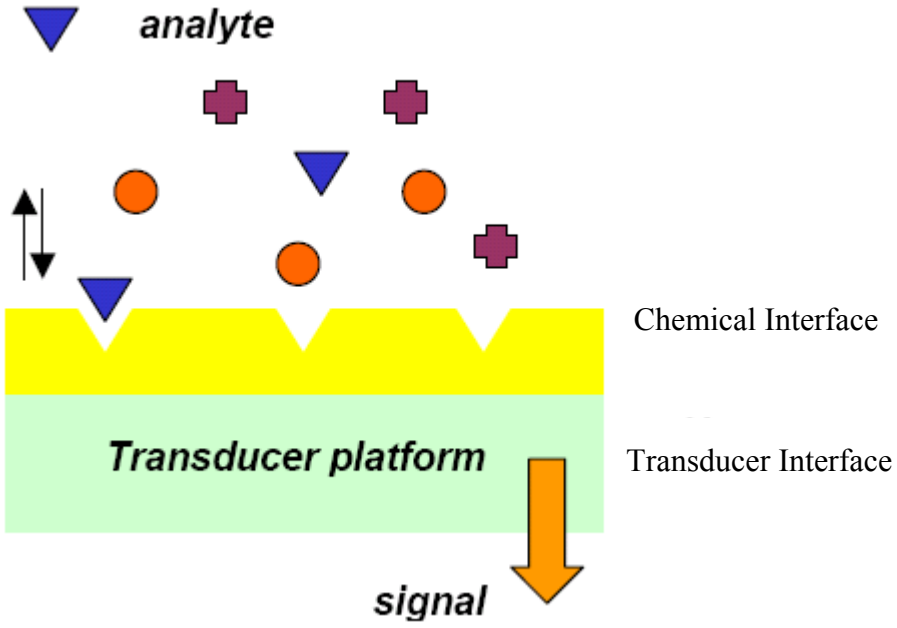


Figure 2 Cross-section of a chemical sensor (Adapted from Stetter ).

Gas sensors are based on physical or chemical adsorption and desorption, optical absorption or chemical reactions that take place on the surface and/or in the bulk of the sensor material. These interactions cause characteristic physical changes of the sensor that is able to detect. A series of different detection principles can be used in chemical gas sensors: conductivity, electrical polarization, electrochemical activity, optical properties, dielectric properties and magnetic properties. The most frequently used sensor technologies can be divided into two basic groups: hot and cold sensors .

Hot sensors are semiconductor metal oxide (SMO) and MOS Field Effect Transistors that operate at elevated temperatures. The SMO sensors, as mentioned above, are based on reaction between adsorbed oxygen on the oxide surface with incoming molecules[7]. The output signal is derived by a change in conductivity of oxide caused by

the reaction with volatile compounds. The MOSFET sensor consists of a doped semiconductor and an insulator (oxide) covered by a catalytic metal. The output signal is based on a change of potential in the sensor due to electrical polarization when molecules react on the catalytic surface. The sensors operate at temperature between $100^{o}C$~$200^{o}C$. Hot sensors' selectivity and sensitivity are dependent on temperature and choice of metal.

Cold sensors operate at ambient temperature. They consist of the conducting organic polymers (CP), oscillating sensors, optical sensors, etc. Conducting organic polymers are based on two main classes of polymers, the pyrroles and the anilines. Volatiles can react with the polymers and thus change the conductivity of it. By altering the structure of the polymer and using different doping ions, the selectivity and sensitivity can be altered. Oscillating sensors are based on the principle that adsorption of molecules onto the sensing layer result in a decrease in frequency due to increased mass and sometimes a changed viscosity of the sensing layer. The QMB (quartz micro balance), BAW (bulk acoustic wave) and SAW (surface acoustic wave) sensors are based on such principle. QMB sensors[8, 9, 10, 11] consist of a piezoelectric quartz oscillator coated with a sensing membrane, whereas the SAW[12, 13, 14] sensors consist of two pairs of finger structure electrodes fabricated onto a piezoelectric substrate with a sensing layer between them. The selectivity and sensitivity is determined by the composition of the coated sensing layer and the operating frequency. Optical gas sensors are another type of sensor used in Electric Nose. In optical sensors, light source excites the gas resulting in a signal from optical properties as absorbance, reflectance, fluorescence or chemiluminescence. Figure 3 shows some commercial available gas sensors. [15]

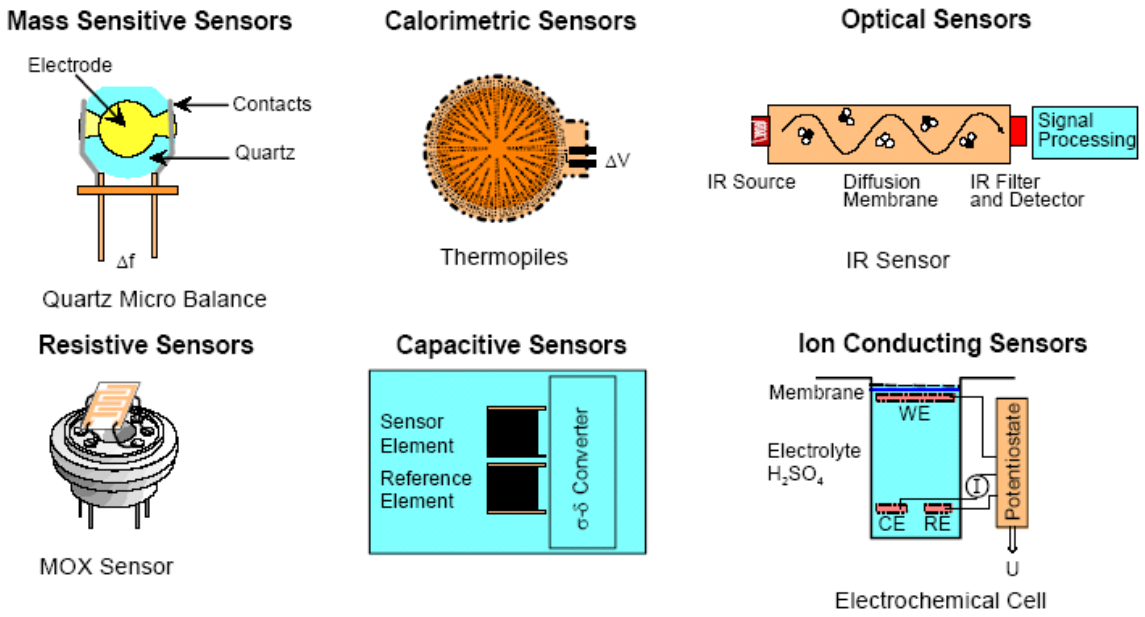


Figure 3 Selection of available gas sensor types (Adapted from Simone )

Table 1 Comparison of different sensing mechanisms

(adapted from Haugen)

| Performance | SMO | MOSFET | CP | QMB | SAW |
|---|---|---|---|---|---|
| Selectivity | Poor | Moderate | Moderate | High | High |
| Sensitivity | >0.1ppm | >0.1ppm | 0.01ppm | >0.1ppm | ppb |
| Reproducibility | Poor | Good | Good | Moderate | Moderate |
| Temperature Dependence | Low | Low | High | Moderate | High |
| Carrier gas | Air ($O_2$) | Air ($O_2$) | Inert/ Air ($O_2$) | Inert/ Air ($O_2$) | Inert/ Air ($O_2$) |
| Humidity Dependence | Moderate | Moderate | High | Low | Low |
| Operating Temperature (C) | 200~500 | 100~200 | Ambient | Ambient | Ambient |
| Response time (s) | 0.5~5 | 0.5~5 | 20~50 | 20~50 | 20~50 |
| Recovery time | Fast | Fast | Slow | Slow | Slow |
| Lifetime (year) | 3~5 | 1~4 | 1~2 | <2 | <2 |

Most frequently used sensors in electrical nose system are the SMO and CP type.[16] A summary of the performance of the different sensor techniques is presented in Table 1.

*1.2.2 Semiconductor metal oxide gas sensors*

Since Seiyama and Taguchi used the dependence of the conductivity of ZnO on the gas present on the atmosphere for gas sensing applications,[17,18] many different metal oxides have been proposed for gas detection. It has been proved that semiconductor gas sensors have highly improved performances for a higher precision and a reduced analysis time.[19,20,21,22,23] Heated semiconductor metal oxides are kind of the electrochemical class of chemical sensors (impedance) sensors. Gas sensors based on different metal oxides ($SnO_2$, $TiO_2$, $In_2O_3$, $WO_3$) are often called SMO sensors (Semiconductor Metal Oxide). In their simplest configuration, SMO sensors consist of a substrate with a heater, electrodes and a sensitive layer in contact with the electrodes.

According to Williams and Moseley[24], most target gases are detected due to their influence on the oxygen stoichiometry of the surface. Many studies have revealed that the key reaction involves modulation of the concentration of surface oxygen ions.

Some metal oxides, such as $SnO_2$, $TiO_2$ or $WO_3$, are intrinsically n-type bulk semiconductors, for which, the metal stoichiometric excess is due to oxygen vacancies. Under normal sensor operating conditions, the conductivity of the surface has revealed to be much less than that of the bulk. This has been attributed to the formation of surface

oxygen ions that trap electrons, inducing a surface depletion layer and thus the development of Schottky barriers at inter-particle contacts. In the case of n-type metal oxides, since the electrons come from ionized donors via the conduction band, the charge carrier density at the interface is thereby reduced and a potential barrier to charge transport is developed (See Figure 4). As the surface charge is developed, the adsorption of further oxygen is inhibited, the adsorption rate slows down because charge must be transferred to the adsorbate over the developing surface barrier and the coverage saturates at a very low value. At the junction between the grains of the solid, the depletion layer and associated potential barrier lead to high-resistance contacts, which dominate the resistance of the solid. The resistance is then sensitive to the coverage on the surface of adsorbed oxygen ions and any factor that changes this, will change the resistance.

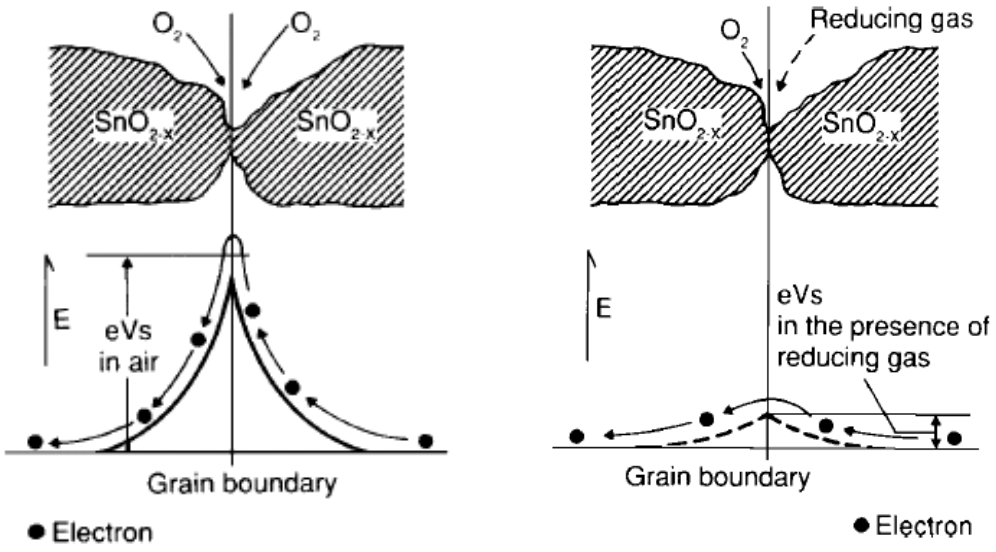


Figure 4 SMO sensor working principle (Adapted from Figaro Co. [25])

The relationship between sensor resistance and the concentration of deoxidizing gas can be expressed by the following equation over a certain range of gas concentration:[25]

$$Rs = A[C]^{-\alpha} \quad (1)$$

where: Rs = Electrical Resistance of the Sensor

A = Constant

[C] = Gas concentration

$\alpha$ = Slope of Rs curve

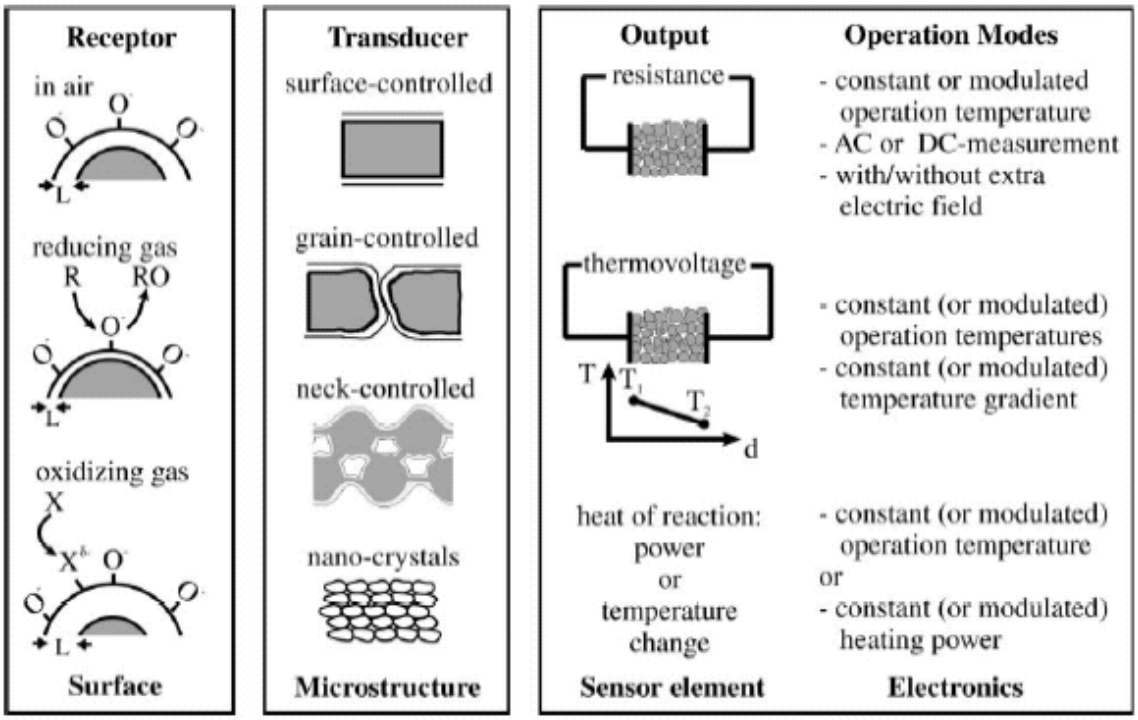


Figure 5 Schematic view of the gas sensing elements of SMO sensor: receptor, transducer and output signal (adapted from Simon ).

Figure 5 shows a schematic view of the gas sensing elements of SMO sensor. Like other gas sensors, SMO gas sensor also comprise of three major parts: Receptor, Transducer and Output signal.[74] The *receptor* is the surface of the metal oxide, where chemical species undergo absorption (physically and chemically), reaction and desorption. The interaction of the gaseous molecules will induce a change in the depletion layer of the metal oxide grain. These changes are transduced into an electrical signal depending on the microstructure of the sensitive film (the *transducer*) including porosity of the film, the grain size and the different grain intersections. This output signal (e.g. resistance or thermal voltage) will be detected by corresponding electronics.

Some characteristics that make SMO sensors appealing for gas sensor users are:

- Low cost, small size and easy to handle (compared to other gas sensors)
- Fast sensor response and recovery time
- Robust construction, good mechanical strength and high reliability (in part because of the simple associated electronics) leading to a low failure rate.
- Long operating life and maintenance free
- Good resistance to corrosive gases.

On the other hand, they have some disadvantages that are still a matter of research (some of them being common to most of gas sensors):

- Poor selectivity of single sensors
- Influence of humidity and temperature

- High power consumption (except micro-machined devices)

Selectivity is the major obstacle of gas sensor and gas sensor arrays development. It has been demonstrated that semiconductor gas sensor's selectivity can be largely improved by doping with specific metals or metallic oxides[74,75]. As single doped gas sensor is only sensitive to a specific gas or limited gases, multiple sensors or a sensor arrays are needed to detect multiple gas species at the same time in a mixture environment. Sufficient selectivity of metal oxide sensors can only be achieved if several sensors are put together to an array.[26,27] In this case, a lack of selectivity and therefore overlapping sensitivities of different sensors can be turned into an advantage. Other important advantage of SMO sensor is that its fabrication process is completely compatible with IC fabrication and a SMO sensor array can be integrated on to single chip.

*1.2.3 Thick film SMO sensor*

Ceramic thick film sensors were the first type of metal oxide semiconductor sensors. The first sensors were fabricated by pressing a heater coil and an electrode wire in the powder material. The sensitive material was painted as a paste on an alumina tube, in which the heater was separated from the layer. Later planar structures were obtained by thick-film technologies like screen printing onto electrode-covered ceramic $Al_2O_3$ substrates with a heater and temperature sensor at the backside.

The oxide base material is typically prepared from salt solutions (mostly $SnCl_4$), organic-tin compounds, or the pure metal dissolved in nitric acid as precursors. This process will be nominated more general the sol-gel process, knowing that normally this means a special preparation route.[28,29] Improvements of the sensor properties are possible by chemical modifications of the precursor or of the base material. Catalysts and receptor functions[30] can be introduced before or during the preparation of the paste by mixing the calcined powder with salt solutions or by addition of metals (colloid method).[31] In this case it is supposed that the tin oxide surface absorb all the metal catalyst from the solution. The intended catalyst concentration is calculated as weight percent usually in the range between 1% and 3%. The catalyst surface density could therefore be much higher. Typical catalysts are noble metals like Pt[32], Pd[33], Au[34], Cu[35] or basic material like Ca[36] or La[37].

In spite of their complicated microscopic and chemical structure, the ceramic sensors have surprisingly good sensitivities, because they have been optimized by a careful choice of materials and preparation steps. Nevertheless long term stability can only be achieved by long pre-aging times. Other drawbacks are high power consumption of the final bulky device and problems arising mounting the hot sensor element.

### *1.2.4 Thin film SMO sensor*

The gas sensing thin film is the key part of the SMO gas sensor. Most widely used techniques of thin film fabrication can be distinguished as three main groups:

powder/slurry deposition, chemical vapor deposition (CVD) and physical vapor deposition (PVD) (Table 3) [38,39, 40,41]. The main difference between powder/slurry based films and CVD or PVD has traditionally been attributed to their different film thickness. While the former lead to sensitive layers of several microns of thickness (thick films), the layer thickness of the latter varies between 20 and 1000 nm. Beyond this classification, there is a fundamental difference in the microstructure of these thick and thin films. Thin films are usually very 'compact' (not porous), so the interaction with gas is limited to the external surface of the sensitive layer. On the other hand, gas can penetrate through most of thick films and so the interaction can occur throughout the whole layer. This has led to some authors argue that thick film must be more sensitive than thin films, since the change of conductivity is not limited to the outermost zone of the sensitive layer but to the whole layer.

Table 2 Typical deposition techniques used for the preparation of gas-sensitive materials based on semiconductors.

| ***Powder/Slurry*** | ***CVD*** | ***PVD*** | |
|---|---|---|---|
| | | ***Sputtering*** | ***Evaporation*** |
| Sol-gel | Thermal CVD | Sputtering | Molecular beam epitaxy |
| Precipitation | Plasma CVD | Reactive sputtering | Thermal evaporation |
| Screen-printing | Laser induced CVD | Cathode sputtering | Reactive evaporation |
| Dip coating | Electroless plating | | Ion plating |
| Drop coating | | | Reactive ion plating |
| Pulverisation coating | | | Arc evaporation |
| Spin coating | | | Laser evaporation |

However, it is necessary to be pointed out here that spin-coating techniques, which are actually using a slurry, are able to obtain 'thin films' in the sense of thickness (and the slurry can be obtained by a sol-gel process, for instance), being actually 'thick films' in terms of porosity[42]. With regard to screen-printing, it must be understood that this technique is a two-step process: firstly the powder is obtained (by sol-gel, precipitation or any other method) and then slurry based on this powder is screen printed. A more complete description of the application of these techniques to SMO sensors can be found in [43].

Thin film technologies based on vapor deposition have some limitations or disadvantages. Vacuum evaporation may suffer from compositional inhomogeneity, capability of good step coverage for topographies, difficulties to control the film thickness, etc. Sputtering deposition is expensive and usually creates very dense thin film, which is not good for gas sensing applications.

Sol gel process is very promising technology for nanostructured thin film for gas sensing purposes. Advantages comparing to conventional vapor processing techniques include simple equipment with possibility of low temperature fabrication, ability to produce ultra fine particles, ability to control the sample shape, morphology and the addition of dopants simultaneously and more accurately. Furthermore, the high porosity and large surface area enhance sensitivity[44, 45]. Preparation of sols using either alkoxide or chloride precursors utilizing either dip or spin coating methods has been reported[46, 47].

The gas sensing properties of $SnO_2$ semiconductor thin films depends strongly on the methods of processing. It has been pointed that the crystallite size[48] and the film

thickness have pronounced effects on the gas sensitivity. It has been recognized that $SnO_2$ semiconductor thin film can achieve the maximum gas sensitivity only if the crystallite size within the film is comparable with its space-charge layer thickness. Besides, crystallite size also affects another important property of semiconductor gas sensor, the surface to volume ratio. When particle size decreases, the surface to volume ratio increases largely (reverse proportional to the particle size). For example, a particle size decrease from 100 μm to 20nm, the surface to volume ratio increases by 5000 times! A remarkable enhancement of sensitivity can be realized.

## 1.3 Properties of $SnO_2$

### *1.3.1 Crystalline structure of $SnO_2$*

$SnO_2$ is an anisotropic polar crystal, which crystallizes with tetragonal ($a=b\neq c$, $\alpha=\beta=\gamma=90^o$) rutile structure. The unit cell contains six atoms, two tin, and four oxygen. Each tin atom is at the centre of six oxygen atoms placed approximately at the corners of a regular slightly deformed octahedron, and three tin atoms approximately at the corners of an equilateral triangle surround every oxygen atom. (See Figure 6)[49] $SnO_2$ is an n-type, wide band gap semiconductor of which electrons are majority carrier, and electron concentration (n) of conduction band was affected by gas. The origin of the n-type behavior is the native non-stoichiometry caused by oxygen vacancies.[50]

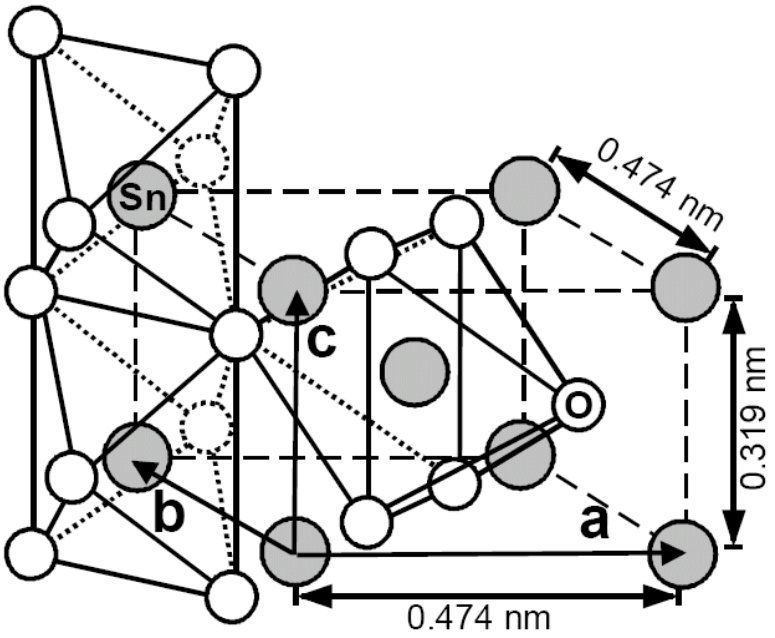


Figure 6 $SnO_2$ crystalline: tetragonal rutile structure (Adapted from Jarzebski )

*1.3.2 Conductivity*

The conductivity σ of a semiconductor crystal can be described as the sum of electronic ($\sigma_n$ , $\sigma_p$ ) and iconic conductivity ($\sigma_{ion}$) if the conduction processes are considered independent.[51, 52] $SnO_2$ gas sensors are typically operated at temperature between 200°C to 400 °C. In this range the ionic contribution can be neglected and the conductivity of $SnO_2$ can be calculated according to:

$$\sigma = \sigma_n + \sigma_p \tag{2}$$

The resistance of bulk material with conductivity σ, mobility μ, length l and cross section A can be calculated according to:

$$R = \frac{1}{\sigma \cdot b \cdot d} = \frac{1}{\sigma \cdot A}, with\ \sigma = \sigma_n + \sigma_p = n \cdot \mu_n \cdot q + p \cdot \mu_p \cdot q \quad (3)$$

where the charge carrier concentrations n and p for an intrinsic semiconductor can be calculated according to:

$$n = \int_{Ec}^{\infty} D(E) f(E) dE;\ p = \int_{-\infty}^{Ev} D(E)(1 - f(E)) dE; \quad (4)$$

with the Fermi-Dirac distribution f(E) and the density of states D(E):

$$D(E) = \frac{1}{2\pi^2} (\frac{2m_e}{\hbar})^{\frac{3}{2}} (E - E_c)^{\frac{1}{2}};\ f(E) = \frac{1}{1 + \exp(\frac{E - E_F}{KT})} \quad (5)$$

therefore, the charge carrier concentrations n and p can be approximated by:

$$n = N_c \exp(\frac{E_F - E_C}{KT});\ N_C = 2(\frac{2\pi m_n KT}{h^2})^{\frac{3}{2}} \quad (6)$$

$$p = N_v \exp(\frac{E_V - E_F}{KT});\ N_V = 2(\frac{2\pi m_p KT}{h^2})^{\frac{3}{2}} \quad (7)$$

For n-type semiconductor, n>>p, therefore, $\sigma_n \approx q\mu_n n$, and for p-type, p>>n, $\sigma_p \approx q\mu_p p$. The n-type behavior of $SnO_2$ is associated with oxygen deficiency in the bulk. The donors are singly and doubly ionized oxygen vacancies with donor levels $E_{D1}$ and $E_{D2}$ located around 0.03 eV and 0.15eV below the conduction band edge. [53,54] In the case of $SnO_2$ the extrinsic donors are multi step donors. Therefore, donor and acceptor energy levels, concentrations, and the operation temperature determine the conductivity of $SnO_2$.

### *1.3.3 Oxygen absorption on $SnO_2$ surface*

When detecting gas is presented, molecules will be absorbed onto $SnO_2$ surface before reacting. Two absorption processes could have happened, physical absorption and chemical absorption. Physisorption is the caused by Van-der-Waals interaction, while chemisorption is based on stronger forces and hence is connected with an electron transfer between absorbent and absorbate. Ionosorption is chemisorption because the charge is transferred to the conduction band, which causes a band bending and thus changing of surface resistance of the sensing material. $SnO_2$ surface's absorption of $O_2$ can be considered as an ionosorption process of a gas with acceptor character. The absorption of an electron acceptor creates acceptor surface level where electrons of conduction band are trapped creating a depletion layer whose depth is described by the Debye length $\lambda_d$. The negative charge built at the surface makes further charge transfer more difficult. At equilibrium, a band bending (eVs) result influences the material resistance. Reducing gases, e.g. $H_2$, release electrons into the sensitive material upon interaction at the sensor surface and thus decrease the resistance.

### *1.3.4 $SnO_2$ grain boundaries*

Porous $SnO_2$ film consists of numerous interconnected metal oxide grains. They can be either single crystals or polycrystalline agglomerates. High porosity will enable the ambient gases to access these inter granular connections. Because of this, a depletion layer is created around the grains, the extension of which is determined by the partial gas

concentrations and the bulk characteristics of $SnO_2$. Therefore, grain boundaries, as bottlenecks for electronic grain-grain transfer, play an important role in the sensing layer conduction. If the grains are connected and the depletion layer depth $\lambda_d$ is much smaller than the grain radius r, a gain bulk area unaffected by the gas will still exist. In order to contribute to electronic conduction, the electrons originating from the "bulk" must overcome these depletion layers and the related potential barriers with the barrier heights eVs at the inter-granular contacts. This is equivalent to a significant resistance increase of the sensitive layer.

The overall resistance R is a function of the contributions of the bulk and the surface of $SnO_2$ grains, the electrode contacts and the inter-granular contacts. The properties of the bulk, i.e. the part of the grain, which is not depleted, are not influenced by surface phenomena due to the rather low operation temperature (<400$^oC$). the resistance contribution of the electrode contacts, which is related to Schottky barriers between the sensing layer and electrodes, depends on the contact material. Electrodes might also show a gas dependent barriers, which have to be overcome for the numerous inter-granular contracts between the electrodes. In most cases, the resistance contribution of the numerous inter-granular contacts dominates the other contributions.

*1.3.5 Sensing film topology*

The differences in compact and porous layers are schematically sketched in Figure 7. The sensitive metal oxide layer is deposited over the metal electrodes onto the

substrate. In the case of compact layers, the gas cannot penetrate into the sensitive layer and the gas interaction is only taking place at the geometric surface. In the case of porous layers the gas penetrates into the sensitive layer down to the substrate. The gas interaction can therefore take place at the surface of individual grains, at grain-grain boundaries and at the interface between grains and electrodes and grains and substrates. Therefore, both the surface layer and the volume of the layer are accessible to the gases and in this case, the active surface is much higher than the compact one.

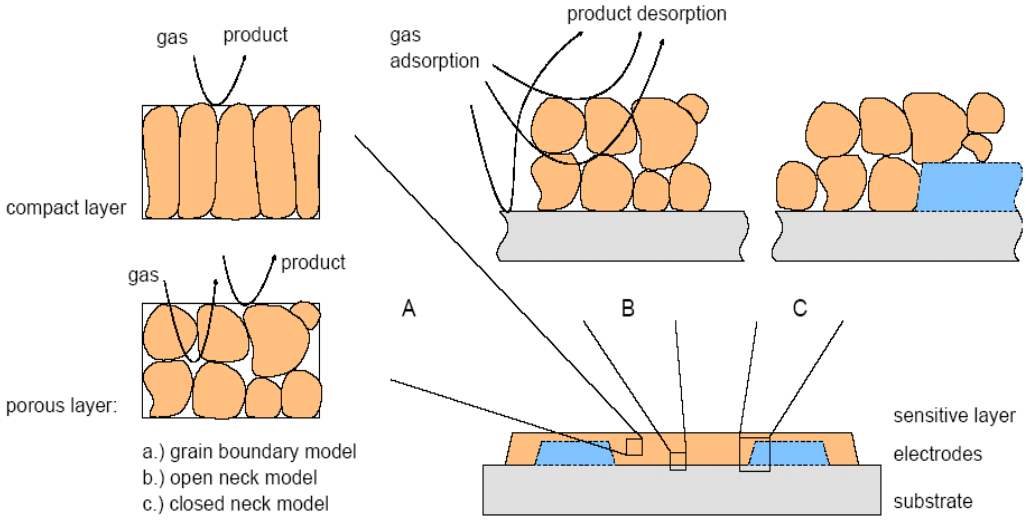


Figure 7 Comparison of gas sensing property of compact film and porous film (Adapted From Barsan [55] )

For compact layers, there are at least two possibilities: completely or partly depleted layers, depending on the ratio between layer thickness and Debye length $\lambda_D$. For partly depleted layers, when surface reactions do not influence the conduction in the entire layer, the conduction process takes place in the bulk region. Normally, two

resistances occur in parallel, one influenced by surface reactions and the other not; the conduction is parallel to the surface, and this explains the limited sensitivity of the compact layers.[55]

For porous layers the situation can be further complicated by the presence of necks between grains. It may be possible to have all three types of contribution in a porous layer: surface/bulk (for large enough necks, layer thickness>thickness of depletion layer), grain boundary (for large grains not sintered together), and flat bands (for small grains and small necks). For small grains and narrow necks, when the mean free path of free charge carriers becomes comparable with the dimension of the grains, a surface influence on mobility should be taken into consideration. This happens because the number of collisions experienced by the free charge carriers in the bulk of the grain becomes comparable with the number of surface collisions; the latter may be influenced by absorbed species acting as additional scattering centers. [56]

Figure 8 illustrates the way in which the metal semiconductor junction, built at electrode sensitive layer interfaces, influences the overall conduction process. $R_C$ is the resistance of the electrode-$SnO_2$ contact, $R_{l1}$ is the resistance of the depleted region of the compact layer, $R_{l2}$ is the resistance of the bulk region of the compact layer, $R_1$ is the equivalent series resistance of $R_{l1}$ and $R_C$, $R_2$ is the equivalent series resistance of $R_{l2}$ and $R_C$, $R_{gi}$ is the average inter-grain resistance in the case of porous layer, $E_b$ is the minimum of the conduction band in the bulk, $q\ V_S$ is the band bending associated with surface

phenomena on the layer, and $qV_C$ also contains the band bending induced at the electrode-$SnO_2$ contact.

For compact layers, they appear as a contact resistance ($R_C$) in series with the resistance of the $SnO_2$ layer. For partly depleted layers, $R_C$ would be dominant, and the reactions take place at the three phase boundary, electrode- $SnO_2$-atmosphere, control the sensing properties. For porous layers, the influence of $R_C$ may be minimized due to the fact that it will be connected in series with a large number of resistances, typically thousands, which may have comparable values ($R_{gi}$ in Figure 8). [55]

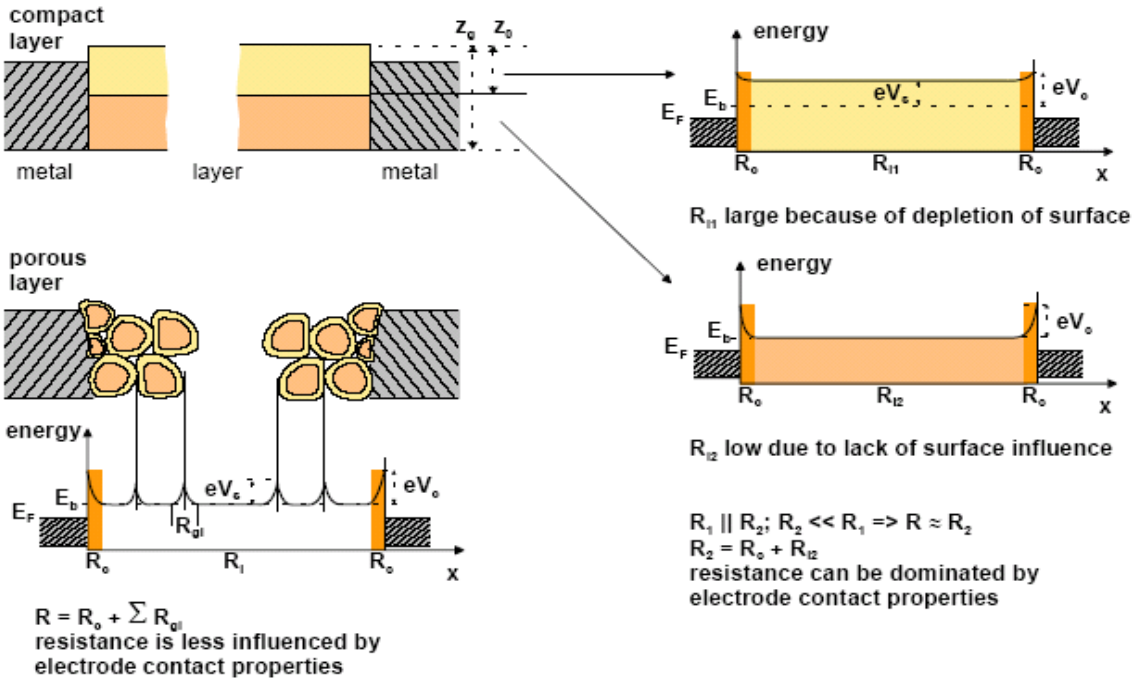


Figure 8 Geometry and energetic bands comparison of compact and porous sensing layers (Adapted From Barsan )

## 1.4 Data Processing and Analysis

### *1.4.1 Overview of pattern recognition techniques*

Data processing of multivariate signal in gas sensor arrays represents an essential part of gas measuring system. Most of the sensor array systems require a suitable post processing procedure. Data processing techniques used in post processing on pattern recognition routines include principal component analysis (PCA), partial least squares (PLS), functional discriminate analysis (FDA), cluster analysis (CS), fuzzy logic or artificial neural network (ANN), etc[57, 58,59]. Among these techniques, PCA, PLS, FDA and CS are based on a linear approach; while fuzzy logic and ANN are regarded as nonlinear methods. Results[60] show that for a typical classification problem, there is no significant difference in overall classification rate between linear statistical method and no-linear such as ANN classifiers. PCA has been found successful in identifying gases such as CO and CH4[61]. However, in a highly nonlinear task of predicting single component concentration in gaseous mixtures, the gas sensor array data are often non-linear in nature[62]. Since most SMO sensors have non-additive sensitivity to different gases, i.e. components of gas mixtures have correlating effect, sensor response doesn't have linear relation with the gas concentrations. Room temperature and humidity can also change the sensor's response in a nonlinear manner. Therefore, by using simple data transformations such as logarithms, linear statistical methods can never satisfy in determining the concentration of each component in gaseous mixtures.

Non-linear methods such as ANN can process sensor array data in a better way[63]. The most commonly used ANN method is the Kohonen and the Multilayer Perceptron (MLP) networks. G. Huyberechts et al[64] show that an ANN is capable to determine all components quantitatively in a three components mixture. A hybrid neural network which contains self-organizing Kohonen layer and MLP has been used to determine the individual analytic concentrations in the mixture of gases with good accuracy[65]. Despite all these advantages, ANN usually suffers from the slow convergence in training process and the risk of over-fitting.

*1.4.2 Fuzzy neural network*

The fuzzy neural system is the combination of fuzzy logic system and neural networks. Fuzzy logic system deals with explicit knowledge which is explainable and understandable, and neural networks deal with implicit knowledge which can be acquired by learning. Because fuzzy logic has tolerance for imprecision of data and neural networks have tolerance for noisy data[66], therefore, the fuzzy neural system may be the most powerful data handling method for gas sensor arrays. A fuzzy logic can enhance the generalization capability of a neural network by providing more reliable output when extrapolation is needed beyond the limits of the training data[67]. Sundic et al. indicated that fuzzy neural network has obvious advantages over linear algorithms. And it has been also confirmed that a fuzzy neural network has better accuracy than the single neural

network, if it is simply connected to a self-organizing competitive fuzzy layer and the supervised multilayer perceptron (MLP) subnetwork in cascade. [68]

A typical fuzzy neural network contains the following five different layers:

- Input layer
- Fuzzification layer
- Fuzzy rule layer
- Defuzzification layer
- Output layer

Input signals are introduced into FNN through input nodes of the *input layer*. In a *fuzzification layer*, each neuron represents an input membership function of the antecedent of a fuzzy rule. In this layer fuzzy rules are fired and the value at the end of each rule represents the initial weight of the rule, and will be adjusted to its appropriate level at the end of training process. In the *defuzzification layer*, each neuron represents a consequent proposition and its membership function can be implemented by combining one or two sigmoid functions and linear functions. The weight of each output link represents the center of gravity of each output membership function of the consequent and is trainable. In the output layer, adjustment is made based on the connection weights and the output of each membership functions.

*1.4.3 TSK fuzzy neural network*

Takagi - Sugeno - Kang (TSK) FNN model or Neuro-Fuzzy with TSK fuzzy rules (NFST) might be the most important one and the most often used one among all fuzzy neural networks (FNN) so far developed. Comparing TSK with other fuzzy neural network in gas measuring application, Osowski[69] pointed out that TSK neuro-fuzzy network yields the minimum mean absolute error and mean absolute percentage error. Recent researches have been conducted on searching the effective approaches in optimizing TSK neural network[70,71,72]. A novel learning algorithm has been proposed to achieve fast convergent rate and small mean square error, by using self-organizing and fast learning rules[73].

A Takagi-Sugeno-Kang (TSK) FNN model is characterized by TSK rules, given the form of

*if* $x_1$ *is* $A_1$ , *AND* $x_2$ *is* $A_2$ , *AND* ... $x_N$ *is* $A_N$ , *then* y=f(**x**)

Where $\mathbf{x} = [x_1, x_2, ..., x_N]^T$ and $A_1$, $A_2$, ... $A_N$ are fuzzy sets in the premise, while y is a crisp function in the consequent.

In contrast to a crisp set, a fuzzy set is defined without crisp boundary, where the transition between "belong to a set" and "not belong to a set" is gradual and this transition is characterized by the membership functions in the range [0, 1]. Such assumption guarantees the flexibility in modeling. The membership may be described either in a discrete form as a set of membership values or as a continuous function valid in some range of values of the variable x. The most popular types of membership functions

belong to the triangle, trapezoidal, Gaussian or bell functions. In this study, the design of gas measuring system will apply the Gaussian function as the membership function, given in the form,

$$\mu(x) = \exp\left[-\left(\frac{x-c}{\sigma}\right)^2\right] \tag{8}$$

In which, $c$ is the centre (mean) and the parameter $\sigma$ represents the width of the function (variance).

The general function y=f(**x**) in TSK model is usually a polynomial of the input variables $x_i$. We will apply here the linear form of this function, for which

$$y_i = f_i(\mathbf{x}) = p_{i0} + \sum_{j=1}^{N} p_{ij} x_j \tag{9}$$

where $p_{ij}$ are the adjustable parameters.

For R fuzzy rules, we have R such membership functions $\mu_1(\mathbf{x})$, $\mu_2(\mathbf{x})$, ..., $\mu_R(\mathbf{x})$. Assuming that each antecedent is followed by the consequent of the linear form as above, for i= 1, 2, …, R, the aggregator of rules in TSK model generates the output crisp signal of the system as follows, $o(x) = \dfrac{\sum_{i=1}^{R} \mu_i(\mathbf{x}) y_i(\mathbf{x})}{\sum_{i=1}^{R} \mu_i(\mathbf{x})}$ (10)

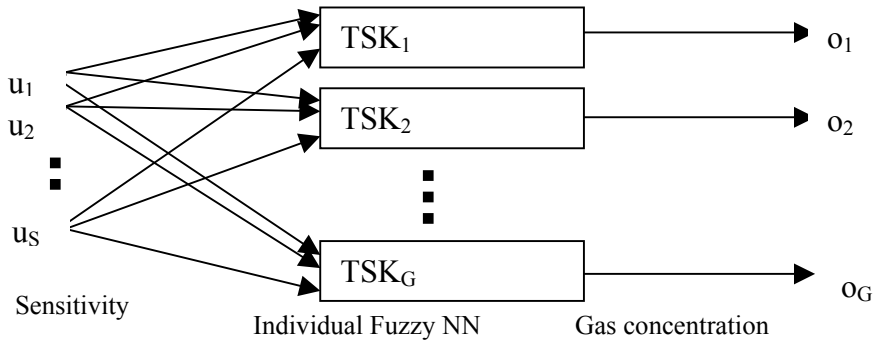


Figure 9 TSK construction

The last relation is called the universal approximation formula. This formula forms the basis for the practical implementation of the TSK FNN.

## 1.5 Electric Nose

Detection and quantification of gases present in the ambient (explosive gas leaks in houses, e.g.) is very important but complex in nature. The human nose is able to differentiate between hundreds of smells but fails if absolute gas concentration of odorless gases needs to be detected[74]. It is difficult for using single gas sensor to detect a specific gas in a gas mixture, as there exists a high cross-sensitivity to other gases that are not able to be measured.[75] Therefore, a gas sensor array able to detect different interested gases has been a major focus of research on gas sensors[76,77]. Sensor arrays have been described as "Electric Nose" (EN) in comparing to the human nose. An Electric Nose (EN) based sensor consists of three parts (1) sampling system for sample treatment (2) the chemical sensor array, and (3) pattern recognition[78]. So far, Electric Nose system for gas detection has found applications in a wide range of fields as the following: (1)

Environmental monitoring in HVAC system for air quality control, safety/anti terrorism, explosive gas (bomb) and hazardous pollutant gas detection in public area like airport, shopping center etc.) [79,80,81,82,83]. (2) Odors detection in industries such as food, drinks, fragrance, chemical etc[84,85,86,87]. (3) Health care such as bacterial infections, detection of some volatile compounds in the breath of patients associated with certain diseases such as lung cancer, alcohol detection etc[88,89]. (4) Other important areas include automobile industries[90,91], space, smart domestic applications[88,89,92].

However, techniques available are costly and time-consuming, and limitations in sampling and analytical techniques exist. Currently, commercially available Electric Nose system can be divided into two parts, they are: (1) Desktop analytical instruments including Fourier transform infrared (FTIR) instrument, gas chromatographs and mass spectrometers such as Fox 2000 Alpha MOS, Agilent 4440, Osmetech, Smartnose, and E-Nose 4000 EEV (PC based, using zero reference gas and static response, skilled operator required, with price ranges from $40K to $130K) (2) Portable units such as C320 of Cyrano Sciences, Applied Sensor of VOC checker, and SAWTEK of VaporLab (with price ranges from $5K to $10K). Only for process control and laboratory analytics, one can afford high performance, large and expensive desktop gas analyzers. For all other purposes, either the money or the place required for gas analyzer needs to be taken in considerations. Portable units have advantages such as small size, low cost, and easy manipulation. However, further research is needed mainly to improve their sensitivity, selectivity and stability[61, 93, 94]. Clearly, a need exists for accurate, low power consumption, inexpensive, real-time, in-situ analyses using robust Electric Nose system.

A considerable amount of researches and developments have been directed towards the development of high sensitive and high performance gas sensing devices to achieve a qualitative and quantitative analysis of a complex mixture of gases in the past decade[95,96,97,98,99]. Micro-electro-mechanical systems (MEMS) plus nano technologies are most promising emerging technologies. [100,101,102,103,104]

# 2 EXPERIMENT PROCEDURE

## 2.1 Nanostructured SMO Thin Film Preparation by Sol Gel process

Nanocrystalline semiconductor metal oxide was prepared following a soft chemistry route, classified as a sol-gel route, which has been introduced in the previous section [1.3.4]. Sol-gel synthesis method also allows easy manipulations of adding doping material to achieve the selectivity with atomic level mixing and uniform dispersion efficiency.

### *2.1.1 Pure $SnO_2$ sol preparation*

Tin isopropoxide ($Sn(O^iPr)_4$) was first dissolved in anhydrous ethanol. A complexing agent, acetylacetone (AcAc), was added to stabilize the hydrolysis of tin isopropoxide. After complete mixing using magnetic stirring, hydrolysis was performed by adding distilled water in an appropriate ratio. A clear and stable sol was formed after continuous stirring. The viscosity of the sol was adjusted with addition of PVA (poly vinyl alcohol). To prevent cracking during the firing process, PEG (poly ethyl glycol) was added to improve the plasticity of the coating.[105]

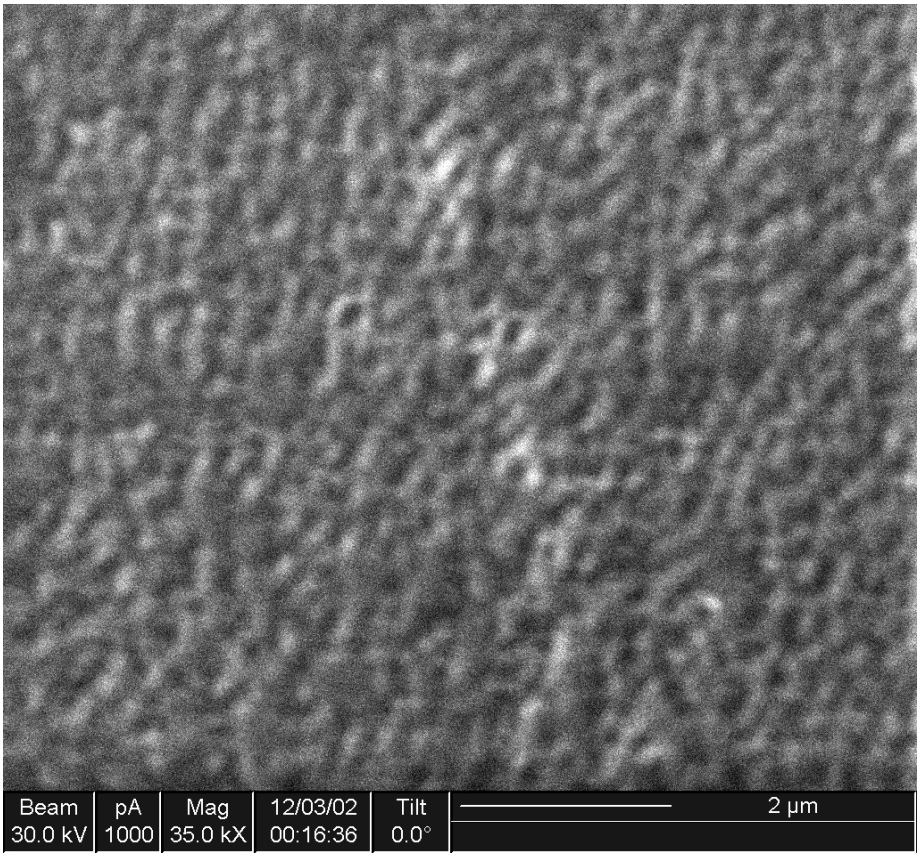


Figure 10 Porous topology of Tin Oxide film ~15nm

*2.1.2 Preparation of $SnO_2$ sol with different dopants*

Metal additives can enhance the material sensitivity and selectivity, and shorten response time and lower working temperature of the SMO gas sensor. The most widely used method is the addition of catalytically active noble metals, which can promote selectivity of SMO gas sensor. Table 3 lists some reported SMO sensors with dopants for specific target gases. Considering our gas detection requirements the nature of neural network, we choose Ag, Pd, Pt, CuO, Mo as doping material for $SnO_2$, and $In_2O_3$ and $WO_3$ as additional SMO sensing materials.

Table 3 Some reported SMO gas sensors and target gases

| Target Gas Detected | Metal Additive/SC | References |
|---|---|---|
| $H_2$ | Pt / $SnO_2$<br>Pd / $SnO_2$<br>$In_2O_3$<br>Ag/Pt / $SnO_2$ | 106,107<br>108,109<br>110<br>111 |
| CO | Pt/ $SnO_2$<br>Pd/ $SnO_2$<br>Cu / $SnO_2$<br>$In_2O_3$ | 112, 115<br>112, 113<br>114<br>115,116,110 |
| $H_2S$ | CuO / $SnO_2$<br>Ag / $SnO_2$<br>$WO_3$ | 117,118,119,120,121<br>122<br>123,124,125,126 |
| $NO_2$ | CuO / $SnO_2$<br>$SnO_2$<br>$In_2O_3$<br>$WO_3$ | 127<br>128<br>116<br>129 |
| $CH_4$ | Pd / $SnO_2$ | 113 |
| $NH_3$ | Mo / $SnO_2$ | 83 |

- Platinum (Pt)

  Two methods can be used for Pt doping:

  I. Sputtering: after $SnO_2$ thin film was spin coated and sintered, 20 $\overset{o}{A}$ Pt was sputtered onto the surface of $SnO_2$ thin film followed by a 500$^o$C thermal diffusion process.

  II. Platinum(II) acetate ($Pt(OOCCH_3)_2$) was added into the $SnO_2$ sol followed by magnetic stirring

- Silver (Ag)

$AgNO_3$ was added into the $SnO_2$ sol and followed by a magnetic stirring (for 1 day), while $HNO_3$ was used to stabilize the $SnO_2$ sol. Figure 11 shows SEM picture of $SnO_2$ film doped with Ag.

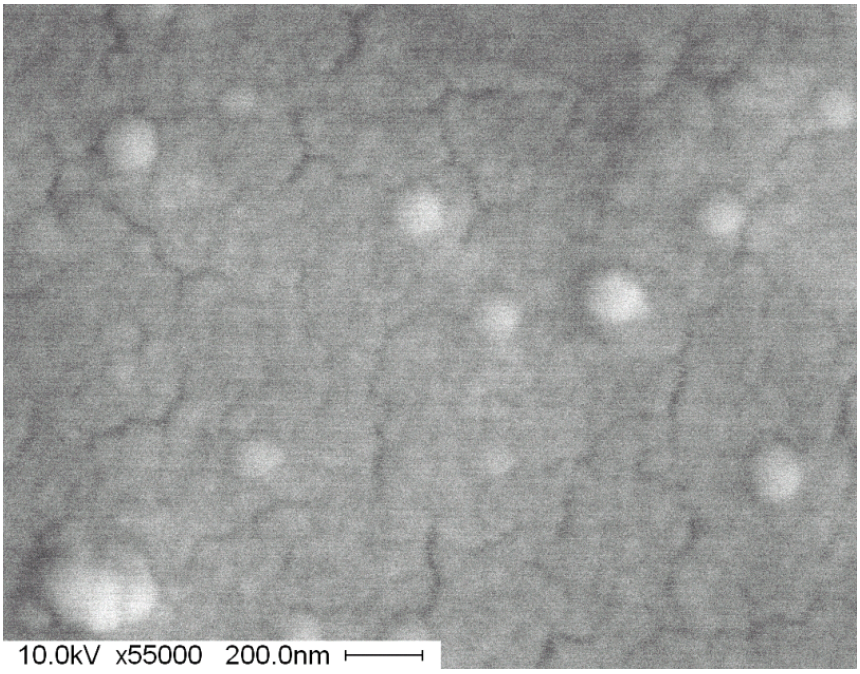


Figure 11 SEM picture of $SnO_2$ doped with Ag

- Copper Oxide (CuO)

Since $Cu(NO_3)_2$ is acidic salt solution, while the original $SnO_2$ is poor alkaline solution, when $Cu(NO_3)_2$ was added to $SnO_2$ sol, precipitate will generate, which cause the sol unclear. Adding proper amount of $NH_4OH$ (controlling the PH value) and heated stirring over night can make those precipitate ($Cu(OH)_2$) well dispersed as nanosize particles into $SnO_2$ matrix.

- Molybdenum (Mo)
  Molybdenum (II) acetate ($Mo(OOCCH_3)_2$) was added into the $SnO_2$ sol followed by magnetic stirring.

- Palladium (Pd)
  Palladium (II) acetate ($Pd(OOCCH_3)_2$) was added into the $SnO_2$ sol followed by magnetic stirring.

Figure 12 shows some prepared sols using the above mentioned routines.

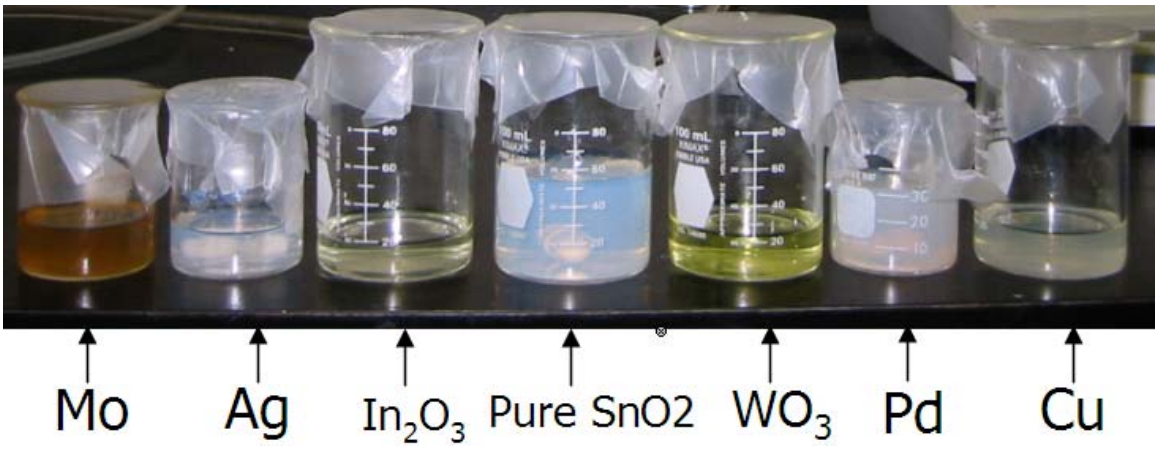


Figure 12 Prepared sols

*2.1.3 $WO_3$*

Tungsten acid (10.0 g) was dissolved in 31.0 ml of methanol. After stirring at room temperature for 15 minutes, 18.0 ml of water (1:25 tungsten acid: water molar ratio) were slowly dropped into the tungsten acid-methanol solution, which was refluxed at 80°C for 20 hours under stirring in air. Afterwards, it was further treated for 5 hours at 110 °C in air. Nanocrystalline $WO_3$ was obtained by annealing the dried powder between

400°C and 700°C for 5 hours. Figure 13 shows SEM picture of $WO_3$ thin film with nanoparticles prepared using this routine.

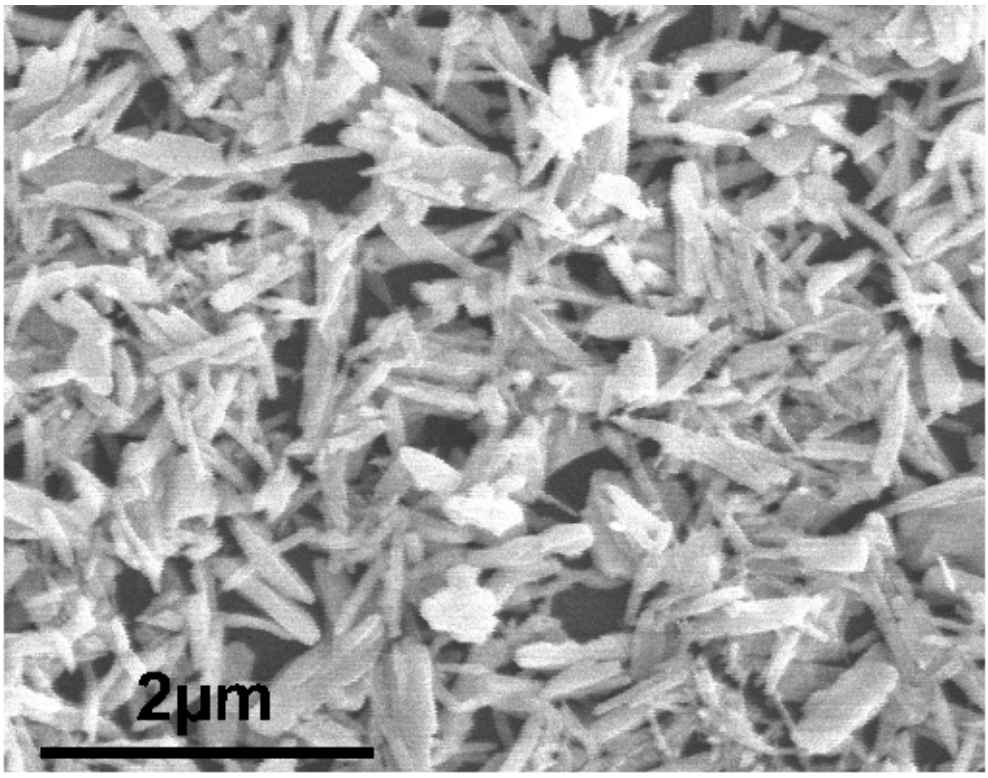


Figure 13 SEM picture of $WO_3$ thin film with nanoparticles

*2.1.4 $In_2O_3$*

Anhydrous indium trichloride ($InCl_3$) in DI water, surplus $NH_3$ is added to get precipitation ($In(OH)_2$), then, using DI water wash these precipitations 7~8 times with the help of flow pumps until the $Cl^-$ is all washed away (use $AgNO_3$ for test), then, add isopropanol and AcAc (acetylacetone) as solvent, use nitric acid adjust PH value so that the sol become clear. Fabricated thin film is shown in Figure 14.

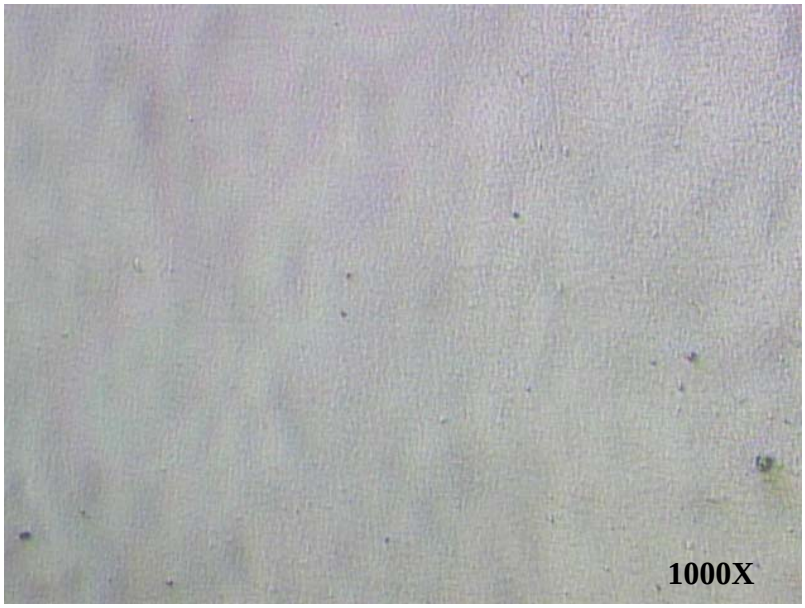


Figure 14 Microscopic picture of $In_2O_3$ thin film with nanoparticles

*2.1.5 Thin film fabrication using sol gel process*

Thin film was fabricated by a spin coating and a subsequent sintering process. A ramp spin coating method was used to increase spinning speed gradually up to 1,000 rpm and keep spinning for 30 seconds total. After air-dry the film for 1 min, this film was ready for another round of spin coating and air-dry if multiple coating is needed to increase the thickness. The coated film was dried in an oven at 100 degree ° C for 4 min. The film sintering was conducted in a furnace (Thermolyne®) with a heating rate of 2° C/min incensement to 500° C and kept it at this temperature for 2 hours. The thickness of $SnO_2$ film was measured by Tencor® Profile Meter. The measured thickness is about ~1μm with single spin coating at 1000 rpm spinning speed. Figure 15 shows the cross section of a film.

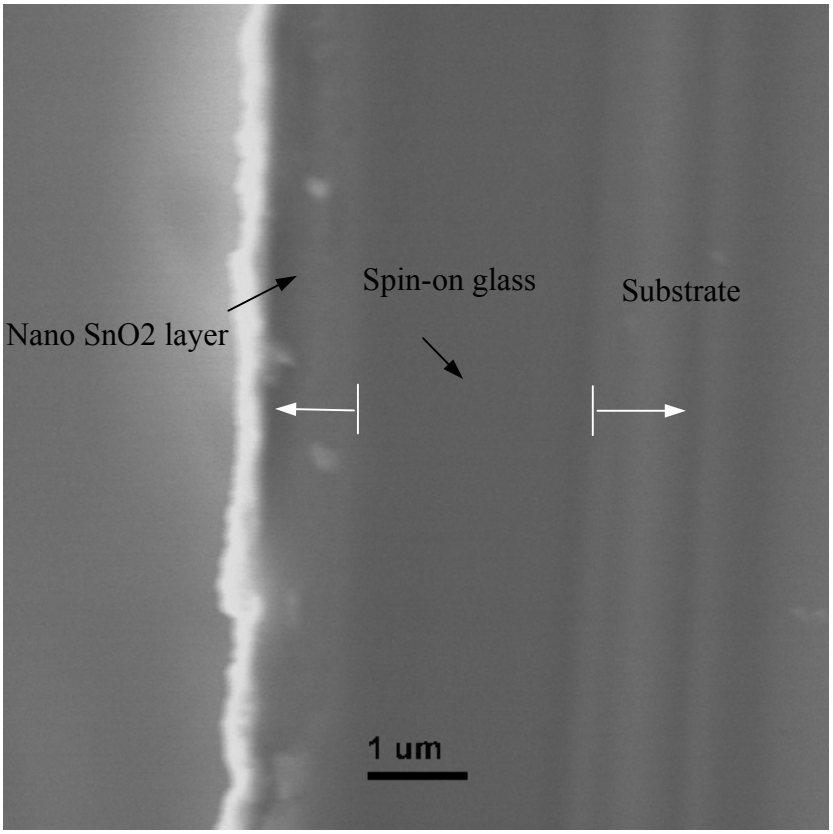


Figure 15 SEM picture shown cross section nano film and the spin-on glass layer

## 2.2 Gas sensor fabrication

### *2.2.1 Design and fabrication of ceramic sensor*

Figure 16 shows a schematic diagram of a micro fabricated SMO ceramic substrate sensor, which includes five major parts, namely substrate, SMO sensing film, sensor electrodes, Pt heater and Pt temperature sensor.

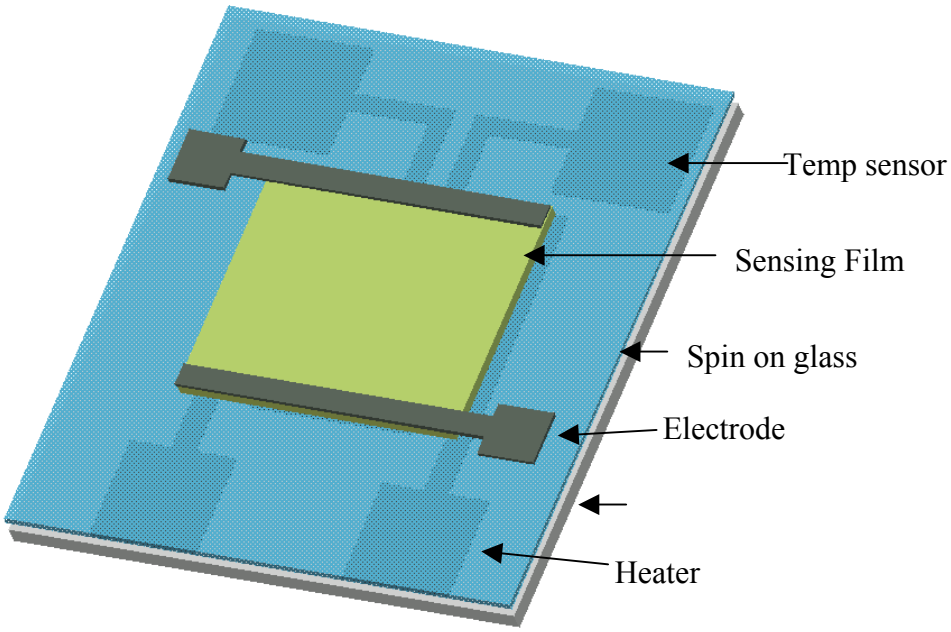


Figure 16 Sketch of gas sensor device

Figure 17 lists major fabrication steps and required masks. Alumina wafer was used as the substrate for better thermal and electrical isolation purpose. To enhance the adhesion to the ceramic surface, about 10s nm layer of Ti is thermal evaporated. 20~25nm thick Pt micro heater and temperature sensor was sputtered followed by a lift off process. High dielectric spin-on glass was spin-coated on as the electric isolation layer. The contacts for heater and temperature sensor are opened by BOE etch using photo resist as etching mask (mask 2,). The gas sensing thin film used for this research was sol-gel derived SnO2105. SnO2 thin film was deposited on by spin coating and it was patterned using mask 3 (Figure 17). Finally, aluminum electrodes were deposited by thermal evaporation and patterned by lift off using mask 4 (Figure 17), after sintering the SnO2 films. Figure 18 shows the detail microscopic view of the fabricated device.

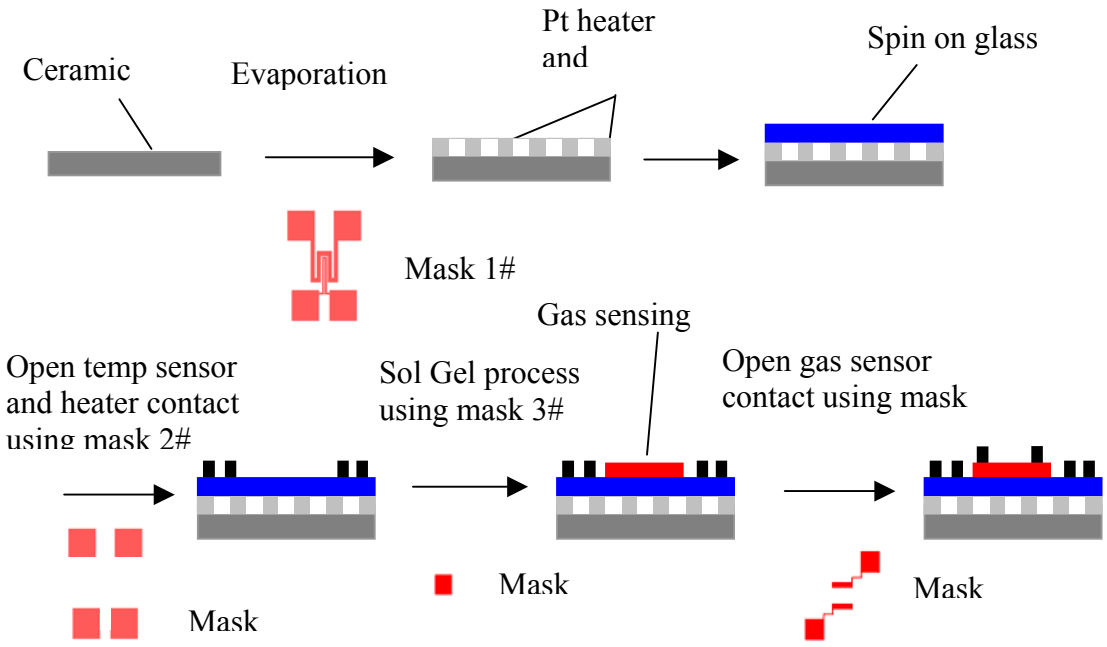


Figure 17 Fabrication process

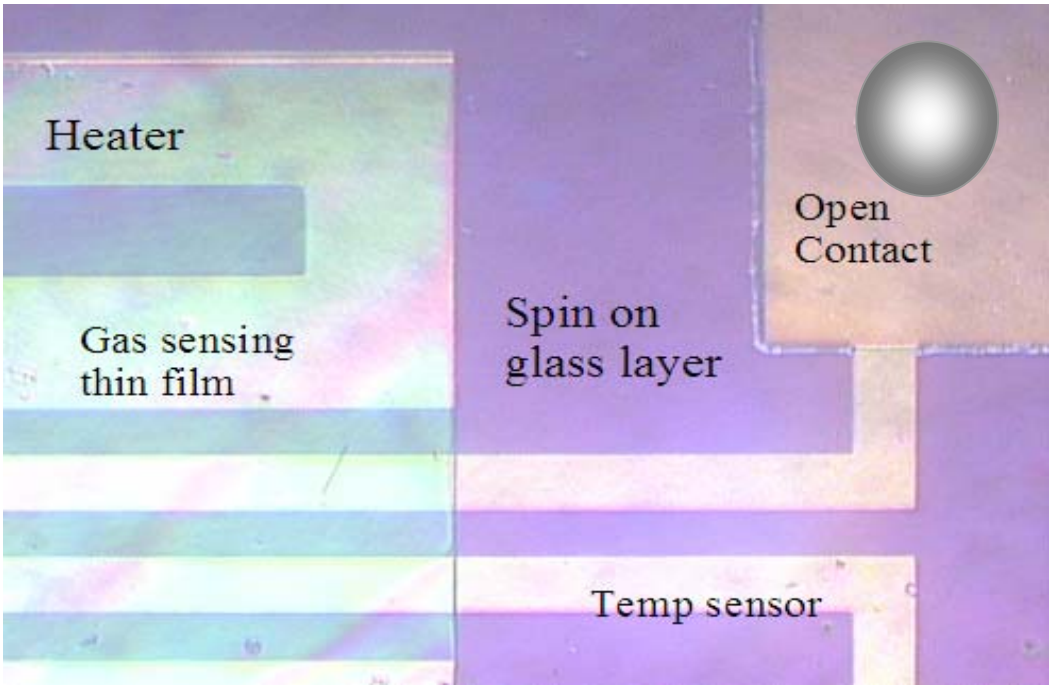


Figure 18 Details of fabricated device under microscope

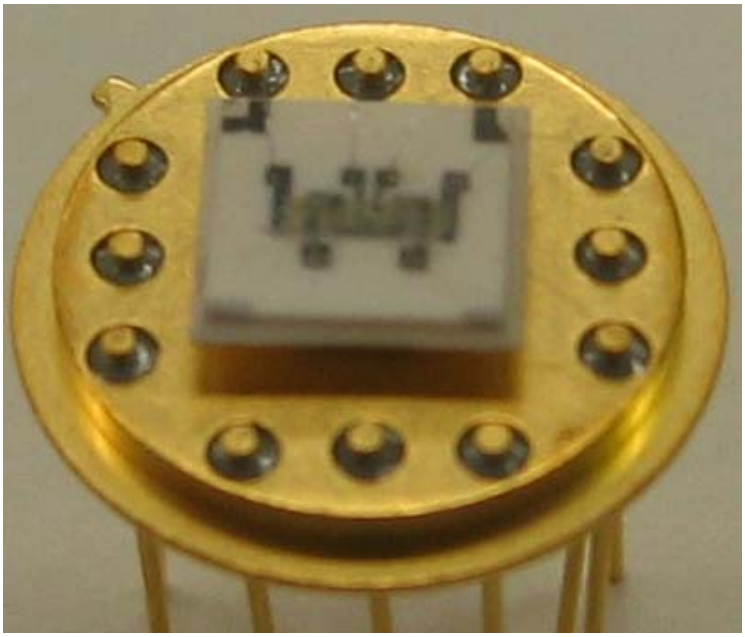

Figure 19 Ceramic sensor after wire bonding

Figure 19 shows the fabricated device fixed on 12 legs package, 1 mil diameter aluminum wires are bonded using ultrasonic wire bonder.

*2.2.2 Design and fabrication of quartz sensor*

Figure 20 shows picture of the novel quartz substrate gas sensor. Quartz wafer was used as substrate and the Pt micro heater/temperature sensor was sputtered on and patterned on the backside. The quartz wafer itself will work as the electric isolation layer, which simplifies the fabrication steps compared with other process. The sensing film and sensing electrode are deposited on the other side of the quartz wafer, since quartz wafer is

transparent; it eliminates the usage of double aligner. Sol gel technique as mentioned in the previous section was used to prepare the nanocrystalline tin oxide layer.

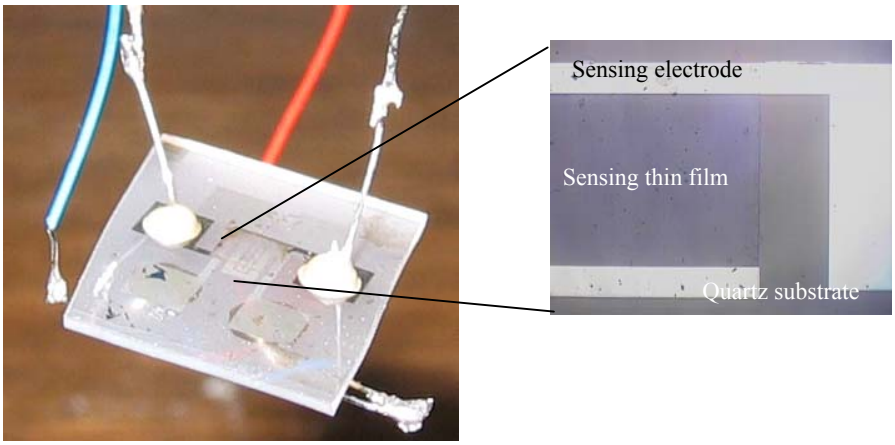


Figure 20 Quartz based sensor

## 2.3 Testing system

The total testing system includes hardware setup and software program.

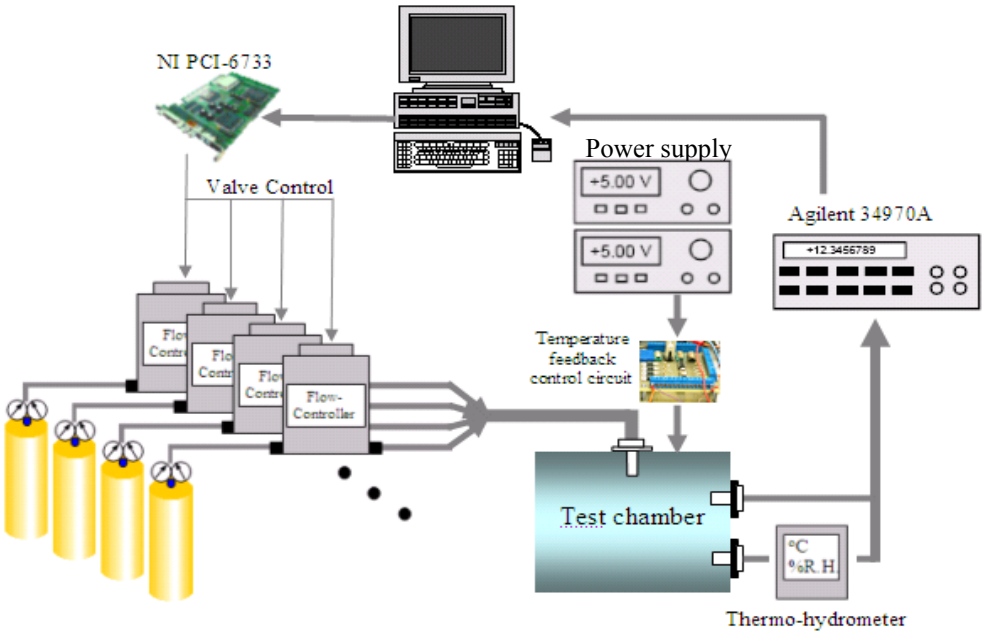


Figure 21 Testing system diagram

Hardware setup consists of five major components, namely, Gas mixing and environmental control, Gas testing chamber, Data acquisition, Signal output (control), Temperature feedback control circuits, and Computer, as are shown in Figure 21.

Software program is the interface between human being and hardware, LabView is used to realize this function.

*2.3.1 Gas mixing and environmental control*

Four Omega MFCs (mass flow controller) are used for gas mixing; they are in different flow ranges, i.e. 2L/min, 200ml/min, 200ml/min and 2ml/min. These MFCs are controlled by computer's analog output signal realized by NI PCI-6733 Analog Output Interface card and LabView program.

Environmental conditions like ambient temperature and relative humidity are also controlled. Gas goes through a big jar of water and generates bubbles, which are used to introduce moisture into testing chamber. Desired relative humidity can be achieved by controlling gas flow rate. To control ambient temperature, a heater is put inside the chamber, with a fan helping air circulation. Desired ambient temperature can be maintained by controlling the heater's power. Refer to Figure 22 and Figure 23.

Omega RH411 thermo-hydrometer is used to monitor the ambient temperature and relative humidity inside the testing chamber.


Figure 22 Testing system

*2.3.2 Gas testing chamber*

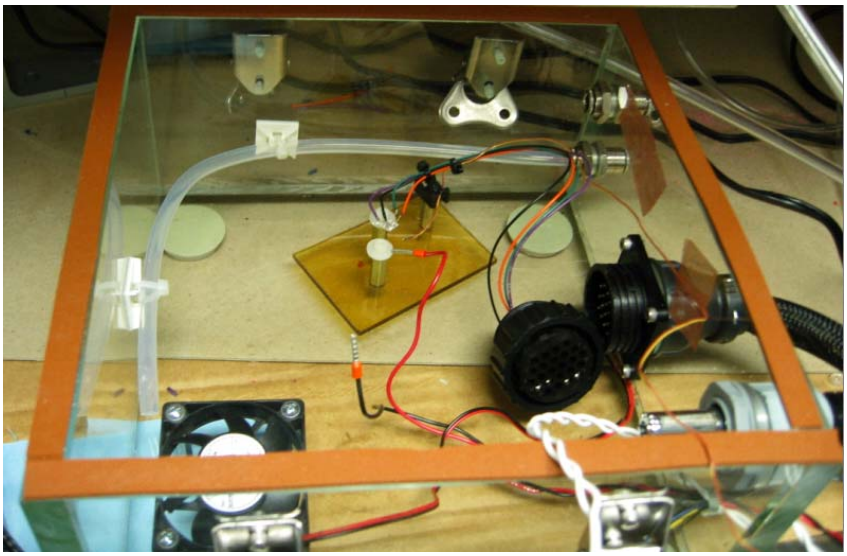

Figure 23 Testing chamber

A homemade gas testing chamber is shown as Figure 23. Wire connector, gas tubing connector and thermo-hydrometer are built on the chamber wall. Seals are used for better airproof.

Table 4 Channel assignment for Agilent multimeter

| | | **Chamber Connector** | | |
|---|---|---|---|---|
| | **Wire Color** | **Pin #** | **Signal Name** | **Signal Type** |
| **Channel (103)** | **BRN** | 1 | Sensor 1 | Resistance |
| **Channel (103)RTN** | **WHT** | 2 | | |
| **Channel (104)** | **RED** | 3 | Sensor 2 | Resistance |
| **Channel (104)RTN** | **WHT** | 4 | | |
| **Channel (105)** | **ORN** | 5 | Sensor 3 | Resistance |
| **Channel (105)RTN** | **WHT** | 6 | | |
| **Channel (106)** | **YEL** | 7 | Sensor 4 | Resistance |
| **Channel (106)RTN** | **WHT** | 8 | | |
| **Channel (112)** | **YEL** | 19 | Device Impedance | Resistance |
| **Channel (112)RTN** | **BLU** | 20 | (Temp Sensor) | |
| **Channel (113)** | | | Temperature (Deg C) | Voltage |
| **Channel (113)RTN** | | | | |
| **Channel (114)** | | | Humidity (%RH) | Voltage |
| **Channel (114)RTN** | | | | |
| **Channel (115)** | | | Opamp + | Voltage |
| **Channel (115)RTN** | | | | |
| **Channel (116)** | | | Opamp - | Voltage |
| **Channel (116)RTN** | | | | |
| **Channel (117)** | | | Power Supply | Voltage |
| **Channel (117)RTN** | | | | |
| **Channel (118)** | | | Device Temperature | Temperature |
| **Channel (118)RTN** | | | | |
| **Channel (119)** | | | Opamp Out | Voltage |
| **Channel (119)RTN** | | | | |
| **Channel (120)** | | | Heater Voltage | Voltage |
| **Channel (120)RTN** | | | | |
| **Channel (121)** | **ORN** | 21 | Heater Current 1 | Current (mA) |
| **Channel (121)RTN** | **GRN** | 22 | Heater Current 1 rtn | |
| **Channel (122)** | **GRY** | 23 | Heater Current 2 | Current (mA) |
| **Channel (122)RTN** | **VIL** | 24 | Heater Current 2 rtn | |

*2.3.3 Data acquisition*

Agilent 24-channel multimeter is used for data acquisition, its 24 channels assignments are listed in Table 4. It uses RS232 and COM port to communicate with computer.

*2.3.4 Signal output (control)*

NI PCI-6733 analog out interface is used for control signal output, its channel assignments are listed in Table 5.

Table 5 Channel Assignment for PCI-6733

| | | **SBC - 68 Module** | | **Mass Flow Cntrl. Conn.** |
|---|---|---|---|---|
| **PCI-6733** | **Wire Color** | **Pin #** | **Analog Outputs** | **Pin #** |
| **DAC 0** | **ORN** | 22 | Mass Flow Cntrl 1 (CO) | 1 |
| **ANOGND** | **BLU** | 55 | | 4 |
| **DAC 1** | **VIL** | 21 | Mass Flow Cntrl 2 (AIR) | 2 |
| **ANOGND** | **BLU** | 54 | | 4 |
| **DAC 2** | **GRY** | 57 | Mass Flow Cntrl 3 (H2S) | 3 |
| **ANOGND** | **BLU** | 23 | | 4 |
| **DAC 4** | | 60 | Heater 1 | |
| **ANOGND** | | 27 | | |
| **DAC 5** | | 28 | Heater 2 | |
| **ANOGND** | | 61 | | |
| **DAC 6** | | 30 | Heater 3 | |
| **ANOGND** | | 63 | | |
| **DAC 7** | | 65 | Heater 4 | |
| **ANOGND** | | 31 | | |

*2.3.5 Temperature feedback control circuits*

Ambient Temperature (AT) is a major factor affecting SMO gas sensor's stability. A novel way to improve temperature stability of SMO (Tin Oxide) gas sensor is by applying a temperature feedback control circuit which is compatible with the MEMS senor fabrication. Built in Pt temperature sensor can precisely detect sensor's working temperature. It provides feedback information to compensate micro heater's current to maintain sensor's working temperature constant, regardless of ambient temperature change. Test results showed that, with this approach, significant improvement of stability has been achieved compared to SMO gas sensors without temperature compensation under the same ambient condition variation. The algorithm realized through hardware circuit, whose advantages include real-time, large feedback gain and low cost. Details of this method will be explained in Chapter 4.

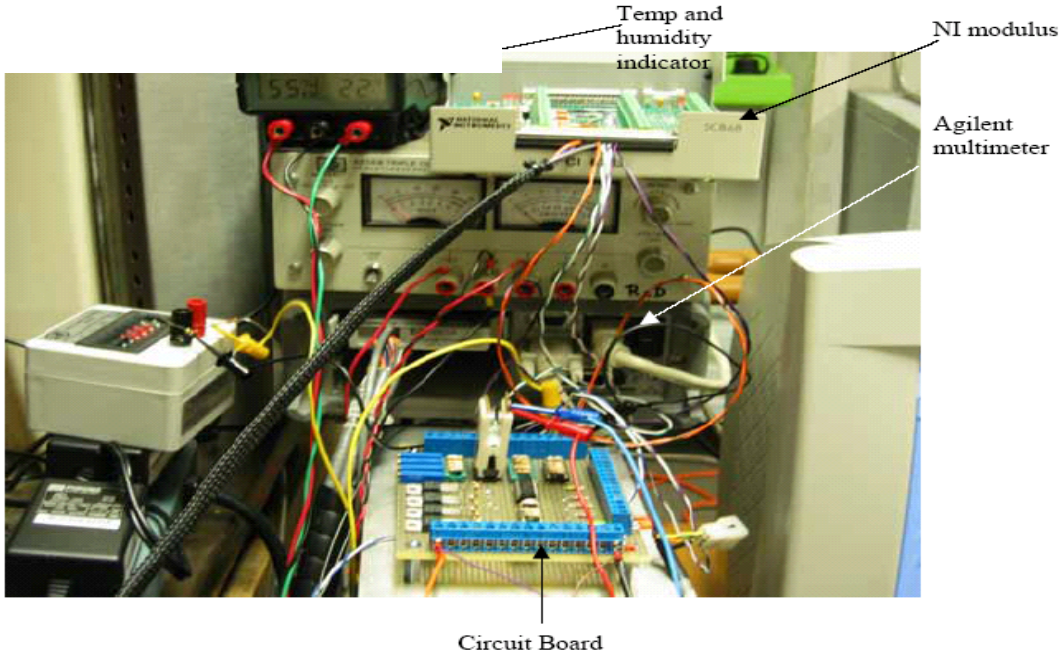


Figure 24 Testing perimeter circuit

Figure 24 shows the picture consisting temperature feedback control circuits and other testing system components like hydro-meter, NI modulus and Aglient multimeter.

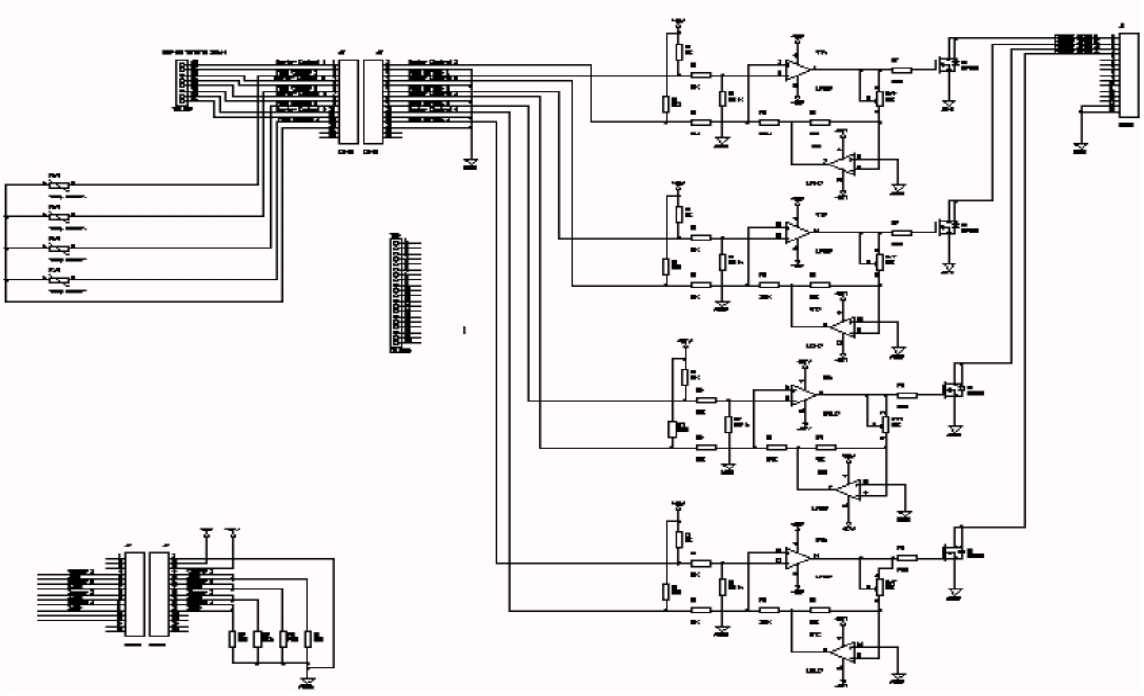

Figure 25  Schematic diagram of board circuit

Figure 25 is the schematic diagram of temperature feedback control circuit. Detailed information about how it works will be covered in Chapter 4.

*2.3.6 Software programming*

National Instruments' LabView is a graphical programming environment designed for measurement and automation tasks with integration with National Instruments'

hardware. This software package provides tools to assist with application development, as well as functions for data acquisition, instrument control, data analysis, and report generation. The latest version is LabView 7 Express.[130,131]

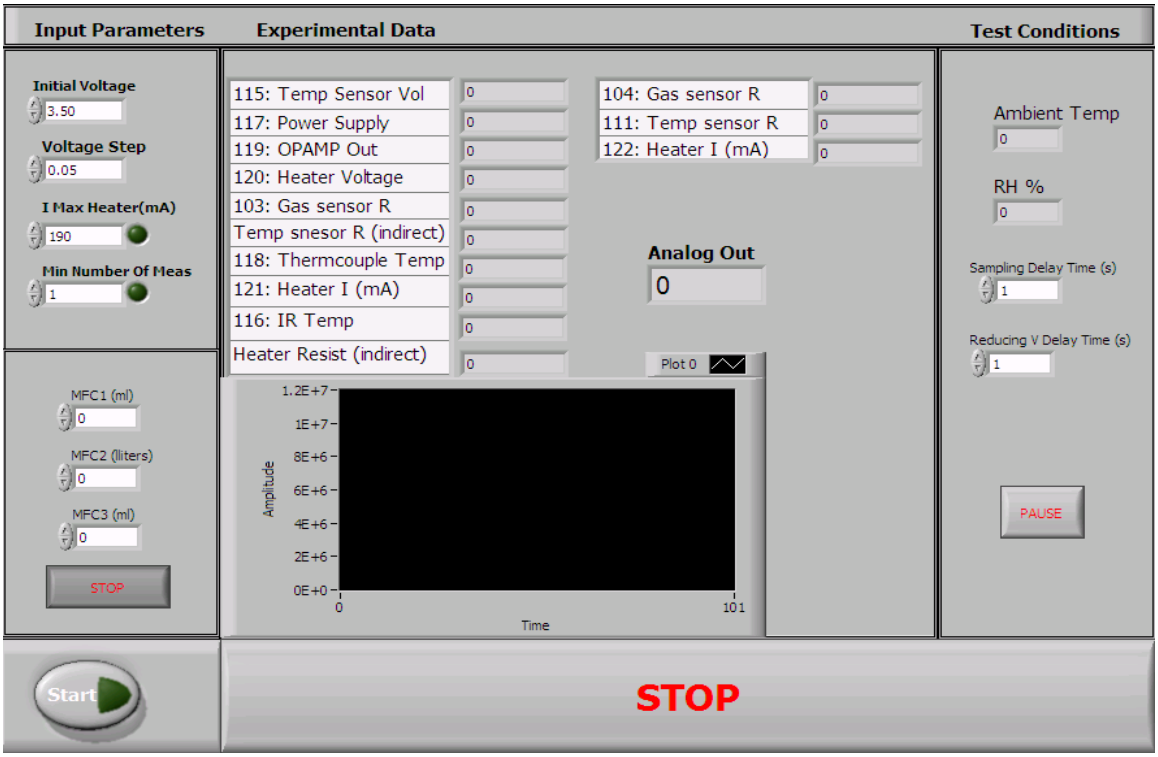


Figure 26 Front panel of test application written using LabView

The whole application program realized using LabView 7 includes module of equipment initialization, module of data acquisition, module of saving and calculation, module of display and plotting and module of control including mass flow meter controlling, sensor heater current controlling, and other system parameters like sampling rate, working temperature point etc. The front panel of the application is shown in Figure 26, and the programming details will not be discussed here. The test results are recorded as Excel files for later processing.

# 3 THERMAL CHARACTERIZATION

## 3.1 Introduction

Temperature is one of the main factors, which determine the sensitivity, selectivity and response time of Semiconductor Metal Oxide gas sensors. For many gas sensitive materials, the sensor performances are enhanced at relatively high temperatures, ranging typically from 400 to 700 K. To set the operating temperatures, a heating resistor, or the micro hotplate, is usually integrated onto the center of a thin dielectric membrane featuring low thermal conductivity, and thus provides good thermal isolation between the substrate and the gas-sensitive heated area.[74,132,133 134,135,136]. A Joule heating module can characterize this electro-thermal behavior of applying voltage or current through a resistive element. This provides information about the relationship between heater voltage and hotplate temperature, which is essential for reproducible gas measurements. The main characteristics to optimize for such devices are the power consumption, the temperature distribution over the sensing area and the robustness.

Pt was selected as the temperature sensor material and heater element. The most important reason is that Pt does not oxidize at elevated temperatures in this application. Another advantage of using Pt is the close-to-linear relationship between Pt's resistance and temperature. (i.e. a constant temperature coefficient). Both Pt heater and Pt

temperature sensor were fabricated at the same time (single layer of Pt deposition, Figure 16 and Figure 17). However, it has been pointed out that the resistance of Pt film depends on the fabrication and the thickness[137]. In order to use the Pt heater and temperature sensor for feedback temperature control purpose, it is important to calibrate the temperature coefficient of sputtered Pt film.

Another issue that needs to be taken into consideration is thermal distribution (homogeneous is mostly preferable) over gas sensitive regions. This issue is very important because it will affect efficiency of temperature feedback control of gas sensor device. Finite Element Analysis software like I-deas is used for thermal simulations.

In future works, optimal design of silicon based microhotplate with lower power consumption and good enough mechanical strength is discussed.

## 3.2 Calibration of Thermal Coefficient of Pt Deposited

Platinum has a positive temperature coefficient. The resistance as a function of temperature can be written as:

$$R = R_0[1 + \alpha(T - T_0)] \tag{11}$$

where $R_0$ is the resistance at the reference temperature $T_0$; $\alpha$ is the temperature coefficient of the resistance, for thin film Platinum, $\alpha \approx 3.927 \times 10^{-3} / K$ .[138]

By controlling the input power, measuring the resultant temperature is used to calibrate the temperature coefficient of the Pt temperature sensor. There are two

approaches of measuring temperature, i.e., direct measurement method and indirect measurement.

*3.2.1 Direct measurement*

- K type thermocouple

The direct temperature measurement method uses thermal conductive paste (glue) or mechanical force to hold a thermal couple probe onto the gas sensor. The size of our fabricated sensor is in small size of 2mm x 2mm, and the heater is located in the center of the device. There is thermal gradient from center to edge and the contact point area also causes inaccuracy. Therefore, the temperature we measured using thermal couple is lower than the actual heater area temperature.

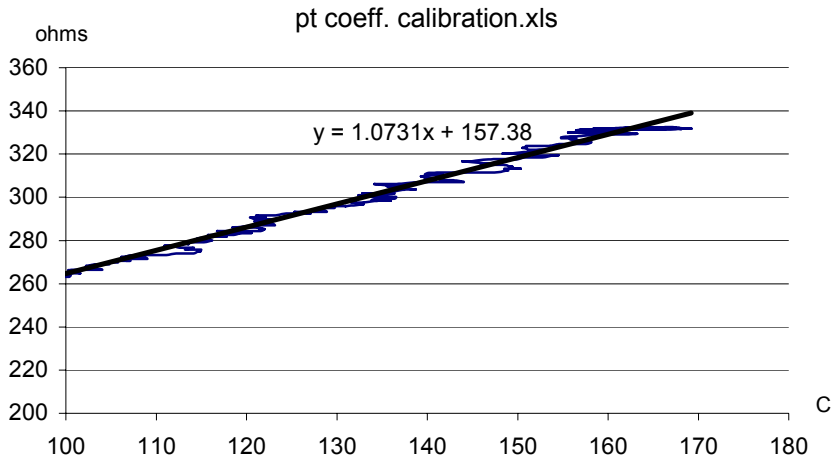


Figure 27 Pt coefficient calibration using direct measurement

- Infrared thermal gun

Infrared thermal gun can eliminate contact inaccuracy. However, the thermal gun measures two points' temperatures and calculate average temperature between two points as measurement value. However, the actual temperature is the peak value between these two points. Therefore, the temperature measured using IR gun is also lower than the actual temperature. Besides, the IR gun also has light converging difficulties.

By using direct measurement for calibration, we got the Pt coefficient value to be ~ $5x10^{-3}$ / K, as is shown in Figure 27. The value is much larger than the one from reference book. This proved that direct measurement method is not accurate enough.

*3.2.2 Indirect measurement:*

Instead of measuring the heated device directly, we used an indirect temperature measurement method. A thermal couple was placed close to the heated device but not in touch with it. The temperature surrounding the Pt sensor was thus measured by this thermal couple. When changing the ambient temperature, both Pt sensor's resistance and its surrounding ambient air temperature were recorded. By doing this, we were able to determine an accurate temperature of the Pt temperature sensor. The calculated temperature coefficient of the fabricated Pt sensor is $3.3x10^{-3}$/K, which is close to value from reference book. We use this Pt temperature coefficient for further calculations.

## 3.3 Design of microhotplate for gas sensors

The design of micro-hotplates leads to two sub-tasks. One task is to develop a device with low thermal loss and high structural stability and the other is to design a heater, which supplies a uniform temperature distribution over the sensitive area.

Suspend type and membrane type are two major microhotplate gas sensor designs, the disadvantage of membrane type structure is the need of double-side alignment for the bulk silicon etch from the backside, and the sloped side-walls obtained by anisotropic etching. The sloped side-walls make the lateral dimensions needed to form a membrane a factor $\sqrt{2}$ larger.

The suspended-membrane-type is completely processed from the front-side (realized by surface micro-machining). Therefore, the suspended membrane is often claimed to be more compatible with CMOS process. The suspended membrane is either formed by anisotropic etch from the front or by sacrificial etching. Figure 28 shows sketch of two types of micro hotplate design, with a) membrane type and b) suspend type.

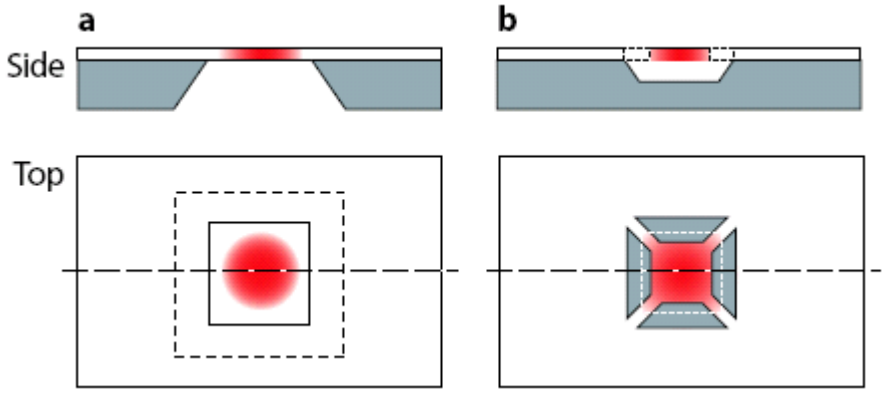


Figure 28 Sketch of two micro hotplate design

## 3.4 Power Consumption

The power consumption of the hotplate structure includes three major parts, namely, conduction, convection and radiation as is indicated in Figure 29. In the following, we will do theory calculations to approximate and estimate power consumptions of our fabricated gas sensor. Dimension of sensor is: 5mm x 5mm x 0.2mm, the heater area is ~ 1.98mm$^2$.

Table 6 Thermal properties of alumina and Pt[139]

| | Aluminum Oxide, Al2O3 | Platinum, Pt | Aluminum wire |
|---|---|---|---|
| Thermal conductivity | 25.08 W/m/K | 73 W/m/K | 216 W/m/K |
| Emissivity | 0.8 | 0.1 | 0.82 |

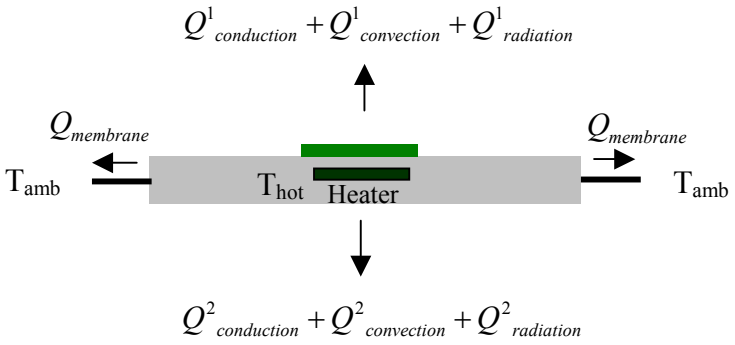


Figure 29 Thermal analysis of a gas sensor device

*3.4.1 Conduction through membrane*

During the experiment, 6 Aluminum wires are used to support the device suspending in the air, the thermal loss caused by membrane conduction can be calculated by Equation (12):

$$Q_{conduction} = \frac{6\lambda_m A_{beam}(T_{hot} - T_{amb})}{l} \quad (12)$$

Where, diameter of Al wire d ≈ 0.1mm, $\lambda_{Al}$=216 W/m/K, wire length l ≈1cm, device temperature $T_{hot}$≈ 140 $^{o}$C, room temperature $T_{amb}$≈23 $^{o}$C:

$$\Rightarrow Q_{conduction} = \frac{6\lambda_m A_{beam}(T_{hot} - T_{amb})}{l} = \frac{6 \cdot 216 \cdot \pi \cdot 0.00005^2 (140 - 23)}{0.01} = 0.119W$$

*3.4.2 Heat losses to air*

Heat losses to the surrounding air can occur due to two different mechanisms, i.e. fluid motion and conduction. Fluid motion can be caused by either external forces or result of temperature differences which lead to density variations in the gravitational field and thus buoyancy forces. The former case leads to heat transfer called *forced convection*; the latter is called free or *natural convection*. When there is no fluid motion, heat is transferred only by *conduction*. We will need to consider only *natural convection* and *conduction* case in our calculation, in the following, heat loss due to conduction and convection to air will be calculated individually.

3.4.2.1 Conduction to Air

For closed membranes, a simple model is obtained by replacement of the square membrane by a round one[140] as depicted in Figure 30.

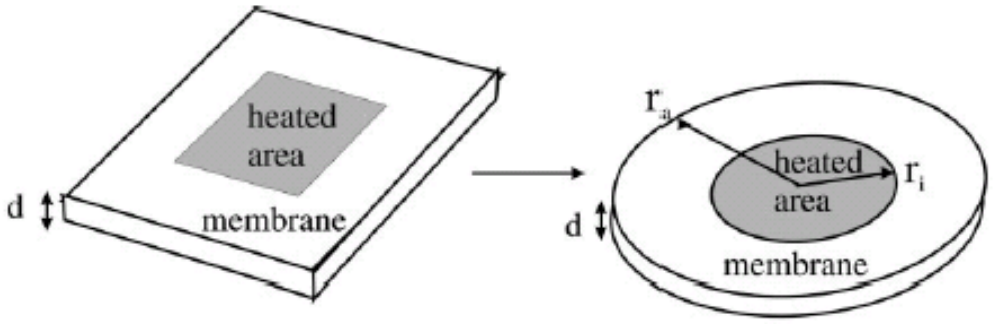


Figure 30 Reduction to one-dimensional heat conduction

This leads to a one-dimensional heat conduction model in cylindrical coordinates, which can be easily solved by Equation (13):

$$Q_{conduction} = \frac{4\pi\lambda_{air}(T_{hot} - T_{amb})}{1/r_i - 1/r_a} \qquad (13)$$

where device temperature $T_{hot} \approx 140\ ^{o}C$, room temperature $T_{amb} \approx 23\ ^{o}C$, the heater area ~ $1.98mm^2$, the equivalent $r_i \approx \sqrt{\frac{1.98}{\pi}} = 0.79mm$ , the device area is $25mm^2$, the equivalent $r_a \approx 2.82mm$, property of air at $140^{o}C$ can be found in Table 7:

Table 7 Air property at 140°C [141,142]

| Specific heat capacity - $c_p$ - (kJ/kg.K) | Thermal Conductivity (W/m.K) | Density - $\rho$ - ($kg/m^3$) | Laminar Kinematic Viscosity $\mu$ ($m^2/s$) | Expansion coefficient $\beta$ x $10^{-3}$ (1/K) | Prandtl's number $P_r$ |
|---|---|---|---|---|---|
| 1.013 | 0.0337 | 0.854 kg $m^{-3}$ | $27.55x10^{-6}$ | 2.43 | 0.695 |

$$\Rightarrow Q_{conduction} = \frac{4 \cdot \pi \cdot 0.0337 \cdot 117}{1/0.79 \cdot 10^{-3} - 1/2.82 \cdot 10^{-3}} = 0.054W$$

3.4.2.2 Heat convection of air

$$Q_{convection} = \alpha A(T_{hot} - T_{amb}) \quad (14)$$

where α is mean heat transfer coefficient $\alpha_m = \frac{Nu\lambda(T_m)}{l}$ (15)

$T_{hot}$ (Plate surface temperature) = 140 °C

$T_{amb}$ (Ambient temperature) =23°C

$\lambda(T_m)$ (Thermal conductivity at Tm=0.5($T_{hot}$+$T_{amb}$)=81.5 °C) =0.03W/mK

$A_s$ (Plate surface area) = 25 $mm^2$

$\rho$ = Air density

$\mu$ = Air Laminar Kinematic Viscosity

$c_p$ = Air specific heat

$k$ = Air thermal conductivity

$\beta$ = Air coefficient of thermal expansion

g = Gravitational constant

Pr = $\frac{c_p \mu}{k}$, Prandtl number

Gr = $\frac{g\beta L^3 (T_{hot} - T_{amb})\rho^2}{\mu^2}$, Grashof number

Ra = $\mathrm{Gr} \cdot \mathrm{Pr}$, Rayleigh number

L = Plate length (For horizontal plates, this value is the surface area divided by the plate perimeter[143].)

$$Nu_m = 0.766(Gr\,\mathrm{Pr})^n = 1.523 \tag{16}$$

$$where, \quad Gr = \frac{\beta g \Delta T L^3 \rho^2}{\mu^2} = 44.69 \tag{17}$$

$$n = 0.2,\ L = \frac{5^2}{4 \times 5} = 1.25mm, \mathrm{Pr} = 0.695\ at\ 140C$$

$$\Rightarrow \alpha_m = \frac{1.523 \times 0.03}{1.25\text{E-}3} = 36.55$$

Qconvection ≈ $2\alpha A(T_{hot}-T_{amb})$ =2 x 36.55x$(0.005)^2$ x 117=0.214W

*3.4.3 Radiation.*

$$Q_{radiation} = G_{rad}\delta\varepsilon(T_{hot}^4 - T_{amb}^4) \tag{18}$$

$\varepsilon_{Alumina}$: 0.8 according to Table 6, δ=5.7 E-8w/$m^2k^4$, $G_{ad}$=2A

$$Q = 2 \times (0.005)^2 \times 5.7 \cdot 10^{-8} \times 0.8 \times (140^4 - 23^4) = 0.00109\mathrm{W}$$

### *3.4.4 Result and conclusion*

To sum the previous calculated items, we got the total value of power consumption of $Q \approx 0.119W+0.054W+0.214W+0.00109W = 0.388W$. Based on this calculation, we can make conclusion that heat loss is mainly caused by nature convection as well as conductive heat transfer through device and air. However, if there is forced convection existing, there would be quite larger heat loss caused by that. This leads two important issues in order to minimize microhotplate gas sensor's power consumption: one is to optimize device structure so as to minimize conductive heat loss through device body; the other is to use housing cap to prevent heat loss caused by forced convection of surround air. Sensor design improvement will be discussed in the later section of this chapter.

## 3.5 FEM Analysis

Many scientific problems, like the heat transport in a solid, are described by partial differential equations (PDE). But in general it is too difficult or impossible to solve these problems analytically for a given geometry. Therefore, we have to solve them numerically. The numerical solution can be split into three steps. The first step is to divide the domain (geometry of the model) into subdomains. This is called "meshing". Then the differential equations have to be approximated in every subdomain. Hereby different methods like Finite Differences, Finite Boxes, and Finite Elements etc. can be used.

*3.5.1 I-Deas thermal simulation*

In order to better understand the thermal distribution of the gas sensor device, FEM thermal simulation is performed using I-Deas$^{TM}$. Power (0.4W) is applied to the heater, Figure 31 shows the simulation of thermal distribution of sensor's front side, the largest temperature differences between maximum value of 91.7 $^{o}$C (Red) in the heater area and the minimum value of 85.3 $^{o}$C (Blue) at the corner is 6.4 $^{o}$C.

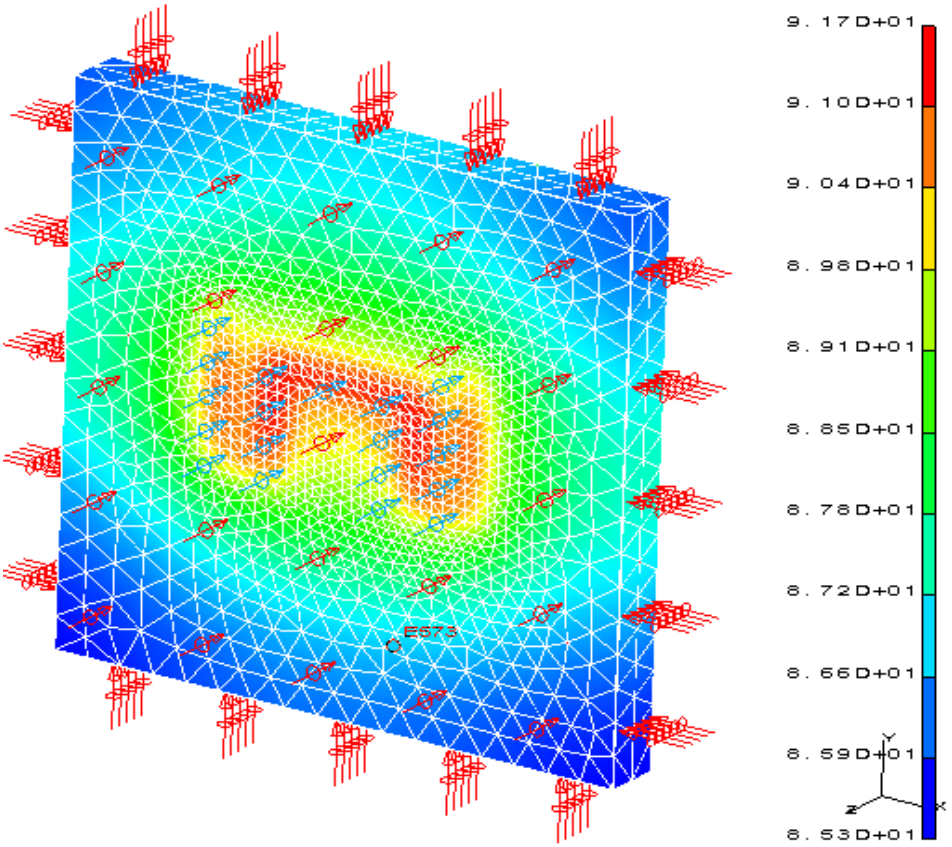


Figure 31 Front side of device

Figure 32 shows thermal distribution on back side of gas sensor. The heater areas temperature difference between two surfaces is ~ 0.2 $^{o}$C, almost same temperature

distribution can be found in other areas. Considering the theoretical calculation of power consumption in the previous section, i.e. 0.388W at 140 $^{o}$C, we got 0.4W at 92$^{o}$C in this simulation. This indicates that FEM thermal simulation is close to the theoretical calculation, and small difference can be explained by assumptions and approximations during calculation.

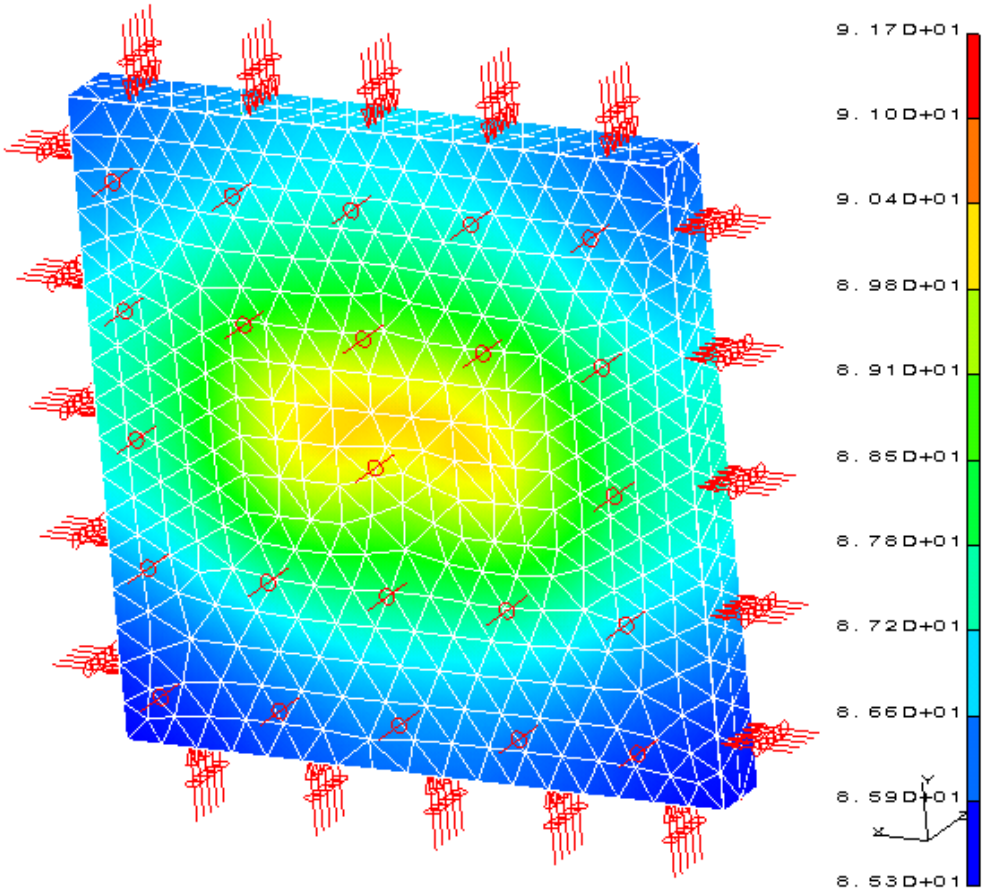


Figure 32 Back side of device

*3.5.2 MatLab electric field simulation*

The electro-thermal model of microhotplate is Joule heating model, Joule's law gives the amount of heat $Q$ generated by current $I$ flowing through a resist with resistance $R$ for a time $t$. Voltage is applied to the pad, it is good if we know the electric field distributed along the resistor so that we can optimize heater design to prevent problems like fatigue and thermal expansion differences. Figure 33 is the MatLab simulation result which shows electric field distribution through heater resistor. Electric field is evenly distributed except that peaks appear at corners. There is not much power consumed on pads, which is a desired result.

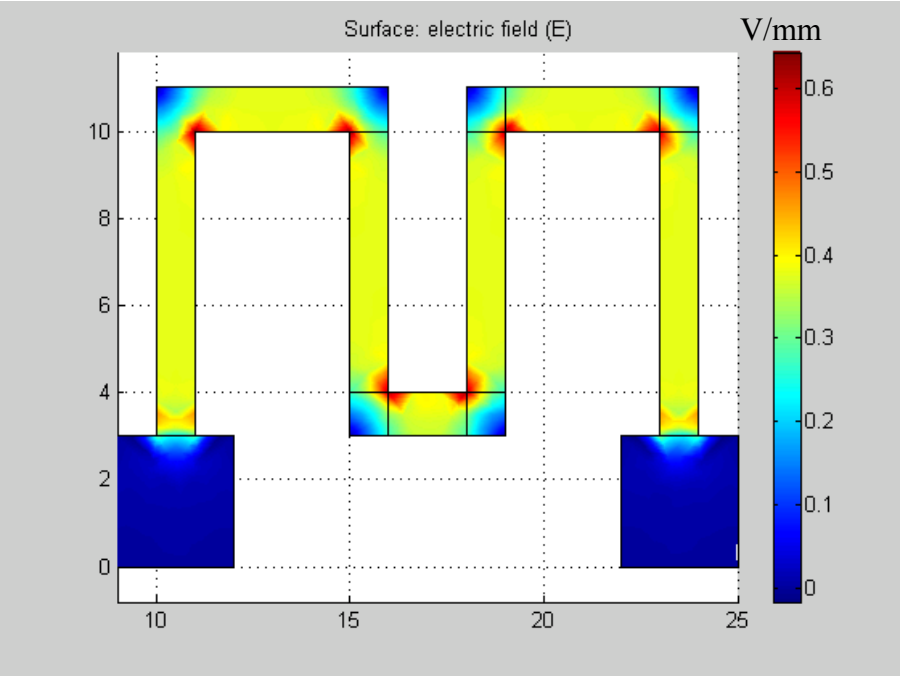


Figure 33 MatLab simulation of electric field distribution

## 3.6 Future Improvement Design

As is mentioned in the previous section, two aspects need to be taken into consideration in order to minimize gas sensor's power consumption: optimized microhotplate structure and housing package.

### *3.6.1 Optimization of microhotplate design*

With help of computer simulations, it is possible to optimize the microhotplate resistor geometry in order to achieve a temperature plateau in the active area. Suspended membrane structure shown in Figure 28 (b) is helpful in thermal isolating gas sensor from surrounding air and is also compatible with the fabrication process. The sensitive layer of micromachined metal oxide gas sensors is deposited onto a thin dielectric membrane of low thermal conductivity such as $Si_3N_4$ or $SiO_2$. The suspended membrane is formed by anisotropic etch from the front and four beams are used to support the membrane. Good thermal isolation can be achieved so that the substrate itself stays nearly at ambient temperature while the gas sensor works at an elevated temperature. The mounting of the sensor element becomes therefore much easier than for an overall hot ceramic sensor element, and control and signal-processing electronics can be integrated on the same substrate if desired.

Either doped polysilicon or sputtered platinum can be used as heater, which is fabricated on $SiO_2$ / $Si_3N_4$ substrate. FEM can be used for design to determine optimal

substrate thickness so that heater loss through membrane conduction is minimized to lowest level, while the mechanical strength is robust enough for a gas sensor device.

### 3.6.1.1 Thermal simulation

Figure 34 shows the thermal distribution of 2μm thickness $Si_3N_4$ membrane, compared to 2μm thickness silicon membrane shown in Figure 35.

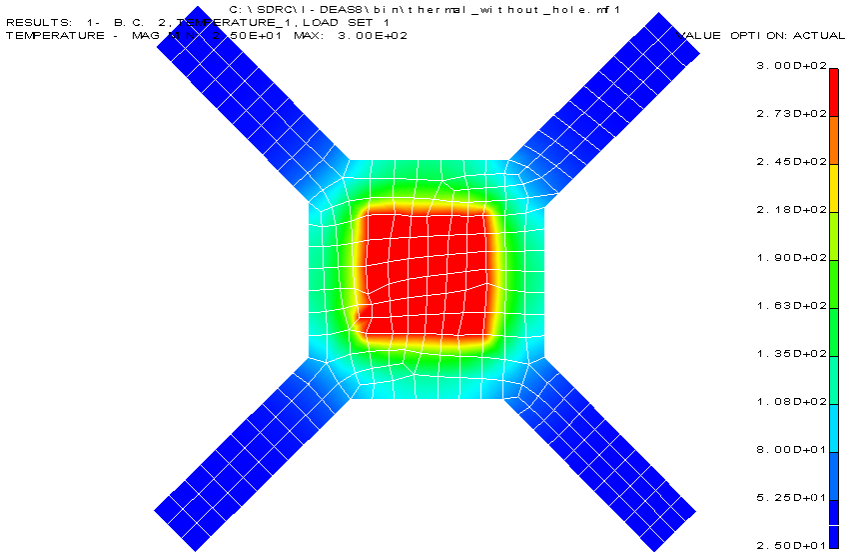


Figure 34 2μm thickness $Si_3N_4$ membrane

Since silicon nitride's thermal conductivity is much smaller than that of silicon, for the same thickness of membrane, thermal distribution of $Si_3N_4$ membrane is smaller than silicon one. Figure 36 and Figure 37 show the thermal distribution of 5μm and 20μm thickness $Si_3N_4$ membrane, individually. It is obvious that, when substrate gets thicker,

the heat is more easily transferred outside the heater area. This phenomenon can also be explained by $Q_{conduction} = \frac{6\lambda_m A_{beam}(T_{hot} - T_{amb})}{l}$ **(12)** i.e. heat loss is proportional to thermal conductivity λ, and membrane thickness.

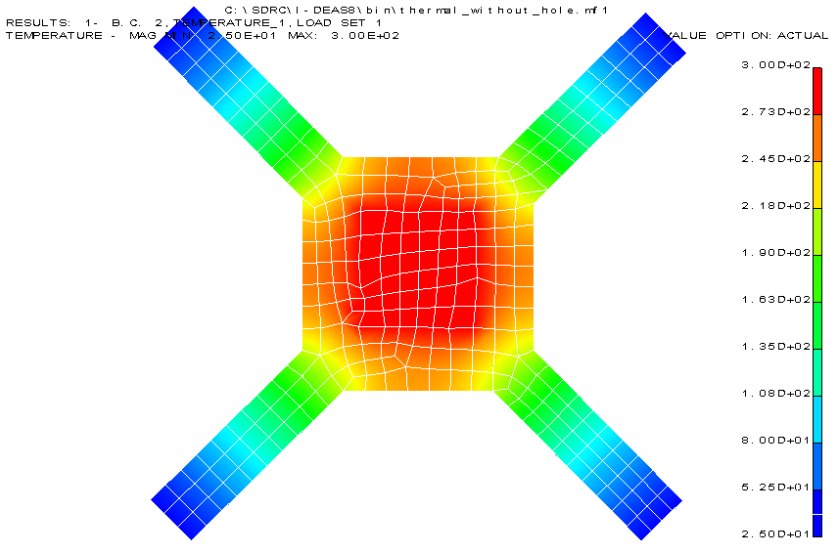


Figure 35 2μm thickness silicon membrane

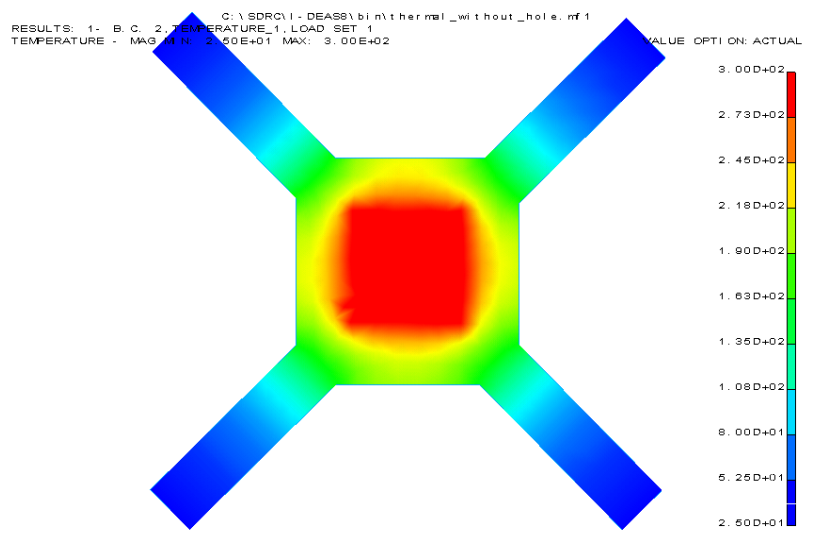


Figure 36 5μm thickness $Si_3N_4$ membrane

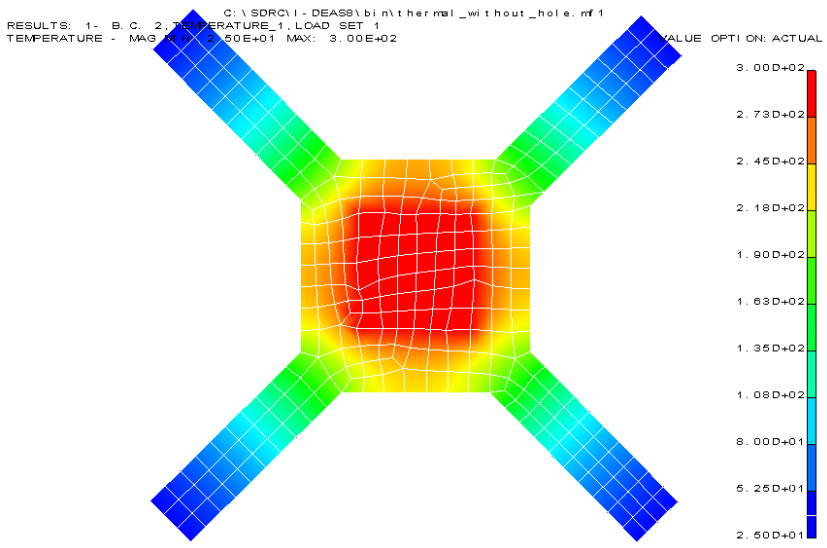


Figure 37 20μm thickness $Si_3N_4$ membrane

3.6.1.2 Mechanical strength

Based on the analysis, we know that, the thinner the substrate, the less of heat loss caused by conduction. However, when a microhotplate on a suspended membrane is designed, mechanical strength is also an important factor that needs to be taken into consideration. The maximum stress $\sigma_m$ of a bending beam can be calculated by[144]:

$$\sigma_m = \frac{Mc}{I} \quad , \; I = \frac{1}{3}bh^3 \qquad (19)$$

Where, M is moment of force (gravity force in this case), I is moment of inertia of beam, and c is the largest distance from the upper surface to the nature surface, b is width of the beam and h is height of the beam.

Figure 38 shows the Von Mises stress distribution of 5μm thickness $Si_3N_4$ membrane, the load is weight of the sensor body. It is obvious that the maximum stress is

located at the end of beams, and should be less than $Si_3N_4$'s yield stress to prevent breakage.

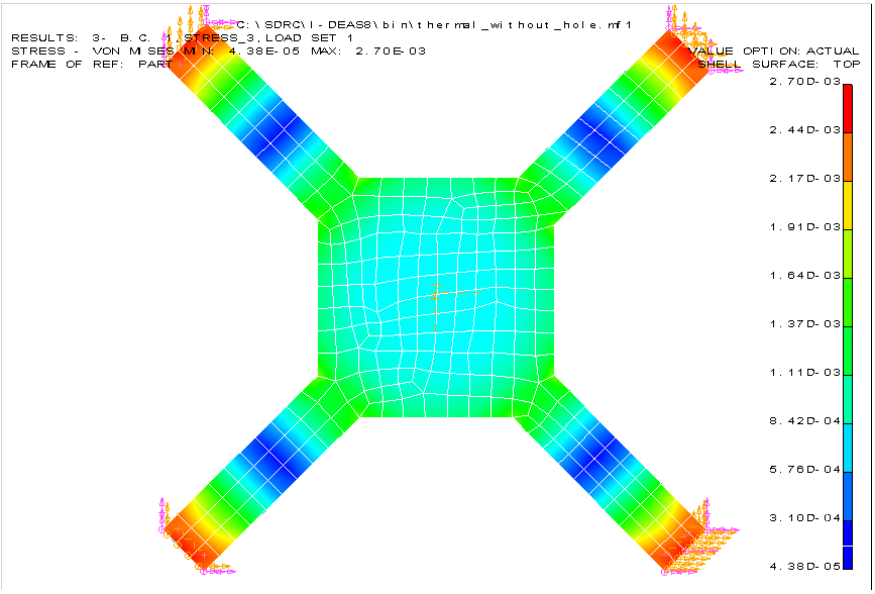


Figure 38 Mechanical strength analysis of 5um thickness membrane

3.6.1.3 Summary

To optimize the sensor design, we should consider both thermal issue and mechanical issue, and make compromise of several contradictory factors to fulfill the requirements. For example, both substrate thickness and beam width are proportional to mechanical strength, refer to Equation (19), and while proportional to heat loss caused by conduction, refer to Equation (12). However, there are also some other factors that need to be taken into consideration, for example, instead of pure $SiO_2$ film or $Si_3N_4$ film, $SiO_2$/ $Si_3N_4$ film is more often used as substrate. This makes simulation more complex due to

combination of two materials. Conducting wire (for heater power line and sensor signal read out) going through beams also add more variables to this problem.

*3.6.2 Housing package*

As is shown in Figure 39, the package of gas sensor should include a housing container which can provide protection and prevent air convections as well. Flame arrestor can make an intrinsically safe system. Active charcoal filter and silica gel pad can partially get rid of contamination and humidity influences.

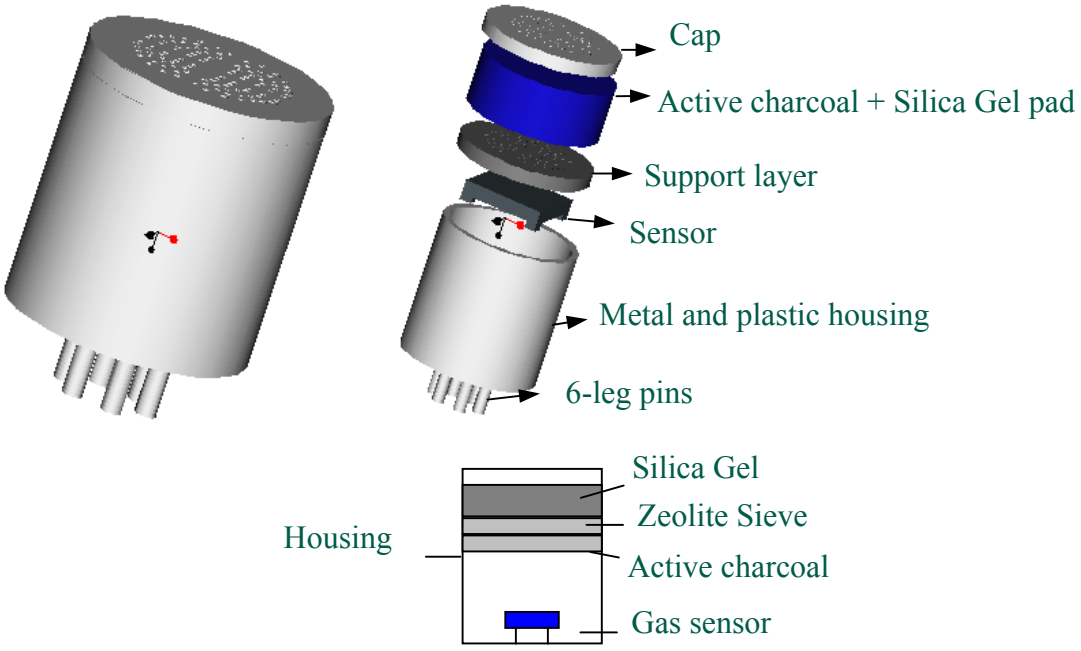


Figure 39 Gas sensor packaging

# 4 TEMPERATURE EFFECTS ON GAS SENSORS

## 4.1 Introduction

An important issue regarding SMO sensor's application is environmental influence, in terms of temperature variation and relative humidity caused instability (drift). When environmental temperature increases, the gas sensor's resistance drops. Otherwise, the resistance increase if the environment getting cold. Since SMO sensor's resistance change caused by chemical gas absorption is the sensing mechanism for chemical detection, the environmental temperature change induced resistance variation will cause serious problem if it is not fully accounted.

Published literatures have shown that efforts have been made on this issue, however, most of them were focused on fabrication induced instability. For example, H. Esch et al.[145] investigated the stability of gas sensor's Ti/Pt heater elements influenced by diffusion and oxidation processes taking place during thermal treatment. However, stability of heater and its power does not mean the gas sensor won't be affected by ambient temperature's fluctuation.

Our test results have shown that a few degree of ambient temperature fluctuation works as a superposition to device working temperature. As a result, this will cause gas sensor's resistance change thus fools the chemical detection. In order to take this into

account, Figaro's TGS sensor configuration[146] and some other designs[147] have used external themistors to compensate the induced temperature effect. This technique requires a fixed temperature-resistance relationship of the gas sensor. However, this is not guaranteed, due to the fact of variation in sensing material and fabrication, range of temperature change, as well as interaction with gases the sensor in access. Therefore, it is necessary to control and maintain the gas sensor's working temperature at a constant level. The environment temperature induced noise in the detection can thus be prevented. Commercial temperature stabilization circuits are also available from Capteur[148]. The sensor heater forms part of a Wheatstone bridge. The current through the heater is controlled so as to maintain the sensor heater at constant resistance. In other word, the heater is also used as the temperature sensor to get a simple design.

However, the drawback of such scheme is the temperature measured by the heater is not the sensor's temperature, especially during the heating time. Pt has much better thermal efficiency than ceramic substrate. This means Pt heater (small volume of material) can reach the required temperature much faster than the sensor's ceramic substrate. For example, during temperature compensation heating (environment is cool), the heater's temperature has to be higher than the required temperature (provide extra power). The extra heating current and the time depend on the environmental temperature, the sensors mass, as well as the thermal convection (cooling). Therefore, it may be very difficult to achieve the thermal balance with this design.

## 4.2 Temperature-Resistance Relations

According to semiconductor theory[149], the relationship between semiconductor's resistance and temperature can be approximated by a nonlinear function. The resistance as a function of temperature can be described as: $R_T = Ro\ e^{[\beta(1/T - 1/To)]}$, where $R_T$ and Ro are the resistance values at absolute temperatures *T* and *To* (on the Kelvin scale), respectively. $\beta$ is a constant over a limited temperature range and it is used to characterize material's property. From this relationship, one can make conclusion that SMO sensor's resistance is greatly affected by temperature. Figure 40 shows this relationship: when device temperature changes from room temperature to 160°C, the sensor resistance decreases from ~12M ohms to below 1M ohms.

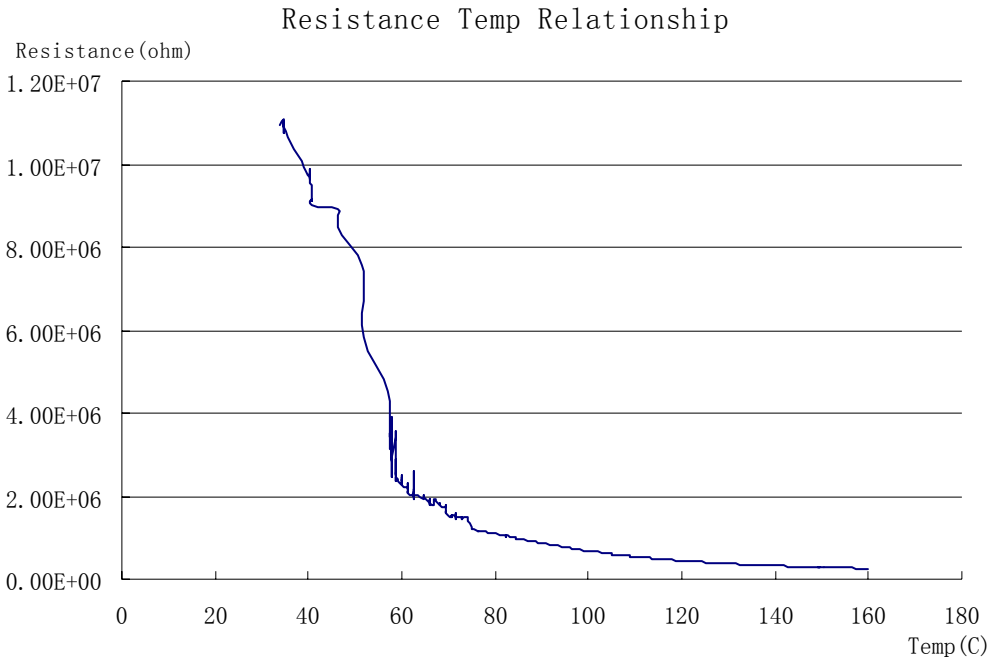


Figure 40 Temperature-Gas Sensor Resistance Relations

## 4.3 Ambient Temperature Affection

Fabricated SMO sensor is normally calibrated in house at room temperature before shipped out for service. The sensor's working power is normally fixed to maintain the working temperature, due to the tested condition. However, what happens if the environment temperature changes, just a few degrees, for example, during day and night? An experiment has been performed specifically.

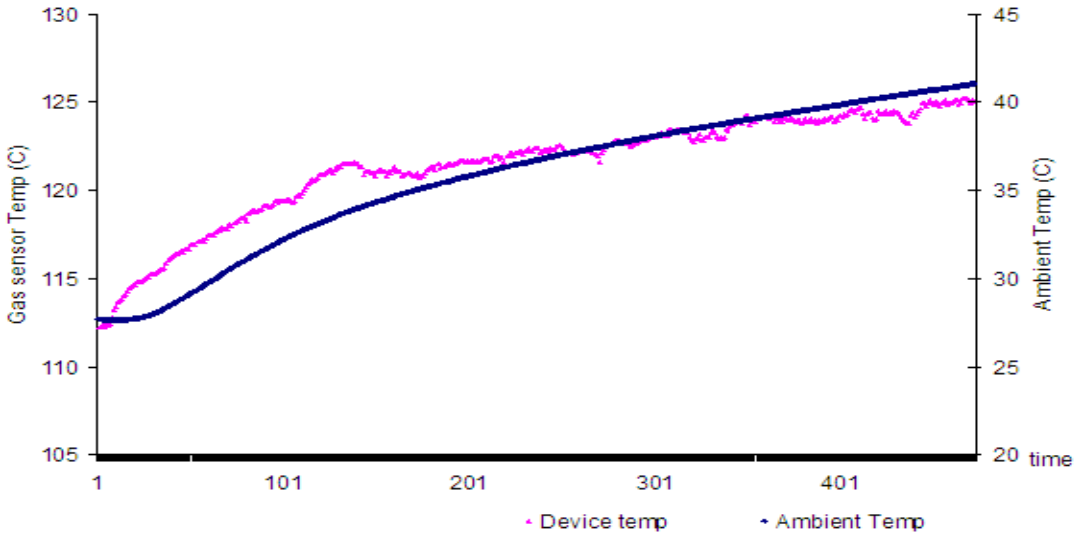


Figure 41 Ambient temperature effect as a superposition

As test results shown in Figure 41, when the ambient temperature changes from 27°C to 41°C (ad hoc night to day in summer in Florida), the measured device temperature is changed from 112°C to 125°C. This means that the change of ambient

temperature will be a superposition on sensor's working temperature, and it has to be compensated to prevent false signals.

## 4.4 Feedback Temperature Control Circuit Design

### *4.4.1 Principle*

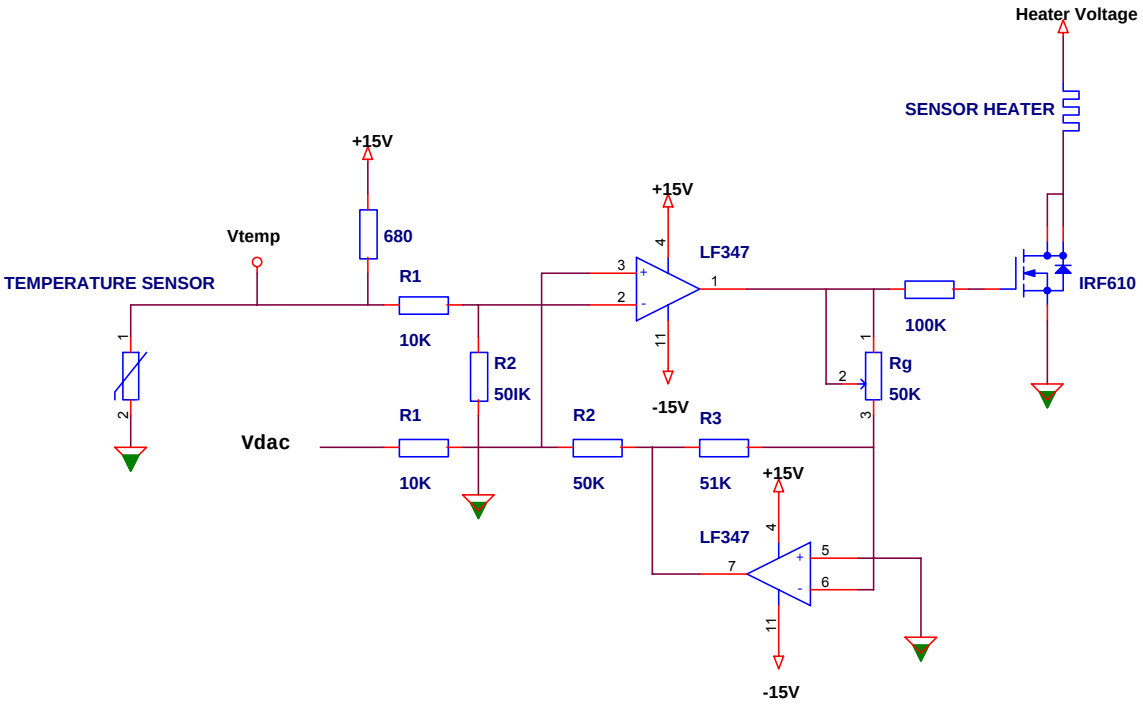


Figure 42 Feedback temperature control circuit for gas sensor

As is shown in Figure 42, the working principle of the temperature feedback control circuit is[150] : For a predetermined sensor's working temperature, a certain power consumption of the heater is required, based on device power consumption. The required power corresponds to an approximately certain current of the heater. The required

heater's current in turn is corresponding to a desired gate voltage $V_g$ of a power MOSFET. Therefore, the required working temperature is realized by using a form of fixed voltage, for a specific gas sensor device. If the ambient temperature changes, Pt temperature sensor will "sense" it (due to the resistance change). It is necessary to provide a differential voltage to the feedback control circuit. This differential voltage will be amplified to control the heater current in order to compensate the ambient temperature effects.

*4.4.2 Calculations*

a. Differential operational amplifier feedback circuit gain calculation

$$Vo = \frac{R_2 R_g}{R_1 R_3}(V_{temp} - V_{DAC}), \rightarrow gain = \frac{R_2 R_g}{R_1 R_3} \tag{20}$$

In this circuit design, $R_2$=50k, Rg=25K, $R_1$=10k, $R_3$=50k, → gain=2.5

b. MosFET voltage-current transconductance

At working point, i.e. drain current is 70mA ($V_{gate}$=3.62V), MosFET voltage-current transconductance=δI/δE= 0.224 siemens

c. Temperature sensor's resolution calculation:

Pt sensor 's resistance at room temperature is 295ohm, for a dividing 680ohm resistor and 15V Vcc, the calculated resolution is 15.3mV/ohm, assume pt's thermal

coefficient a is equal to $3.3x10^{-3}$ C/ohm, then 1 degree C of temperature change will cause 0.975ohm change, and thus 14.91mV change.

In summary, 1 $^{o}$C of ambient temperature change will cause 8.34mA compensating heater's current change, which is far larger than is needed (at working point, $V_{gate}$=3.62V, the heater's current is approximately 70mA, which is corresponding to around 150C working temperature). Since it is a real time feedback, this large enough gain will guarantee fast response and thus achieve equilibrium very quickly.

## 4.5 Results

### *4.5.1 Circuit performance*

An experimental study has been conducted to examine the performance of the abovementioned temperature feedback control circuit. Three dummy temperature sensors with different resistance (52ohm, 100ohm and 200ohm respectively) have been used during the study to simulate 3 different temperature situations.

The relationships of heater's current versus temperature sensor's output voltage are shown in Figure 43. The temperature's output voltages between resistors (52ohms, 100ohms and 200ohms) are also indicated in Table 8. Taking the 200ohm- temperature sensor output voltage as a reference, we can calculate voltage offset for other temperature sensors. For example, voltage offset for the 50ohm resistor is 2.34 V and 1.49 V for the 100-ohm resistor (Table 8). If we shift the 100ohm voltage-current curve along the x-axis

(temperature sensor's output voltage) by adding a calculated offset voltage (1.49 V), it is perfectly overlapped with the 200ohm's curve (Figure 43).

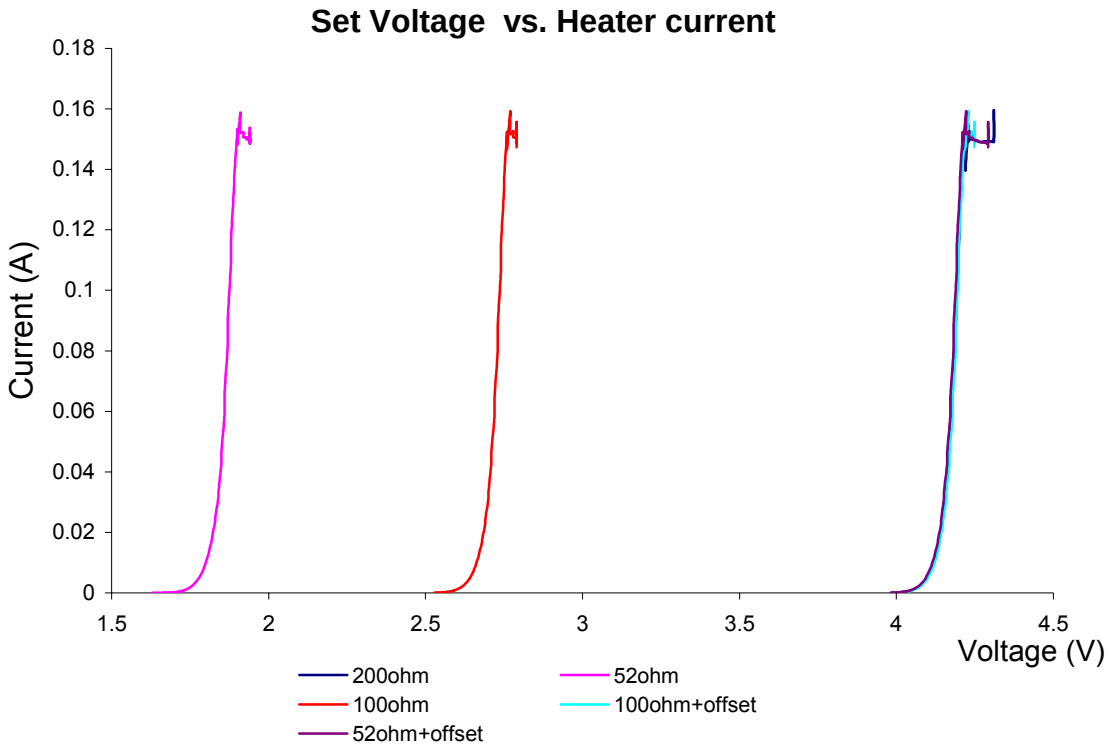


Figure 43 Dummy temperature sensor experiments

Table 8 Temperature sensor output voltage resolution and calculated offset voltage

| Dummy Temperature sensor value | Resolution (V/C) | Offset Voltage (V) |
|---|---|---|
| 52 ohm | 0.019062 | 2.34 |
| 100 ohm | 0.016787 | 1.49 |
| 200 ohm | 0.013186 | 0 |

This test shows that, changes of temperature sensor's output voltage (decrease or increase) caused by the ambient temperature variations will make voltage-current curve shift along the x-axis (left or right, Figure 43). It is necessary to use the offset to compensate the change. As the result, heater's current would be adjusted (decease or increase) accordingly.

Assume temperature sensor's resistance at room temperature is 295ohm, for a dividing 680ohm resistor and 15V Vcc, the calculated resolution is 15.3mV/ohm, assume Pt's thermal coefficient a is equal to $3.3x10^{-3}$ C/ohm, then $1^{o}$C of temperature change will cause 0.975ohm change, and thus 14.91mV change, which will cause 8.34mA compensating heater's current change, which is far larger than that is needed (at working point, $V_{gate}$=3.62V, the heater's current is approximately 70mA). Since it is a real time feedback, this large enough gain will guarantee fast response and thus achieve equilibrium very quickly.

*4.5.2 Sensor baseline resistance stability*

Micro fabricated gas sensor with temperature feedback control circuit was tested in changing ambient temperature conditions. The gas sensor was put into a closed chamber, which temperature is controlled with a heater and a fan installed away from where gas sensor is mounted. When the heater was powered on and the ambient temperature was increased gradually from around 25C to $42^{o}$C.

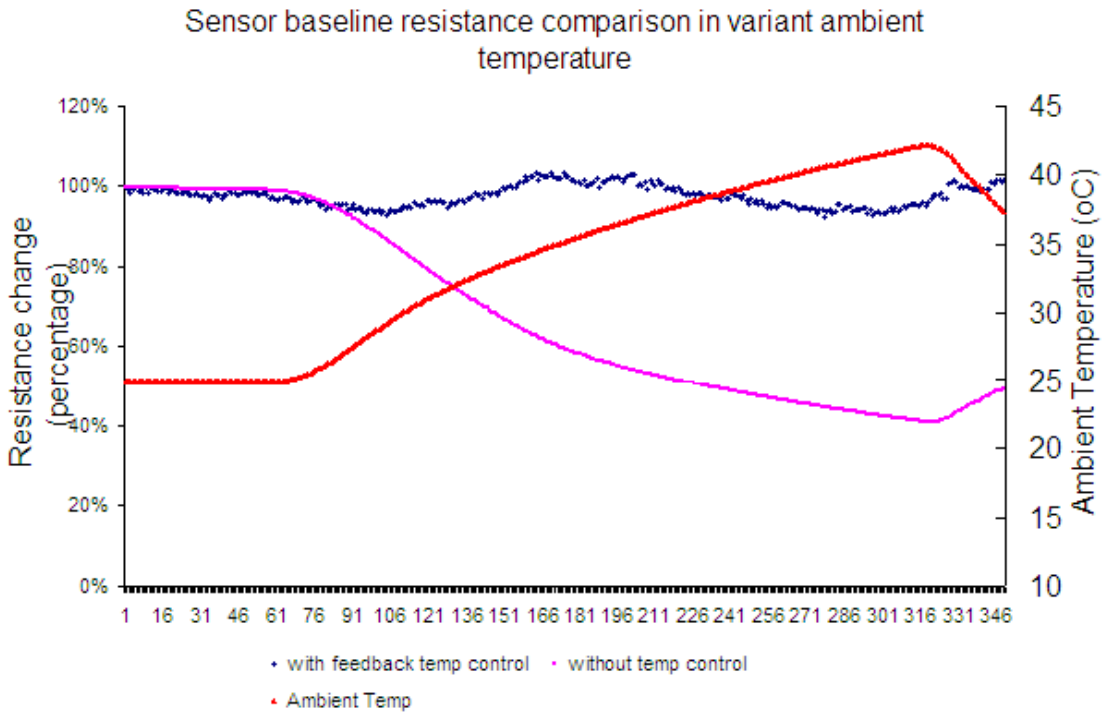


Figure 44 Gas resistance baseline change with ambient temperature change

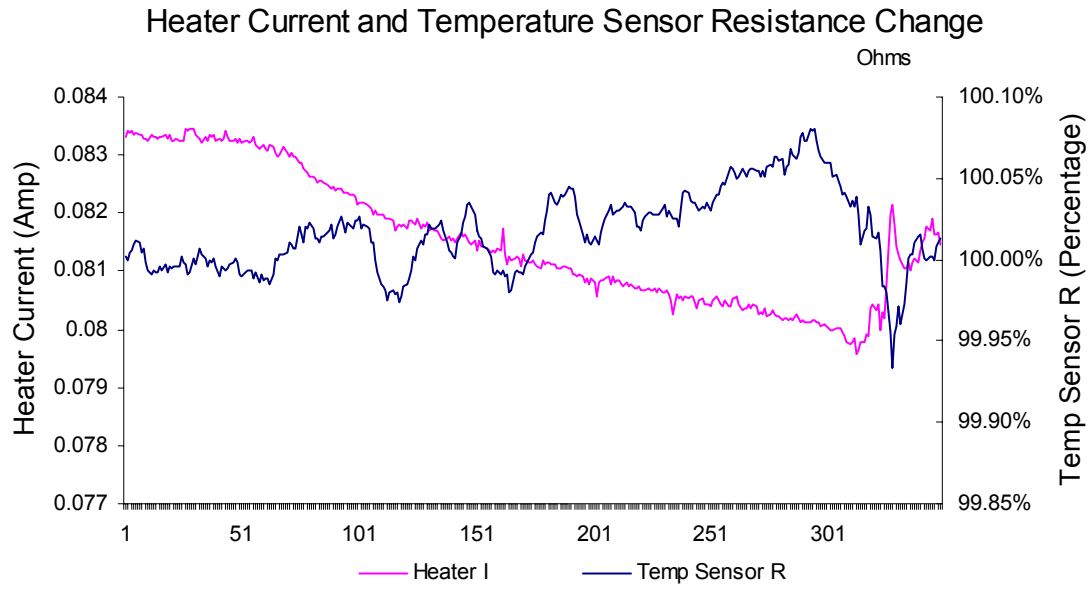


Figure 45 Built in Pt temp sensor change and Heater's current change

Figure 44 shows the comparison of sensors under same environmental conditions during the test. The resistance of sensor with the feedback temperature control only drifted within about 5 percent of its baseline resistance, while the resistance of the sensor without the temperature control dropped more than 40 percent (Figure 44). The actual meaning of the 40 percent resistance change means that larger false signals will be predicted.

Figure 45 shows the relationship of temperature sensor's resistance versus the heaters' current. The heater's current decreases as the temperature's resistance increase (higher temperature). This indicates that with a decreased heater current when ambient temperature increases, the power applied on the sensor device decreased to compensate the environmental temperature change. The current percentage change in Figure 44 is within 5%, while the heater current range is within 4 mA. A quick response can be seen in Figure 45, when a quick temperature change induced resistance change, a quick current increment is provide automatically to compensate the temperature change.

## 4.6 Discussions and Future Improvement

From the result shown in Figure 44, we conclude that this temperature feedback control circuit has significantly improved the sensor's stability. However, there are still some small fluctuations due to ambient temperature changes. The causes of such a fluctuation may be explained as in the followings.

Based on the feedback temperature control circuit working principle, i.e. the feedback information is provided by the temperature sensor's output, whose fluctuation will be magnified to compensate the fluctuation caused by the ambient temperature. Therefore, there is always a small difference between the controlled temperature and the predefined temperature. The "temperature difference" will result in a "different heater current" for the compensation purpose. The larger the gain and the transconductance are, the smaller difference between the controlled temperature and the desired temperature becomes.

Large thermal mass causes delay in feedback control performance. Current sensor design has a large thermal mass (using bulk ceramic wafer substrate) comparing to the micro Pt heater used. By taking further advantage of MEMS technique, the future design will be using smaller and thinner substrate. Much lower thermal mass is also preferred to achieve lower power consumption and fast response.

In the current design, the area of sensing film is larger than the heated area. From the thermal analysis point of view, there is a thermal distribution peak which appears inside of heater area. Therefore, during the temperature feedback control process, the actual temperature distribution may be not uniform, since temperature at heater's area is higher than that of outside sensor electrode. This problem will be solved in the future design, in which, the heater area will be larger than the gas sensing film's area.

# 5 GAS TEST RESULTS AND DISCUSSION

## 5.1 Environmental Influences on SMO Sensors' Performance

As is mentioned in the previous chapter, temperature has a big influence on SMO gas sensor's performance. Besides that, there are several other environmental factors that will affect a SMO gas sensor, e.g. humidity, light and oxygen partial pressure etc. These factors will be firstly discussed in this chapter.

### *5.1.1 Humidity*

Relative humidity is major concern among SMO sensor's reliability-related requirements. It is well known that water vapor strongly influences semiconductor metal oxide gas sensors' conductance *G* both in air and in partial pressure of a reducing gas in air. [151,152, 153]

#### 5.1.1.1 Influence on gas sensor baseline resistance

Madou et al. brought up that the lower the humidity, in general, the greater the dependency to relative humidity[154] . When humidified air is introduced in a background of synthetic air, resistance decreases very fast and afterwards increases slowly, reaching a

final value very close to the resistance value in dry synthetic air. These dynamic responses have been already described for $SnO_2$, $In_2O_3$, ZnO and $WO_3$[155, 156, 157, 158]. The decrease is attributed to the dissociatively reaction of water with lattice oxygen, which leads to the formation of oxygen vacancies and so to a resistance decrease. The following slow resistance increase could be due to the recombination of the OH ions with the lattice oxygen vacancies previously formed. Our test results (Figure 46) on two SMO sensors (home made UCF $SnO_2$ sensor and commercial Bacharach $WO_3$ sensor of Scott Instrument) also show these trends: decrease of baseline resistance of gas sensor when R. H. increases. In range of R. H. lower than 30%, the curve is steeper; while in range of R. H. larger than 30%, the curve is more moderate.

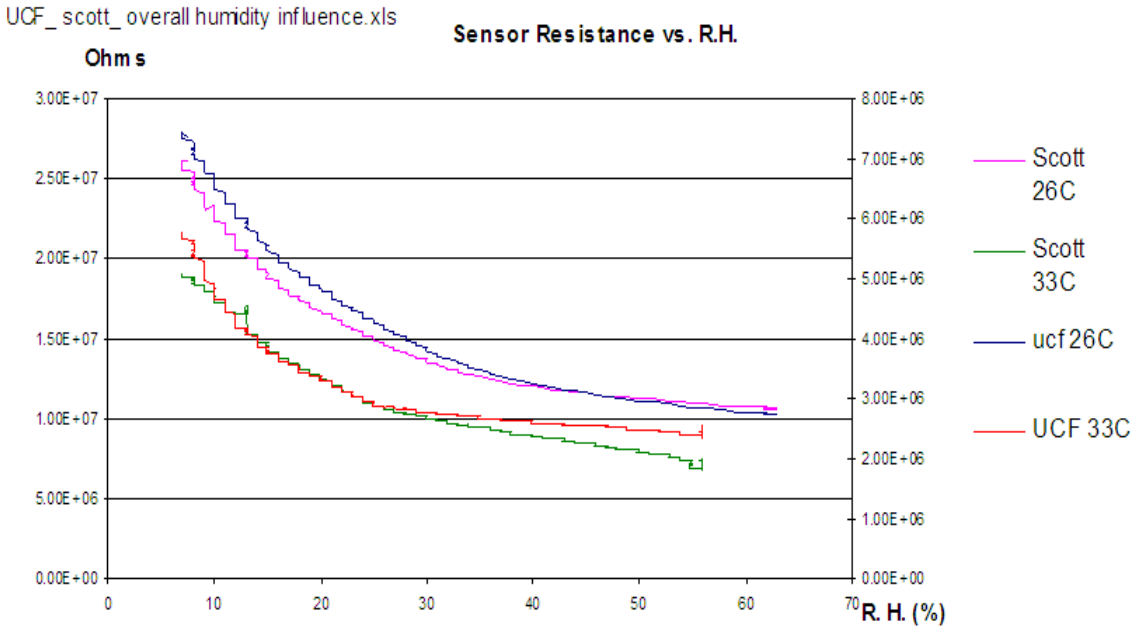


Figure 46 R. H. effects on gas sensor baseline resistance

This phenomenon can be described as a sequence of dissociation and reduction processes. A hydrogenation reaction of absorbed water can involve proton from a water molecule. A proton from a water molecule (strong Bronsted acid) is more easily available than the tightly-bound proton form an OH group (weak Bronsted acid). [159] Therefore, process described in equation (21) happens, and the oxygen vacancy on the right hand side has to move towards the bulk in order to become effective as a donor.

$$H_2O + Sn + O \rightarrow 2(OH - Sn) + V_o \qquad (21)$$

5.1.1.2 Influence on gas sensor sensitivity

Yannopoulos[160] suggested that the sensitivity changes with humidity, when the sample is used as a CO sensor, is due to the water/gas reaction, leading to a $CO/H_2$ ratio in the gas that depends on the water vapor pressure. Both oxygen ion and hydroxyl group attached to unsaturated tin sites donate electron to $SnO_2$ by reaction with a reducing gas. However, hydroxyl groups are blocked by water molecules at low temperature and high humidity because of water condensation on the sensor surface. He claimed that the device is relatively insensitive to humidity in the humidity range from 20% RH to 100% RH, although sensor resistance decreases above 70% RH because of instability from water condensation. A model for the interaction between CO and $SnO_2$ surface, which takes into account the role of water vapor, is brought by N. Bârsan et al[161]. They refer interaction of water vapor with the $SnO_2$ surface as a generating process of chemisorption sites for oxygen and conclude that the reacting chemisorbed species of oxygen is doubly ionized oxygen atoms and that their interaction with reducing gases is enhanced by the

presence of water vapor. $H_2S$ tests at different relative humidity level are conducted regarding to this issue, and the results are discussed in the later section of this chapter.

### *5.1.2 Light influence*

This discovery and explanation of this phenomenon of a SMO gas sensor are the first time to be brought up based on the author's knowledge. Our preliminary test result shows that, when fluorescent lamp in lab was turned off, gas sensor resistance increased gradually until certain level, and when lamp was turned on again, sensor resistance decreased and returned to previous level. This test has been repeated for several times, and got ~ 20% resistance change every time.

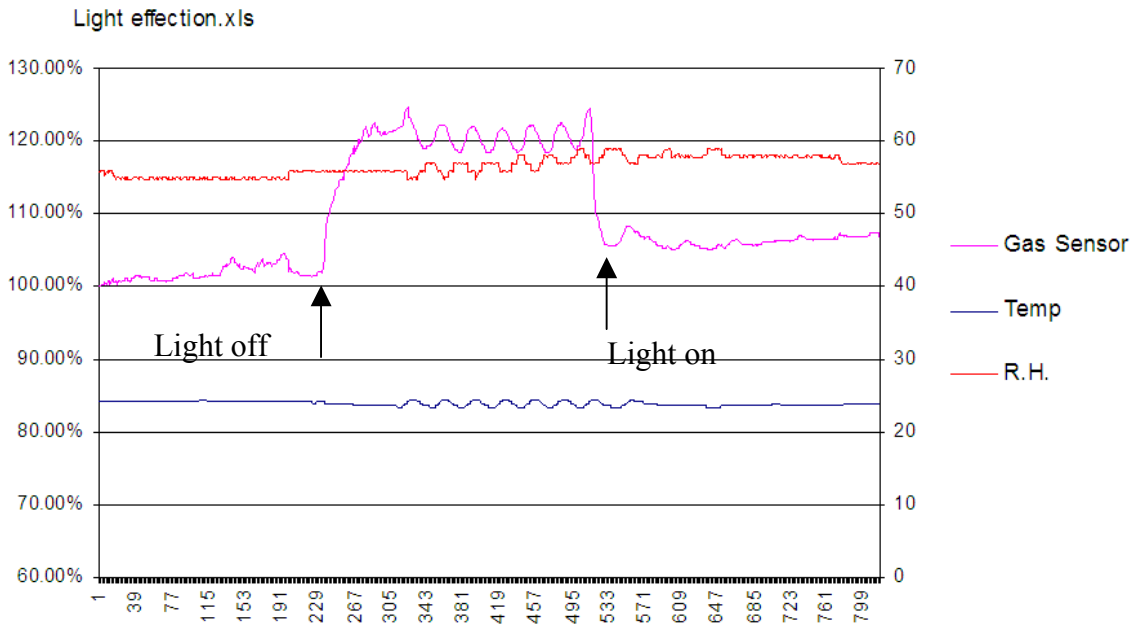


Figure 47 Light influence on SMO gas sensor

Figure 47 shows the test result of light influence on $SnO_2$/Ag sensor, sensor resistance when light is on and off. Ambient temperature and R.H. are also monitored to exclude their effects on gas sensor.

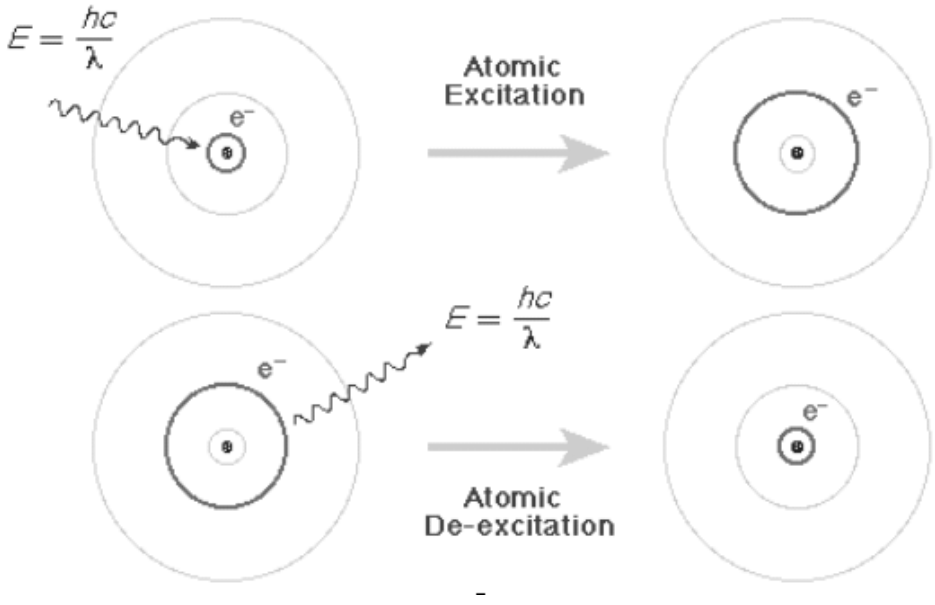


Figure 48 Excitation by absorption of light and de-excitation by emission of light

This photoemission phenomenon can be explained using atom Bohr Model, i.e. the neutrons and protons occupy a dense central region called the nucleus, and the electrons orbit the nucleus. Electrons can make transitions between the orbits allowed by quantum mechanics by absorbing or emitting exactly the energy difference between the orbits. Figure 48 shows an atomic excitation cause by absorption of a photon and an atomic de-excitation caused by emission of a photon. In each case the wavelength of the emitted or absorbed light is exactly such that the photon carries the energy difference

between the two orbits, i.e. $hc/\lambda$, where $h$ *is* Planck constant, $c$ *is* the speed of light and $\lambda$ is the wavelength of the light. Thus, an atom can absorb or emit only certain discrete wavelengths (or equivalently, frequencies or energies). Therefore, according to this theory, tin oxide absorbs certain wavelength of light and the acquired energy stimulates electron movement and increase conductivity.

### *5.1.3 Oxygen partial pressure effect*

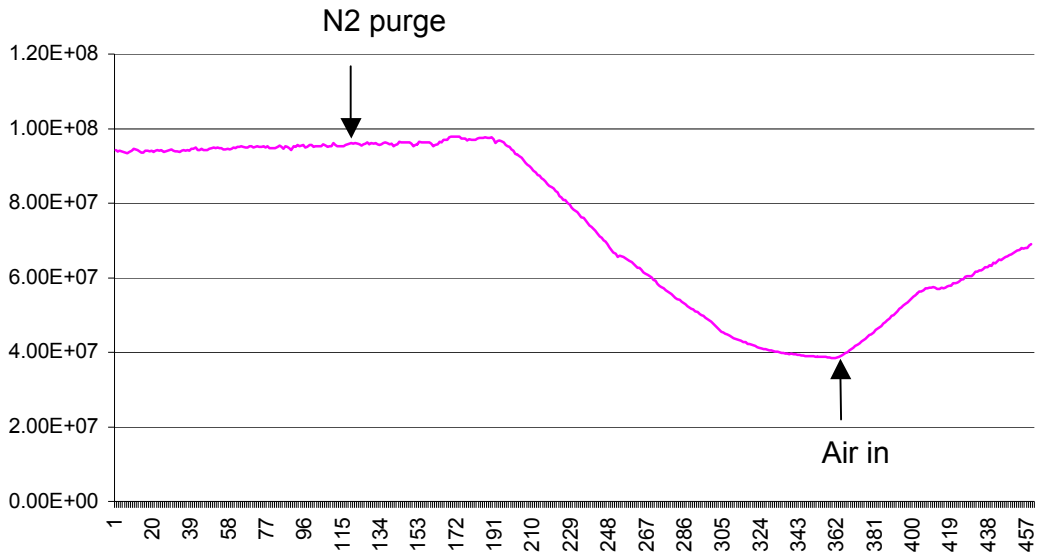


Figure 49 Oxygen partial pressure effect

According to the SMO gas sensor working principle model[8], oxygen partial pressure is also a factor that may influence the gas sensor resistance, an experiment was performed to verify this, refer to Figure 49. After sensor is stabilized, large flow rate

(2L/min) of nitrogen flew into test chamber (4L), the result showed that gas sensor resistance didn't change right after $N_2$ was introduced, however, after around 2 minutes, resistance began to drop. Therefore, we can conclude that the amount that are absorbed onto tin oxide surface are very small, it will reach saturated state even in very small oxygen concentration environment. However, when oxygen partial pressure was lower than that level, further oxygen concentration changes would affect SMO sensor's resistance.

## 5.2 Concentration Calculation (Tank Filling Formula)

Certain concentration of target gas is prepared by filling pre-mixed known-concentration gas into test chamber. Therefore, the gas concentration C is function of volume of gas chamber and time. The time to reach a given concentration in a tank is given by equation 22:

$$t = \frac{V_o}{V_1} \ln \frac{C_1 - C_o}{C_1 - C} \tag{22}$$

where, $V_o$ is the volume of the tank

$C_o$ is the initial concentration of the gas in the tank

$V_1$ is the gas flow in the tank

$C_1$ is the concentration of the flowing gas.

C is the concentration in a moment t of time

t is the time in which this concentration is reached.

## 5.3 Gas Sensor Sensitivity

There are two mostly used sensitivity definitions:

$$\text{Sensitivity } S_1 = (R_0 - R_1)/R_0 \times 100\% \quad (23)$$

$$\text{Sensitivity } S_2 = (R_0 - R_1)/R_1 \quad (24)$$

Where $R_0$ is baseline resistance of gas sensing thin film in air, and $R_1$ represents resistance in gas environment.

## 5.4 Hydrogen Sensitivity Characterization

$SnO_2$ sensor doped with Pt has good sensitivity to Hydrogen, test results of fabricated $SnO_2$+Pt thin film gas sensor cell and $SnO_2$+Pt+Ag thin film gas sensor cell in a series of hydrogen concentration environment and different working temperatures are presented in Figure 50~ Figure 55. The comparison of gas sensing performance for these two sensors is summarized in Table 9. The results shows that $SnO_2$/Pt/5%Ag film has achieved better sensing results than $SnO_2$+Pt sensing film. We can observe that $SnO_2$/Pt/5%Ag film has less baseline drift, better sensibility, faster response time and quicker recovery time comparing to $SnO_2$/Pt film. The doped Ag can improve the sensing ability of $SnO_2$ thin film to hydrogen. It also indicates that for both thin film gas sensors, a fairly good sensitivity can be achieved at 100°C. Better results have been achieved at higher temperatures such as 200°C and 250°C. Another characterization of both sensors is the fast response time (2s ~ 6s) and quick recovery time (10s~40s) to hydrogen compared to other reported $H_2$ gas sensors, e.g. 15~30s response time and 20~60s

recovery time of single layer carbon film to $10^3$ppm $H_2$[162], several second's response time of ZnO+Pd thin film to $H_2$[163], 14~21s' response time and up to 35min's recovery time of nano sized mesoporous powder $SnO_2$ paste to $H_2$, and other reported longer response time and recovery time. [107,164,165,166,167,168]

Table 9 Comparison of sensitivity $S_1$ to Hydrogen at 100°C

| | 2000ppm | 4000ppm | 8000ppm | Res. T. | Rec. T. |
|---|---|---|---|---|---|
| $SnO_2$ / Pt | 14% | 18% | 23% | ~ 6 s | ~ 40 s |
| $SnO_2$ /5% Ag/Pt | 17% | 23% | 30% | ~ 5 s | ~ 40 s |

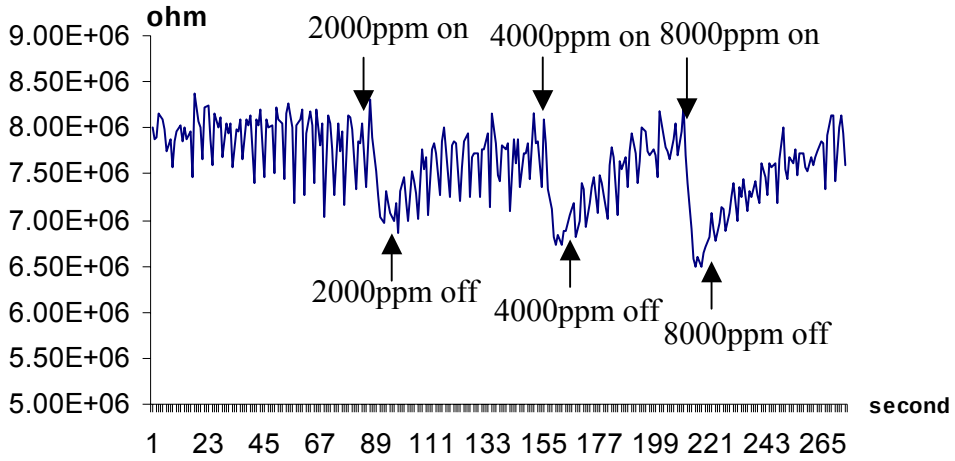


Figure 50 Response of $SnO_2$ +sputtered Pt to $H_2$ at 100°C

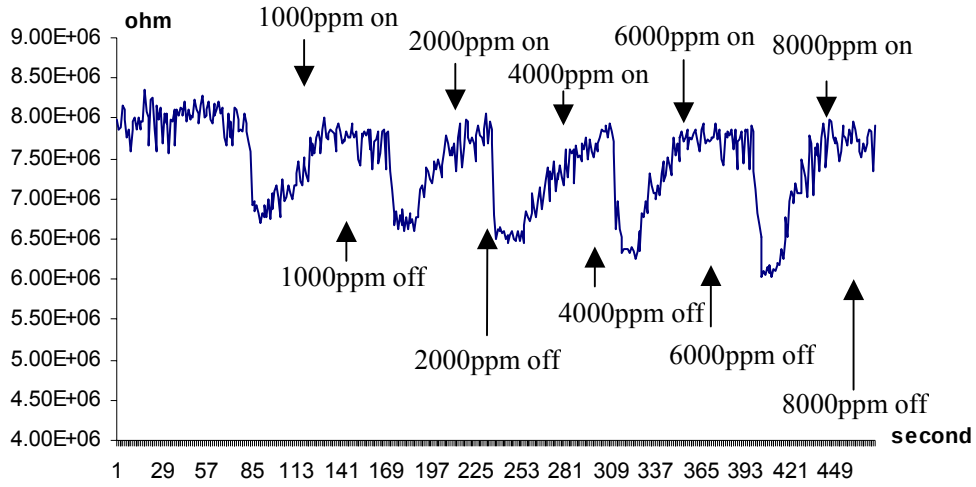


Figure 51 Response of $SnO_2$ +5% Ag+sputtered Pt to $H_2$ at 100°C

Table 10 Comparison of sensitivity $S_1$ to Hydrogen at 200°C

| | 1000ppm | 2000ppm | 4000ppm | 6000ppm | 8000ppm | Res. T. | Rec. T. |
|---|---|---|---|---|---|---|---|
| $SnO_2$ / Pt | 15% | 20% | 24% | 31% | 40% | ~ 4 s | ~ 20 s |
| $SnO_2$ /5% Ag/Pt | 24% | 38% | 53% | 70% | 90% | ~ 4 s | ~ 15 s |

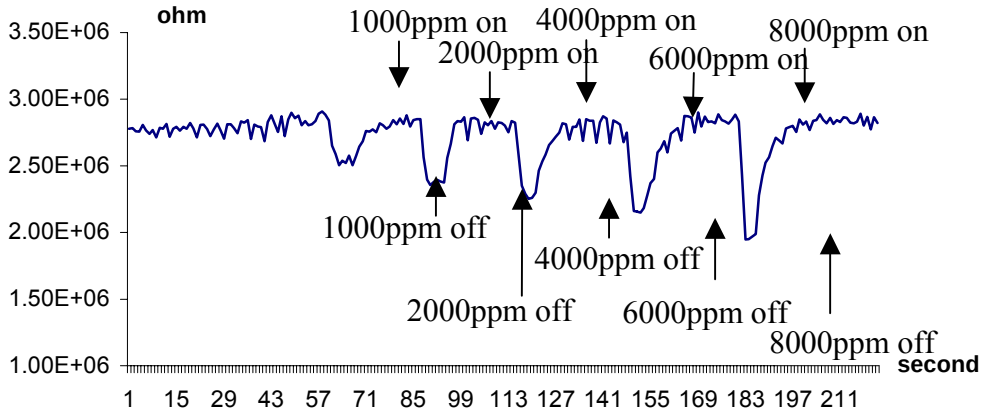


Figure 52 Response of $SnO_2$ + sputtered Pt to $H_2$ at 200°C

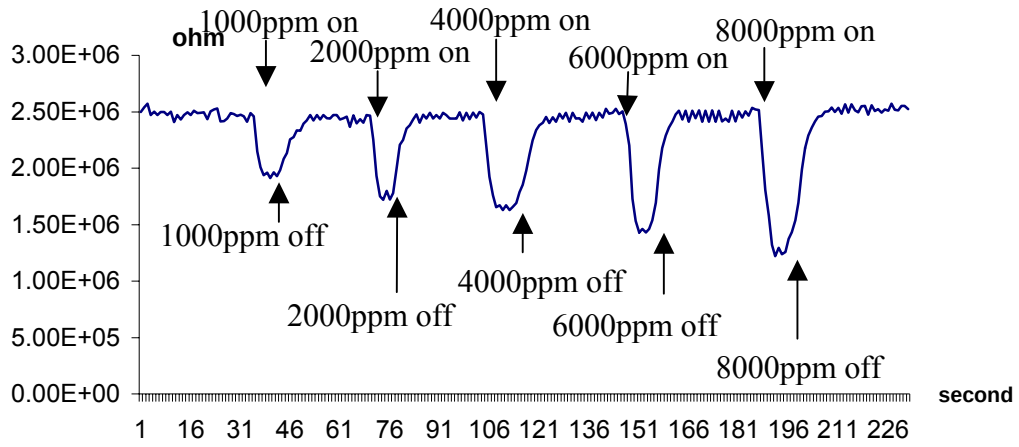


Figure 53 Response of $SnO_2$ +5% Ag+sputtered Pt to $H_2$ at 200°C

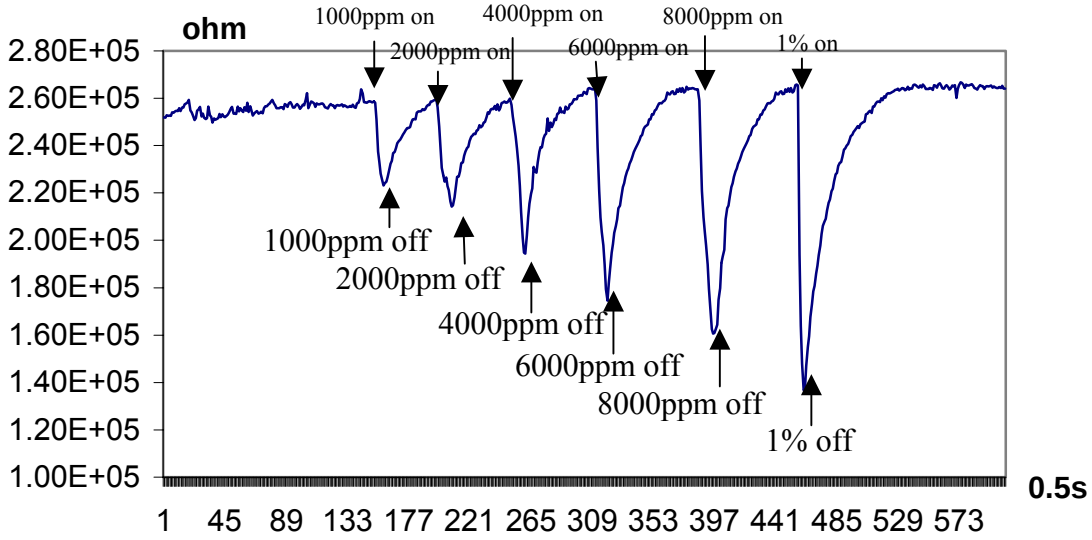


Figure 54 Response of $SnO_2$ +sputtered Pt $H_2$ 250°C

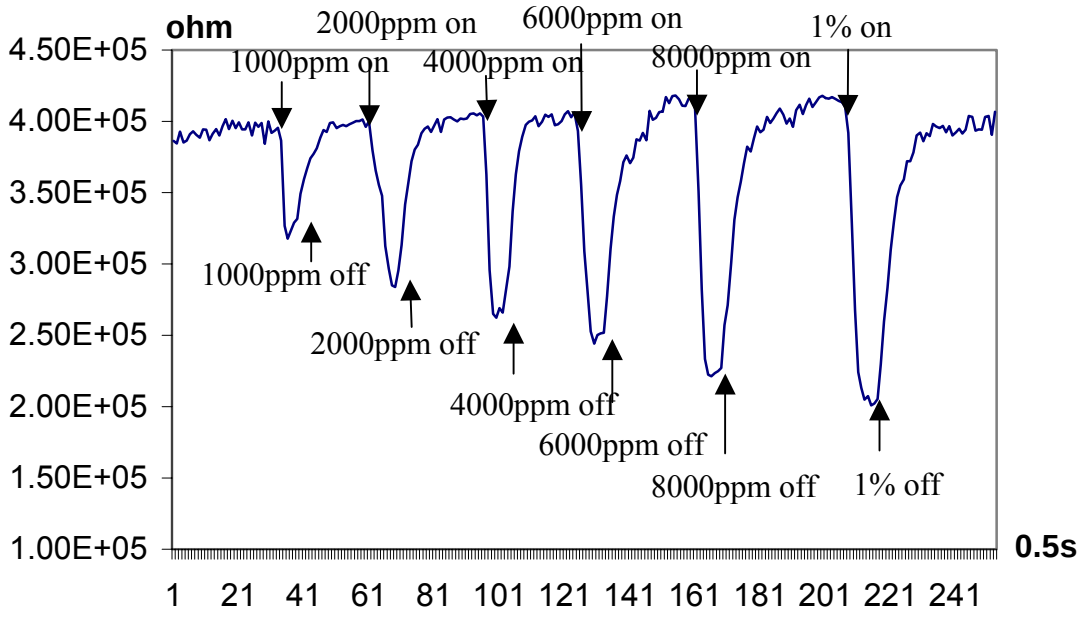


Figure 55 Response of $SnO_2$ +5% Ag+ sputtered Pt to $H_2$ at 250°C

Table 11 Comparison of sensitivity $S_1$ to Hydrogen at 250°C

| | 1000ppm | 2000ppm | 4000ppm | 6000ppm | 8000ppm | 1% | Res. T. | Rec. T. |
|---|---|---|---|---|---|---|---|---|
| $SnO_2$ / Pt | 18% | 22% | 30% | 44% | 63% | 85% | ~2s | ~ 20s |
| $SnO_2$ /5% Ag/Pt | 30% | 41% | 53% | 64% | 79% | 100% | ~2s | ~10s |

## 5.5 Hydrocarbon Sensitivity Characterization

Sensors with pure $SnO_2$ film have been tested to in hydrocarbons. The test results to acetone and ethanol at 300°C are shown in Figure 56 and Figure 57. A comparison of sensitivity, response time and recovery time is shown in Table 12. According to this table, we can conclude that even though there are no catalysts being doped, the fabricated gas

sensor with pure $SnO_2$ nano films have good sensitivity, quick response time and recovery time to Acetone and Ethanol.

Table 12 Comparison sensitivity $S_1$to Acetone and Ethanol at 300°C

| | 1000ppm | 2000ppm | 4000ppm | 6000ppm | 8000ppm | Res. T. | Rec. T. |
|---|---|---|---|---|---|---|---|
| Acetone | 8% | 13% | 18% | 26% | 36% | 4s | 14 s |
| Ethanol | 21% | 27% | 40% | 55% | 70% | 3 s | 9 s |

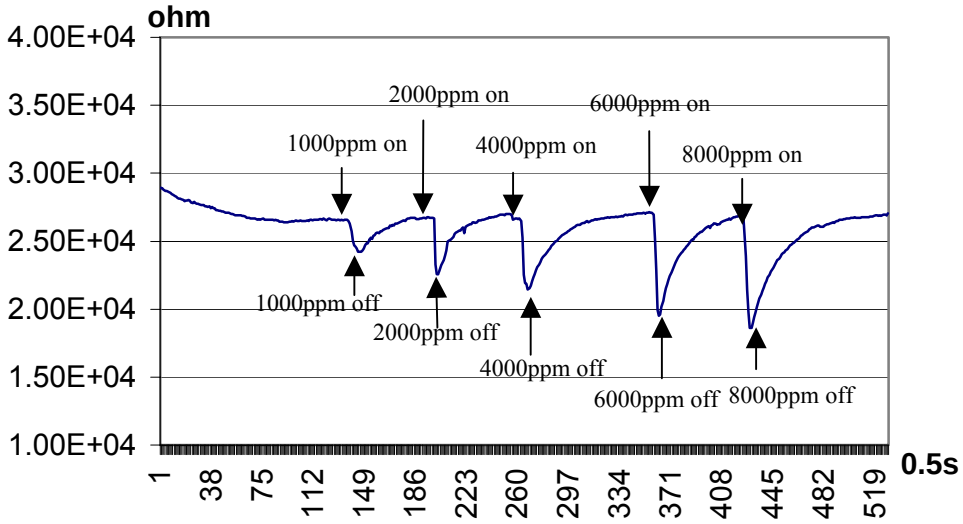


Figure 56 Response of pure SnO2 to acetone at 300°C

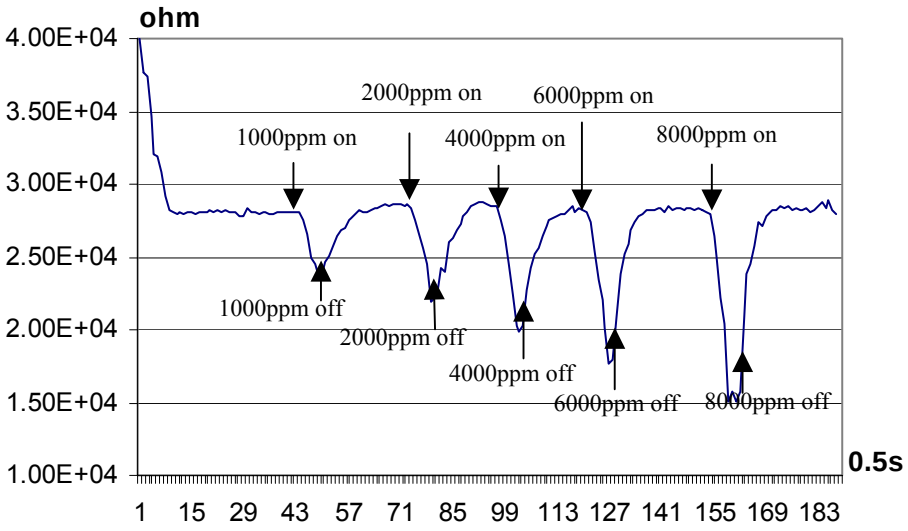


Figure 57 Response of pure $SnO_2$ to Ethanol at 300°C

## 5.6 Hydrogen Sulfide Sensitivity Characterization

Two fabricated $SnO_2$ sensor doped with Ag are tested in Hydrogen Sulfide. UCF1 is a big device with quartz substrate, and UCF2 is small device with ceramic substrate. For better understanding our sensor's performance, we have included some commercial sensors include Figaro (Tin oxide) $H_2S$ sensor TGS825, MICS 4512 (SMO) CO&$NO_2$ sensor and Bacharach (SMO) $H_2S$ sensor for comparison.

### *5.6.1 Verification of gas sensitivity theoretical formula*

As is mentioned in the previous section, the relationship between SMO sensor resistance and gas concentration can be expressed as Equation 1[9]. By using natural log on both sides, equation 1 can be changed to form of: $\ln(Rs) = -\alpha \ln(A) - \alpha \ln(C)$, which

shows that ln(Rs) and ln($^{o}$C) has linear relationship with slope of $\alpha$ and intersection of $\alpha$ln(A). We use simple experiment to verify this formula: 100ppm $H_2S$ was prepared and flew into test chamber in certain rate, resulting gas concentration at certain time can be calculated using Equation 18 [88]. We plotted ln(Rs) and ln($^{o}$C) and the relationship is shown in Figure 58. It is clear that, there is a linear relationship between ln(Rs) and ln($^{o}$C) in the range that ln($^{o}$C) is between 1.64 and 3.51 ( i. e. gas concentration between 5.1ppm and 33.4ppm). Explanation of the non-linear portion is: below 5ppm, non-linear could be caused by slow response time of sensor at low concentration condition, beyond 35 ppm, non-linear could be caused by saturation of sensor at higher concentrations. However, this is only the author's conjecture; further experiments should be conducted to prove. In spite of some non-linear portion, we still conclude that the relationship between SMO gas sensor resistance and gas concentration can be described by equation 1.

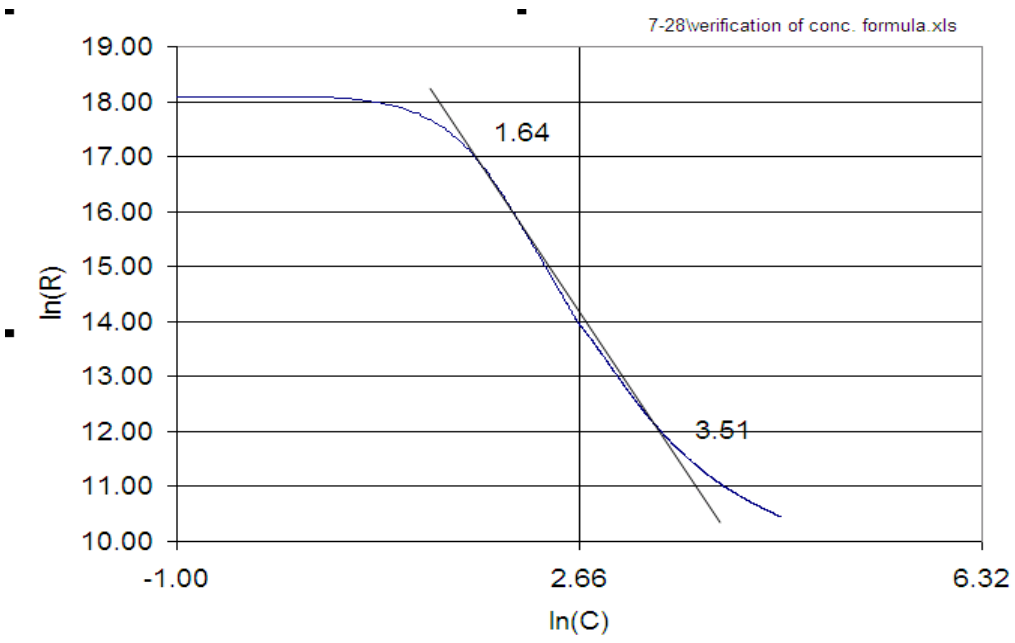


Figure 58 100ppm $H_2S$ experiment to verify theoretical formula

*5.6.2 Test of staircase concentration of $H_2S$*

A staircase concentration test was conducted for $H_2S$ testing. The procedure is: increase the concentration from lowest level to highest level, at each level, keep exposing to $H_2S$ gas for half an hour before increasing to the next concentration level. UCF1 sensor is working at 64°C and UCF2 sensor is work at 79°C. Figure 59 shows the four sensors response in a staircase concentration test. We pick up the UCF2 sensor to show more characterization details in Figure 60. The purpose of using log scale and reverse of R is to better differentiate gas concentrations (especially in high concentration range).

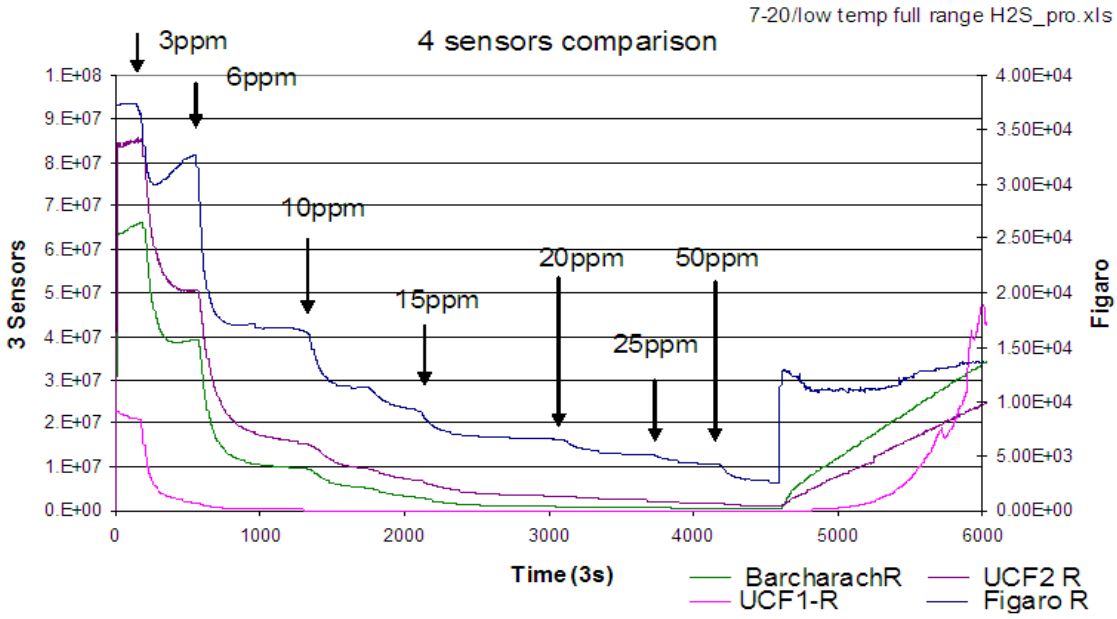


Figure 59 Staircase concentration $H_2S$ test result

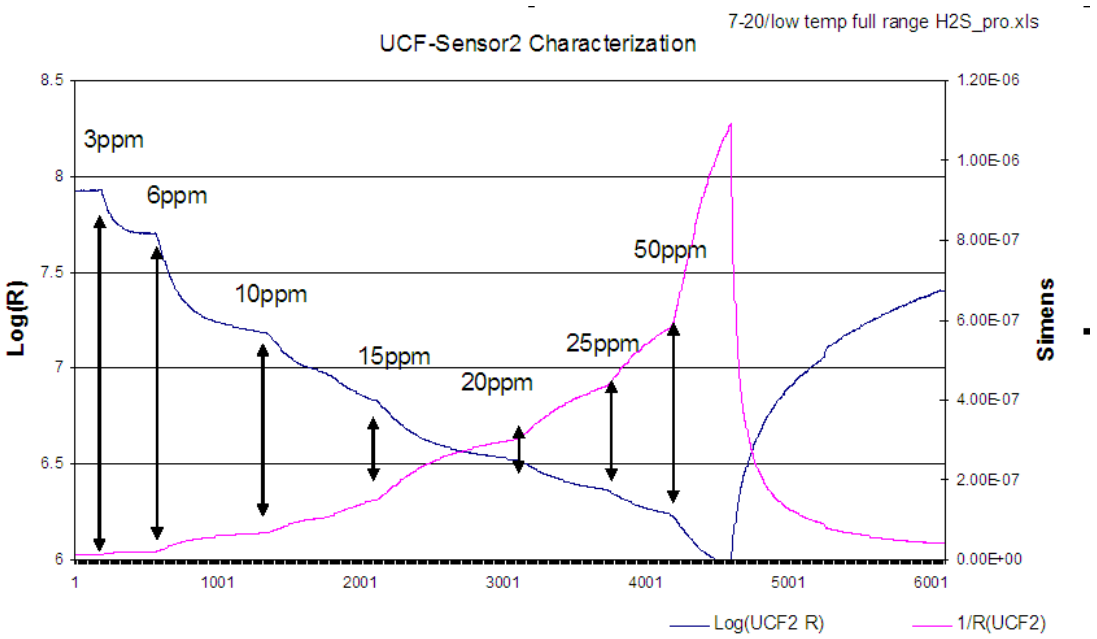


Figure 60 Characterization of UCF2 sensor

Table 13 Sensitivity summary of staircase concentration test

| | **3ppm** | | **6ppm** | | **10ppm** | | **15ppm** | |
|---|---|---|---|---|---|---|---|---|
| | $S_1$ (%) | $S_2$ | $S_1$ (%) | $S_2$ | $S_1$ (%) | $S_2$ | $S_1$ (%) | $S_2$ |
| Figaro | 19% | 0.14 | 54% | 1.28 | 75% | 3.09 | 82% | 4.7 |
| Bacharach | 40% | 0.86 | 85% | 5.91 | 95% | 23.2 | 98% | 83 |
| UCF-1 | 90% | 9.5 | 99% | 117 | 99% | 242 | 99% | 372 |
| UCF-2 | 40% | 0.86 | 82% | 4.67 | 92% | 12.7 | 96% | 24.6 |
| | **20ppm** | | **25ppm** | | **50ppm** | | | |
| | $S_1$ (%) | $S_2$ | $S_1$ (%) | $S_2$ | $S_1$ (%) | $S_2$ | | |
| Figaro | 82% | 6.22 | 82% | 7.78 | 82% | 13.3 | | |
| Bacharach | 99% | 108 | 99% | 137 | 99% | 204 | | |
| UCF-1 | 99% | 437 | 99% | 508 | 99% | 640 | | |
| UCF-2 | 97% | 35.8 | 98% | 52.1 | 99% | 91.2 | | |

Table 13 shows a summary of sensitivities of four gas sensors at different $H_2S$ concentrations. It is clear our fabricated sensor UCF1 sensor has the best sensitivities over other three sensors, and UCF2 and Bacharach sensor has comparable sensitivities. Since both UCF sensors have very good sensitivity to higher concentration of $H_2S$, therefore, sensitivity definition of $S_2$ is better than $S_1$ for differentiation.

### *5.6.3 Repeat test with different $H_2S$ concentration*

Repeat test is necessary to examine gas sensor's repeatable performance, for example, whether or not the baseline resistance could recover to its original value after being exposed to targeting gas. Figure 61 shows repeat test of UCF1 sensor and Figaro sensor at different concentrations of $H_2S$. It is obvious that baseline resistance can recover its original value after some time between tests.

### *5.6.4 Relative humidity influence on $H_2S$ sensor's sensitivity*

Tests were conducted on two SMO sensors, UCF $SnO_2$ sensor and Bacharach $WO_3$ sensor, to a full range of $H_2S$ concentration (1ppm~25ppm) in different R. H. (7%~98%). Figure 62- Figure 64 show the gas sensors responses at different $H_2S$ concentrations. Table 14 summarized test results of Figure 62- Figure 64. Figure 65 plots data of Table 14 to show trend of R. H. effect on $H_2S$ sensitivity.

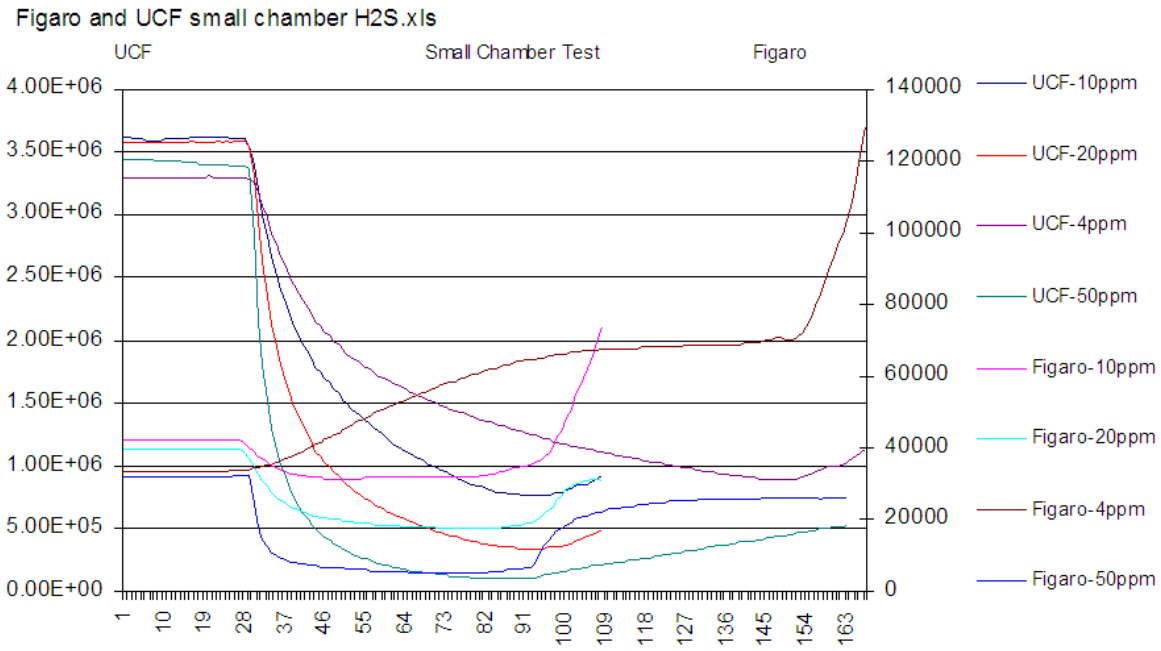


Figure 61 Repeat Test

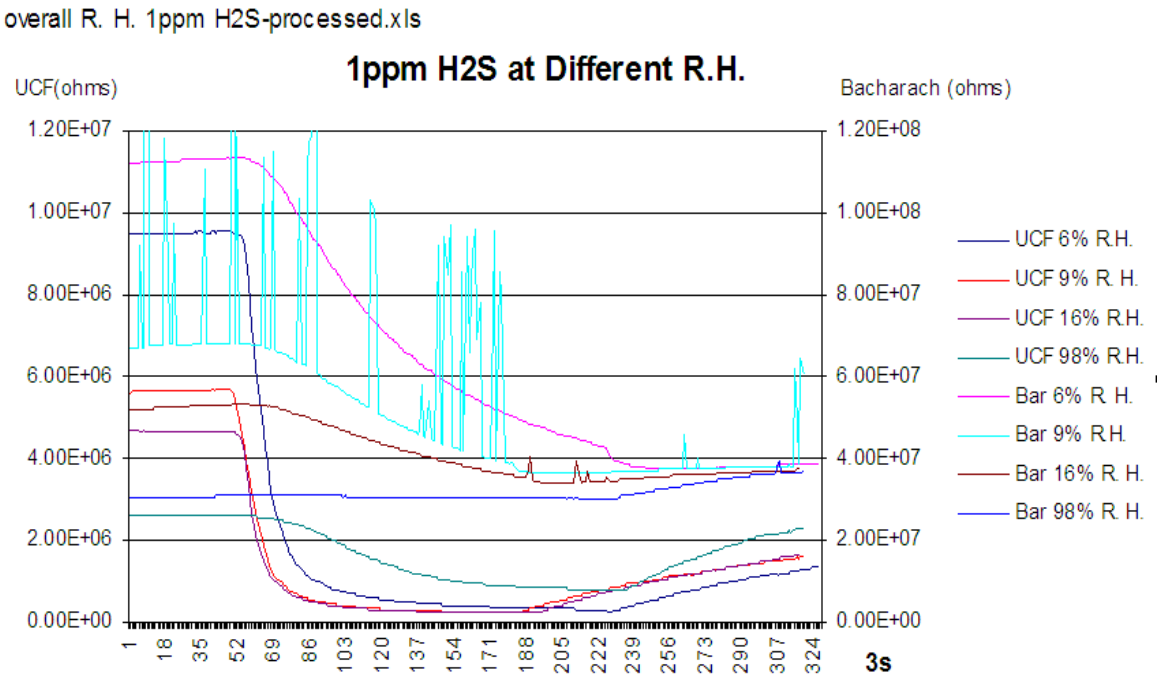


Figure 62 1ppm $H_2S$ test at different R. H.

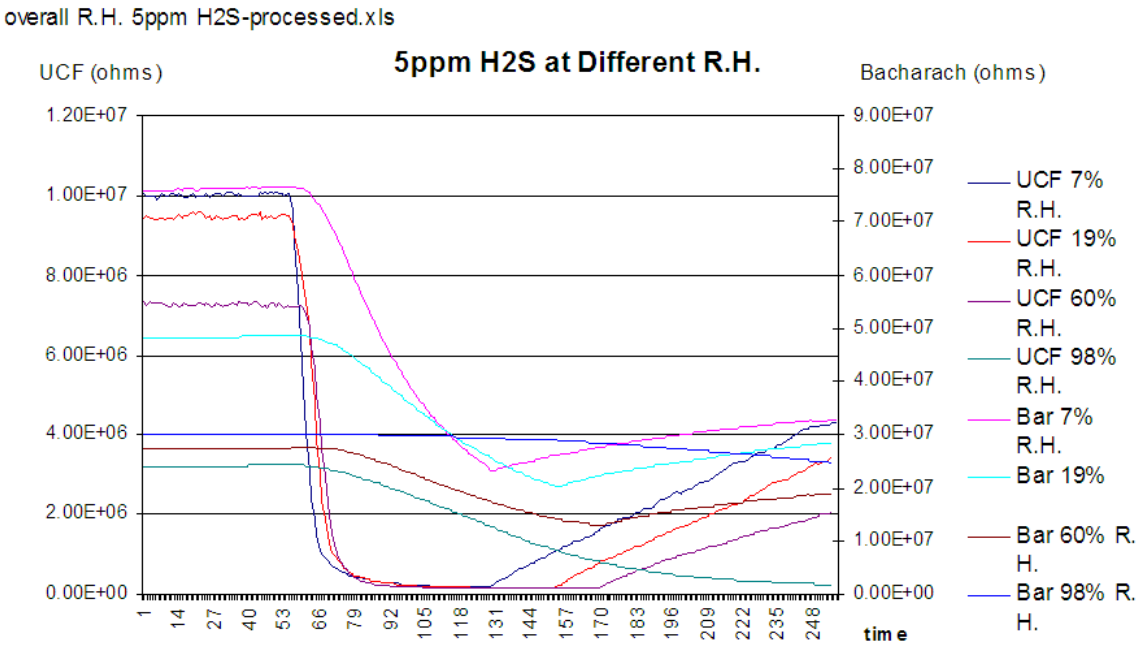


Figure 63 5ppm $H_2S$ test at different R. H.

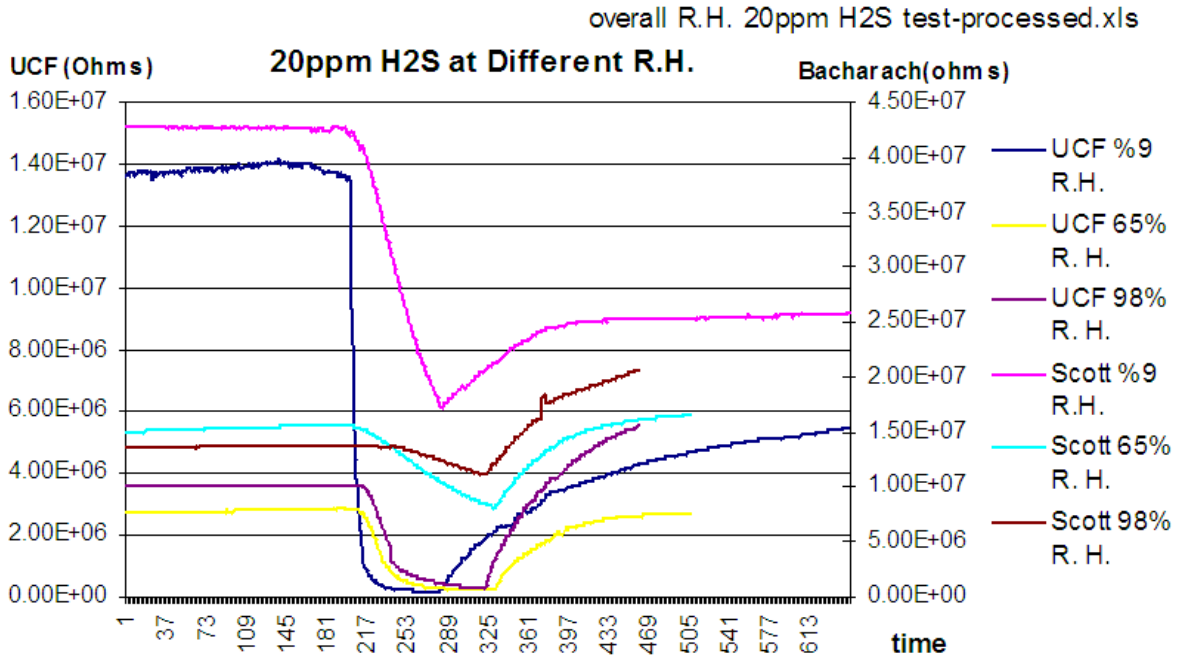


Figure 64 20ppm $H_2S$ test at different R. H.

Table 14 Summary of R. H. influence test (UCF sensor with quartz substrate)

| conc. (ppm) | R. H. | Baseline $R_0$ | $R_1$ | $S_1$ | $S_2$ |
|---|---|---|---|---|---|
| | | | | | |
| 1 | 6% | 9.5 | 0.31 | 96.74 | 29.65 |
| 1 | 9% | 5.68 | 0.248 | 95.63 | 21.9 |
| 1 | 16% | 4.65 | 0.23 | 95.05 | 19.22 |
| 1 | 70% | 6.37 | 1.36 | 78.65 | 3.68 |
| | | | | | |
| 5 | 9% | 10.05 | 0.17 | 98.31 | 58.12 |
| 5 | 19% | 9.4 | 0.14 | 98.51 | 66.14 |
| 5 | 60% | 7.2 | 0.114 | 98.42 | 62.16 |
| 5 | 98% | 3.2 | 0.144 | 95.5 | 21.22 |
| | | | | | |
| 10 | 9% | 9.9 | 0.079 | 99.2 | 124.32 |
| 10 | 56% | 7.2 | 0.095 | 98.68 | 74.79 |
| 10 | 98% | 6.3 | 0.168 | 97.33 | 36.5 |
| | | | | | |
| 1 | 70% | 6.37 | 1.36 | 78.65 | 3.68 |
| 2 | 60% | 6.17 | 0.446 | 92.77 | 12.83 |
| 5 | 48% | 6.95 | 0.12 | 98.27 | 56.92 |
| 10 | 51% | 6.1 | 0.092 | 98.49 | 65.3 |
| 20 | 60% | 6.8 | 0.079 | 98.84 | 85.08 |
| 25 | 57% | 6.7 | 0.06 | 99.1 | 110.67 |
| | | | | | |
| 2 | 98% | 5.18 | 0.846 | 83.67 | 5.12 |
| 5 | 98% | 5.1 | 0.492 | 90.35 | 9.37 |
| 10 | 98% | 5.1 | 0.098 | 98.08 | 51.04 |
| 20 | 98% | 6.1 | 0.086 | 98.59 | 69.93 |
| 25 | 98% | 5 | 0.067 | 98.66 | 73.63 |
| | | | | | |
| 2 | 9% | 9.6 | 0.17 | 98.23 | 55.47 |
| 5 | 9% | 11 | 0.12 | 98.91 | 90.67 |
| 10 | 9% | 9.9 | 0.079 | 99.2 | 124.32 |

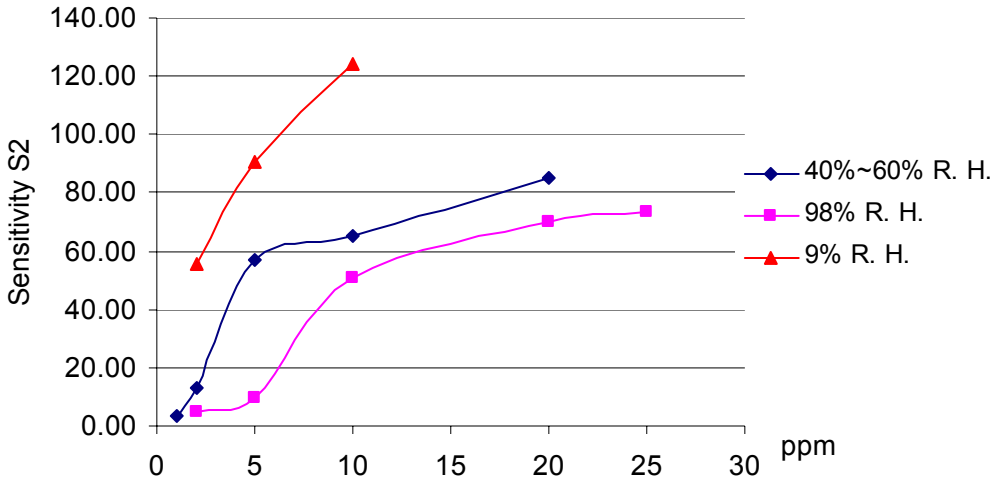


Figure 65 R.H. effects on sensor's sensitivity on $H_2S$

The test results show that sensitivity of our $SnO_2$ $H_2S$ sensor is greatly affected by relative humidity, even at level higher than 30%. It is obvious that sensor sensitivity decreases as relative humidity increases when the background is $H_2S$ in air. We can conclude that water is probably competing with $H_2S$ molecules and preventing oxygen ions from reacting with $H_2S$. When air is reintroduced again, previous sensor resistance value is recovered; the slow recovery time is due to a slow desorption of adsorbed $H_2S$ molecules.

## 5.7 Carbon Monoxide Sensitivity Characterization

Pt and Pd have been widely reported as catalyst to $SnO_2$ sensor's to enhance its sensitivity and selectivity to CO (Table 3).

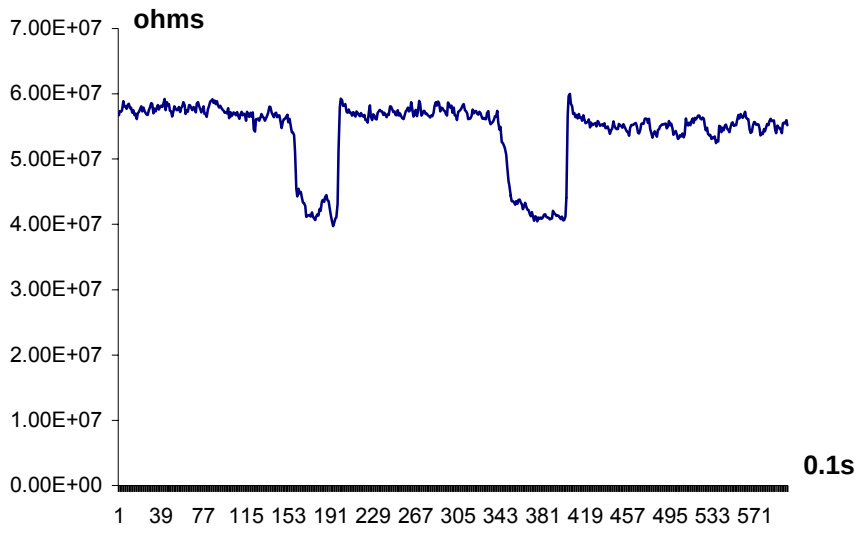


Figure 66 Pure $SnO_2$ film's response to 100ppm CO at 200C

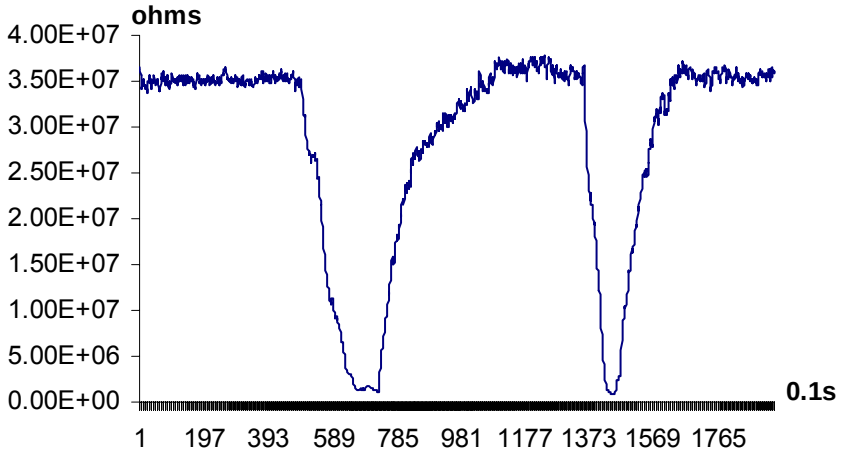


Figure 67 $SnO_2$+Ag+Pt film's response to 100ppm CO at 200$^oC$

Figure 66 shows the response of pure $SnO_2$ sensor to 100ppm CO at working temperature of 200 $^oC$, in comparison with response of $SnO_2$ sensor doped with both Ag and Pt at the same temperature, which is shown in Figure 67.

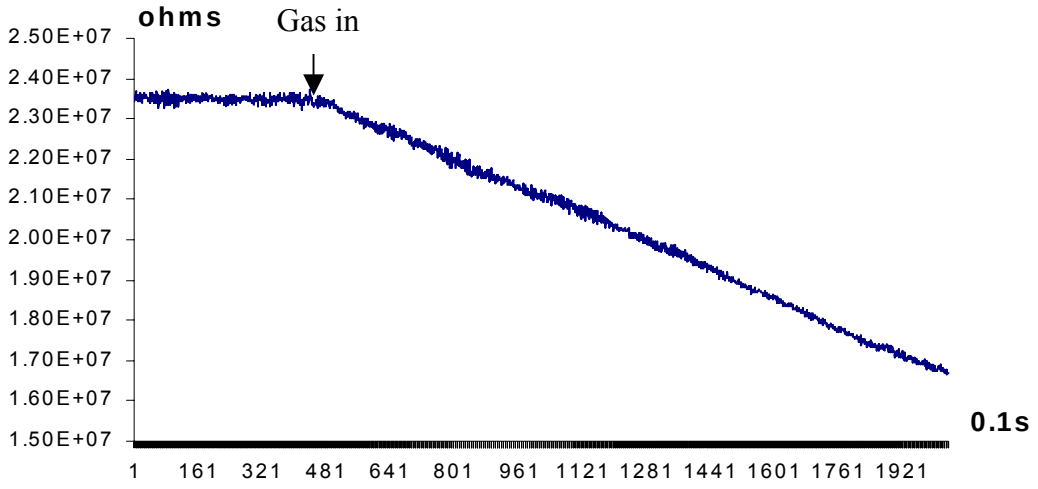


Figure 68 $SnO_2$+Ag+Pt film's response to 0.1 ppm CO at 200$^{o}$C

The comparison indicates that sensitivity to CO has been improved a lot by adding Pt as catalyst. This CO sensor also has a fast response time (1s) and quick recovery time (3s) to 100ppm CO, as well as very good sensitivity (can detect as low as 0.1ppm CO, refer to Figure 68 for details ).

## 5.8 General Discussions

The general gas sensing characteristics (independent of gas) of the sol-gel derived nanocrystalline $SnO_2$ thin film sensor including particle size, thin film topology, film thickness, and the operating temperatures etc are discussed here. Besides, environmental influences to SMO sensor are also discussed.

*5.8.1 Characteristics of the sol-gel derived $SnO_2$ thin film*

5.8.1.1 Particle size

The gas detection principle of semiconductor type gas sensor is based on variations of the depletion layer at the grain boundaries in presence of reducing or oxidation gases which lead to variation in the height of the energy barriers for free charge carriers (e.g. electrons in $SnO_2$) [169]. The enhanced sensitivity gas sensors with nanocrystalline $SnO_2$ thin film attributes to two aspects. First, as particle size decreases, the surface to volume ratio increases largely (reverse proportional to the particle size), which leads to better sensitivity. According to the model brought up by Xu et al., depending on the nanocrystalline size (D) relative to its space charge layer thickness (L), the transducer function is operated by a mechanism of grain-boundary control ($D>>2L$), neck control ($D>2L$) or grain control ($D\leq 2L$), respectively. The gas sensitivity of nanocrystalline $SnO_2$ thin film is enhanced only when the film resistance is controlled by the latter two mechanisms, especially by the grain control mechanism. For the $SnO_2$ thin film, the space-charge layer thickness has been calculated to be ~3 nm at 250 $^oC$ . As a result, the sensitivity increase steeply as D decreases and a maximum sensitivity can be achieved when the grain size is comparable with or less than 2L ($\approx$ 6 nm for $SnO_2$). The particle size of nanocrystalline $SnO_2$ used in this research is ~15nm, prepared by the sol gel process. This is one of the reasons that cause enhanced sensitivity.

5.8.1.2 Topology of thin film

The porous topology of gas sensing thin film has great impact on gas sensing behavior. In this study, block copolymer as a convenient group of structure-directing agents, has been applied during the sol preparations. The mesoporous tin oxide thin film fabricated using this sol gel process has large amount of porosity, which is another contribution to the enhanced sensitivity. Bai, N. S. et al.[170] attribute this phenomenon to an enhanced Knudsen diffusion coefficient ($D_k$). For straight round pores within the thin film, $D_k$ is given by,

$$D_k = 9700 \times r \times (T/M)^{1/2} \qquad (25)$$

Where, r is the pore radius, T the absolute temperature (K), and M the molecular weight of the gas for sensing. For a given film thickness, larger pore radius increases $D_k$, and hence would favor the improved gas concentration profile.

5.8.1.3 Thickness of thin film

The thickness of nanocrystalline $SnO_2$ thin film is also an important factor that greatly affects gas sensitivity. Unlike $TiO_2$, which is bulk conductance effect semiconductor, $SnO_2$ belongs to the surface conductance effect semiconductors. The interaction between a semiconductor surface and reducing gas (Hydrogen in Figure69) can be explained in terms of reaction of hydrogen molecules with the pre-adsorbed oxygen:

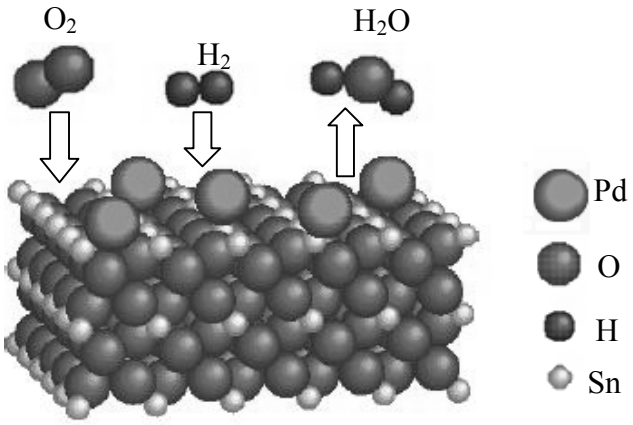


$$O_2^- + 2H_{2(g)} = 2H_2O_{(g)} + e^-$$

$$O^- + H_{2(g)} = H_2O_{(g)} + e^-$$

$$O^{2-} + H_{2(g)} = H_2O_{(g)} + 2e^-$$

Figure 69 Interaction between a $SnO_2$ surface and reducing gas

S. Shukla et al [171] proposed that gas sensitivity of nanocrystalline $SnO_2$ thin film increases as decreasing the film thickness. However, below a critical film thickness of ~110 nm, the gas sensitivity decreases with further decrease in the film thickness. Very compact films exhibit lower surface areas and reduced Knudsen diffusion coefficient. As a result, they offer reduced number of active sites for the oxidation reactions with the reducing gases, and hence, would reduce the gas sensitivity with decreasing film thickness below this critical thickness range. In this investigation, the nanocrystalline $SnO_2$ film thickness is about 100~150 nm obtained via sol-gel spinning coating process under strictly controlled processing conditions.

5.8.1.4 Working temperature

From the results analysis, we also find that, as working temperature elevate, the resistance of gas sensing film decrease until reaches a stable level. Regarding to gas sensitivity, the $SnO_2$ has best sensitivity to hydrogen at 300 $^oC$. This phenomenon can be explained: when operating temperature is below 300$^oC$ (from room temperature to 300$^oC$), the desorption of water and adsorption of the oxygen-ions ($O_2^-$ and $O^-$ ions) dominates, which decreases the conduction electron density within the film, which favors the higher gas sensitivity[172], On the other hand, in the higher operating temperature range above 350 $^oC$, the desorption of the oxygen-ions dominates. This thermally excites the electrons from the trap levels to the conduction band, which increases the conduction electron density, thus reducing the gas sensitivity [170,173].

*5.8.2 Schemes to deal with environmental influences*

For a practical application, a gas sensor should meet many requirements which are imposed by the purposes of application, withstanding various challenges encountered from environment during sensor's operation. The main requirements are two folds. The first ones include sensing performance-related such as sensitivity, selectivity and rate of response, and the second ones are reliability-related like drift, stability and interfering gases. Compared to performance-related requirements, the reliability-related ones are more critical and challenge for SMO sensor. Environmental influence such as ambient temperature and relative humidity has long been remained as influencing factors to SMO sensor's instability and false alarm problem. The reason for that is, in most cases sensor

output contains a constant term as the reference (air base) which is irrelevant to the target gas. As was discussed in the previous part of this chapter [89], $R_0$ in sensitivity formula is assumed constant, however, when baseline resistance tends to shift following the change of environment conditions or drift with time, reliability of gas sensing is undermined. Therefore, it is very important to quantitatively understand semiconductor gas sensors' shift of air base resistance influenced by environmental conditions and calibrate or adjust gas sensor in different application fields. Techniques that cope with ambient temperature fluctuations have been discussed in pervious chapter, here we will focus on R.H. issue.

Many techniques were proposed to deal with this R.H. influence problem. A first method to decrease the influence of the relative humidity is to incorporate additives into the tin oxide. However, with this method, it is impossible to eliminate the influence of water to an acceptable level . Another method is to use an array of sensors and to convert the response of this array by means of mathematical algorithms, in order to obtain a response that is insensitive to water vapor[174]. P. V. Geloven et al [175] use a method of switching a single tin oxide gas sensor between two well-defined temperatures to decrease the sensitivity to water vapor to an acceptable level. G. Huyberechts et al [176] proposed to use a combination of two metal oxide based sensors and a humidity sensor to form a micro system with a trained artificial neural network. They got a quantitative output for both methane and carbon monoxide irrespective their mutual presence and the presence of varying humidity levels. Other method includes compensation of the moisture effect by referring to a compensation device which is exactly the same as the

sensing device except for a sheet of glass placed on top in order to make the device sensitive to moisture only. [177]

PureChoice's latest five-sensor nose monitors use a module from Senserion (Zurich, Switzerland) that has a temperature sensor and humidity sensor and provides a calibrated, digital two-wire output. Other sensors monitor carbon dioxide, carbon monoxide (CO), and VOCs. The five-sensor version, has patented software and hardware to help maintain precise temperature of the carbon monoxide and VOC sensors to minimize sensor drift. The output from the temperature/humidity sensor can also be used to correct the other sensors for temperature and humidity effects. A microprocessor and custom memory chip corrects and calibrates the output of each sensor, and reformats the sensor outputs for digital communication.

# 6 CARBON NANOTUBE/SMO GAS SENSORS

## 6.1 SWNT Introduction

Since the discovery of carbon nanotube (CNT) in 1991 (Iijima), many researchers explored its possibilities of working as sensors. A single-walled carbon nanotube (SWNT) is a nano scale hollow tube formed by a cylindrical shell of single atomic layer of carbon atoms. Nanotubes have diameter of a few nm and length up to 100mm so that they form extremely thin hollow wires. Experimental and theoretical studies have found that these nano-meter sized CNTs have novel electronic properties, metallic or semiconducting, depending on their chiralities. Since the nanotube electronic property is a strong function of its atomic structure, mechanical deformations or chemical doping can induce strong changes in conductance. Such changes can be easily detected by electron current signals, and these properties make CNTs extremely small sensors sensitive to their chemical and mechanical environments. Most studies on carbon nanotube for gas detection application have been focused on chemically gas sensing properties of nanotube. The conductivity of the nanotube changes when chemicals in the surrounding environment bond to the tube, chemical sensors based on individual or ensembles of single-wall nanotubes can detect chemicals such as nitride dioxide and ammonia[178]. Other reported CNT-based gas sensors can detect methane[179], oxygen[180] and carbon dioxide[18080]. However, they also found that

SWNT doesn't response well to some gases. For example, CO and SWNT show no binding indicating that a bare nanotube may not work as a CO sensor. Due to extremely high surface-to-volume ratio, efficient gas adsorption occurs on the surface of the carbon nanotube. The one-dimensional quantum wire nature makes its electronic properties very sensitive to the gas molecules adsorption.

The objective of this research work is to take advantage of both $SnO_2$ and SWNT and to improve $SnO_2$ gas sensing property in terms of sensitivity, response time and recovery time by using SWNT reinforcement. The function of "SWNT" can be summarized into two-fold. The first one is using structural SWNT to achieve permanent nano passes for gas sensing after sintering $SnO_2$. The second one is using SWNT to define the distance between gas accessing boundaries to be less than two time of depletion zone of $SnO_2$ (6nm).

## 6.2 Experimental

Nanostructured $SnO_2$ Sol was prepared using the same routine introduced in the previous chapter [31]. $SnO_2$ thin film was spin-coated followed by sintering process at 500$^{o}$C. Figure 72 shows an SEM micrograph of pure $SnO_2$ film (grain size is about 15nm).

Commercially available carbon nanotubes contain impurities like amorphous carbon; therefore, a purification process is needed before SWNT can be added to $SnO_2$ sol. The purification process start from the commercially acquired AP-Grade Nanotube, it

is boiled in mild NaOH solution (PH=10-12) for 72 hours followed by ultrasonic stir for 10 minutes, the solution is then centrifuged the black super-cant (amorphous carbon) will be decayed off. At last, wash by 50% HCl acid. Figure 70 and Figure 71 (adapted from Bo Li) show the SEM picture of SWNTs as received and after purification respectively. Purified SWNT is added as dopants into well prepared nanosized $SnO_2$ sol followed by 24 hours magnetic stirring and another 10 min ultrasonic cell disrupting, the dark color transparent solution containing SWNT suspension is acquired, typically the SWNT's diameter is approximately 1.4 nm.

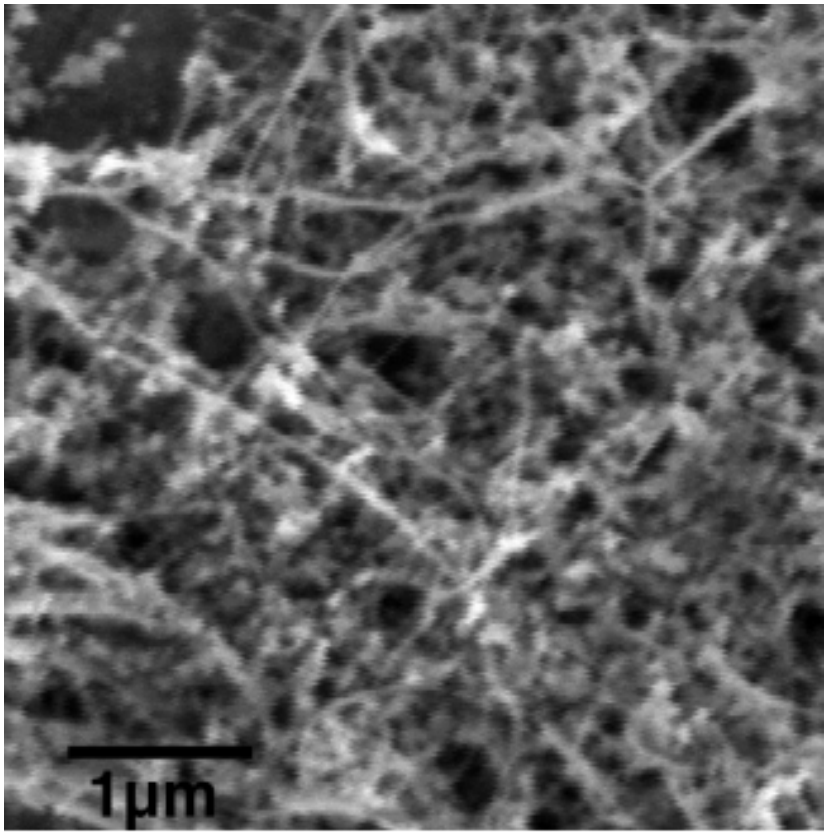


Figure 70 Carbon nano tubes as recived

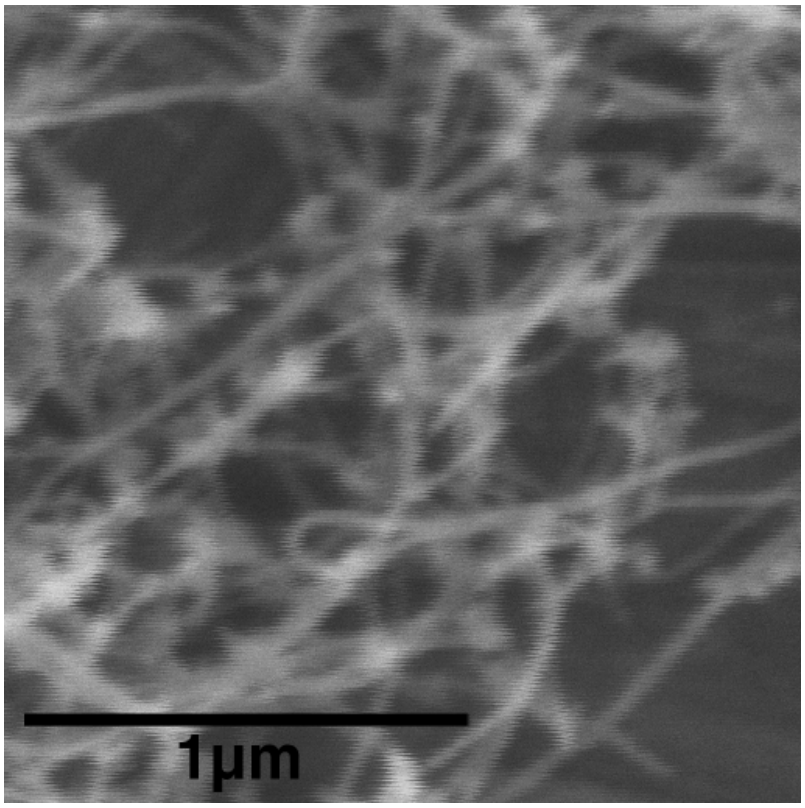


Figure 71 SEM picture of purified SWNTs

The viscosity of the sol was adjusted with addition of PVA (poly vinyl alcohol). After sintering at 500°C within argon environment for 2 hours, sol consisting of nano-sized $SnO_2$ and uniformly distributed SWNT was achieved, as is shown in SEM picture of Figure 73, compared to pure $SnO_2$ film (Figure 72). Figure 74 shows microscopic picture of fabricated SWNT/SMO gas sensor thin film.

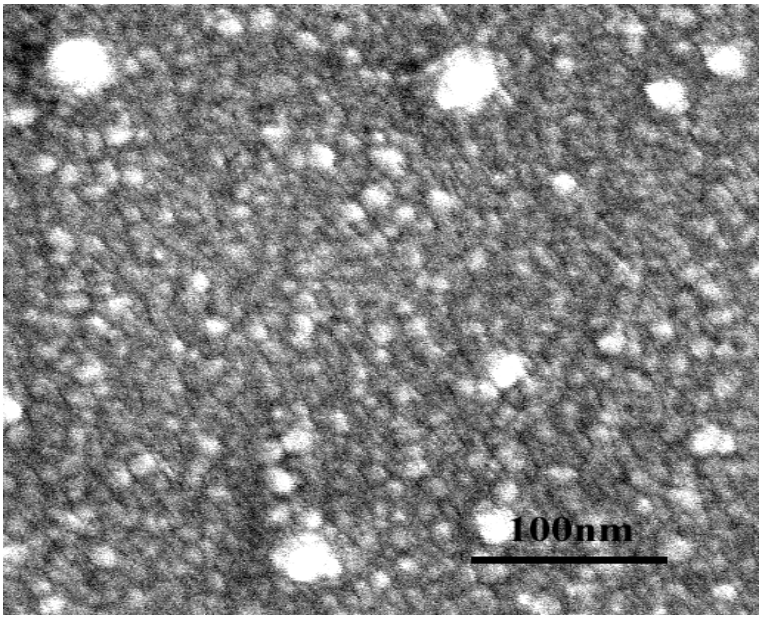


Figure 72 Pure $SnO_2$ particles in range of 15 nm

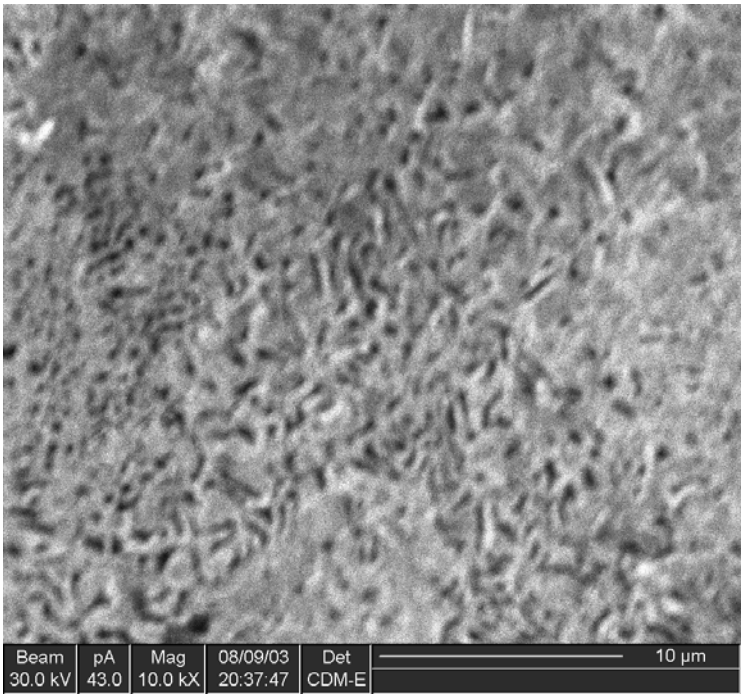


Figure 73 SWNT wrapped by nano sized $SnO_2$

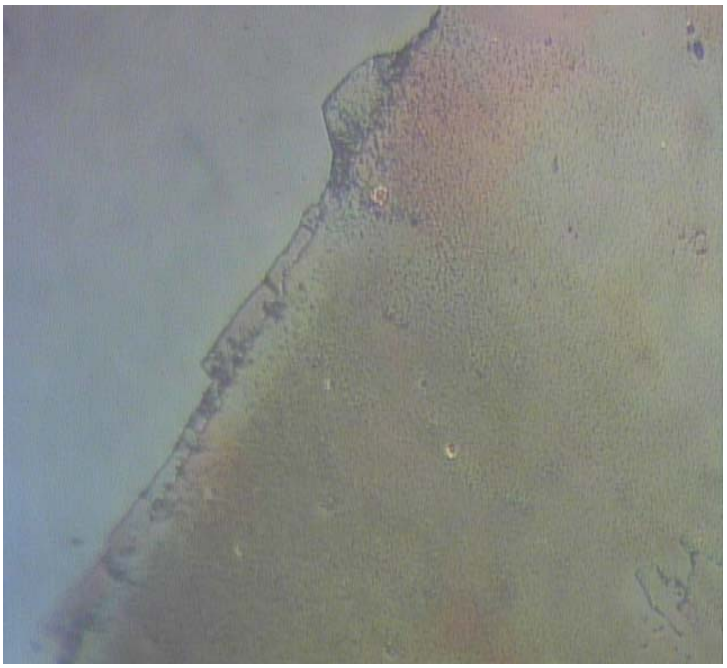

Figure 74 Nanotube/$SnO_2$ thin film under 500X microscope

## 6.3 Test Result and Discussion

Both pure nano $SnO_2$ and SWNT enhanced nano $SnO_2$ sensors working at different working temperatures were tested in 1500ppm hydrogen environment for comparison. Tested results are presented in Figure 75 and the comparison is summerized in Table 15. It is obvious that SWNT/$SnO_2$ composite sensor has much better gas-sensing properties than the pure $SnO_2$ sensor. The sensitivity is three times higher (Table 15) at various working temperatures. The SWNT/ $SnO_2$ sensor has a good sensitivity to Hydrogen at temperatures as low as 150°C, while the pure $SnO_2$ sensor doesn't. The undoped SWNT/$SnO_2$ sensor even has much better sensitivity than $SnO_2$ sensor doped with catalysts[181].

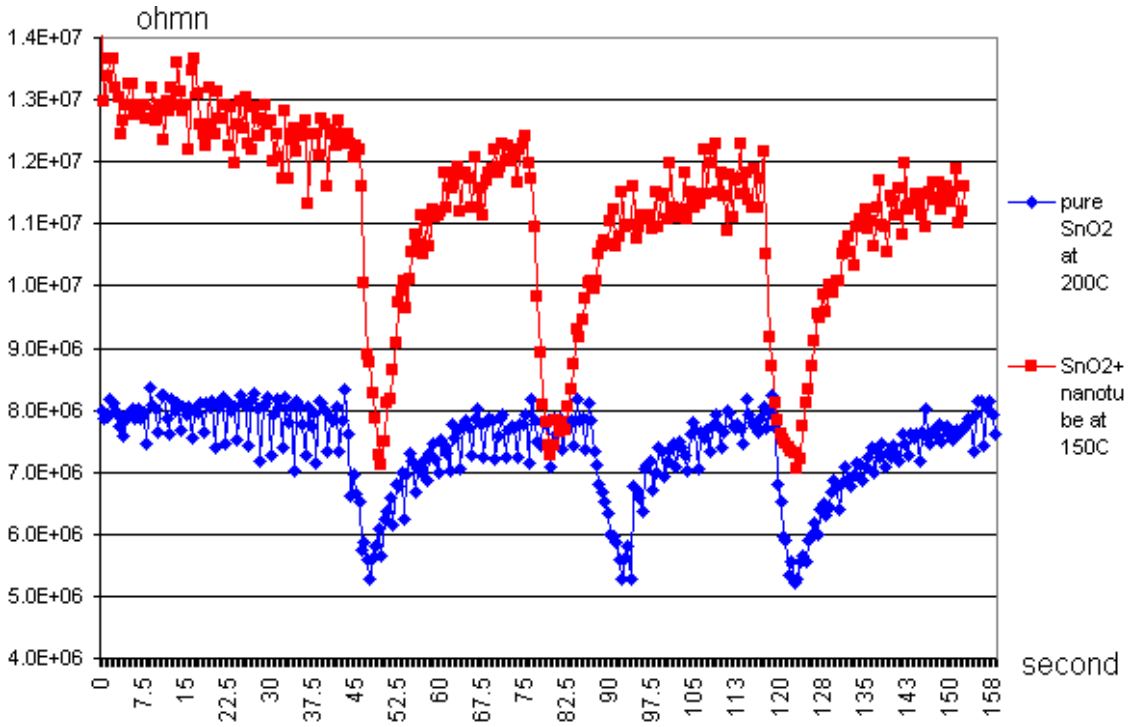


Figure 75 Comparison of various test results in 1500ppm hydrogen

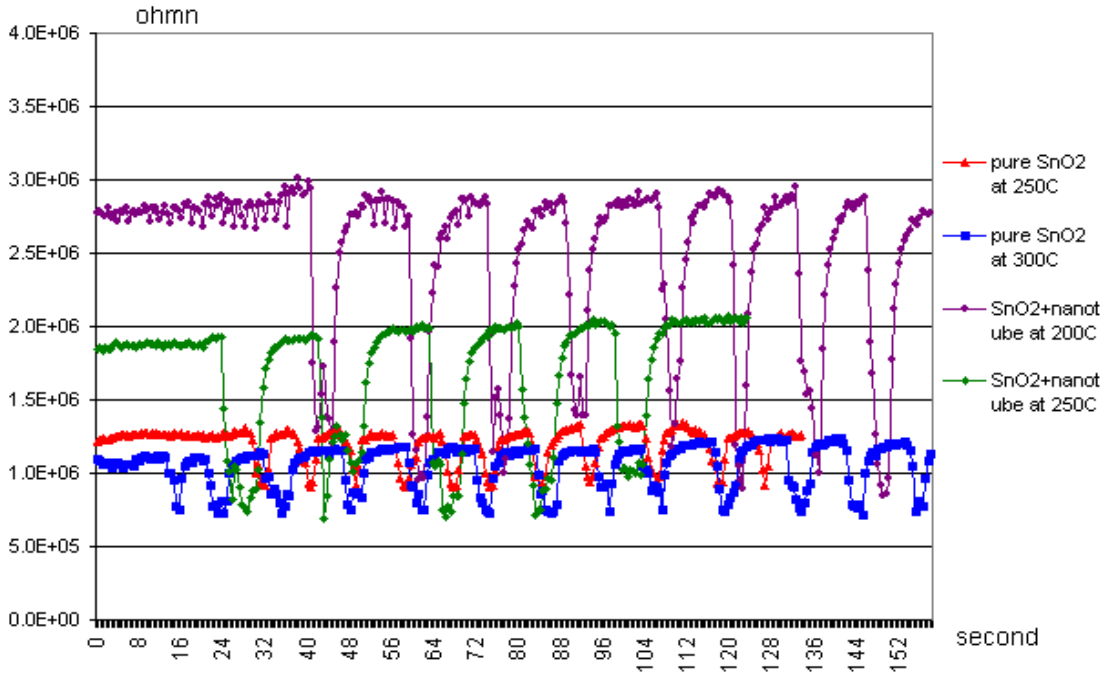


Figure 75 (cont.) Comparison of various test results in 1500ppm hydrogen

Table 15 Comparison of pure $SnO_2$ sensor and SWNT/ $SnO_2$ sensor at different working temperature

| | Sensitivity | Response time | Recovery time |
|---|---|---|---|
| Pure $SnO_2$ at 150°C | N/A | N/A | N/A |
| $SnO_2$/SWNT at 150°C | ~50% | 5~7s | 15~18s |
| Pure $SnO_2$ at 200°C | ~39% | 5~7s | 25~30s |
| $SnO_2$/SWNT at 200°C | ~115% | 3~5s | 3~5s |
| Pure $SnO_2$ at 250°C | ~40% | 3~5s | 6~8s |
| $SnO_2$/SWNT at 250°C | ~147% | 2~3s | 4~5s |
| Pure $SnO_2$ at 300°C | ~56% | 3~5s | 5~7s |

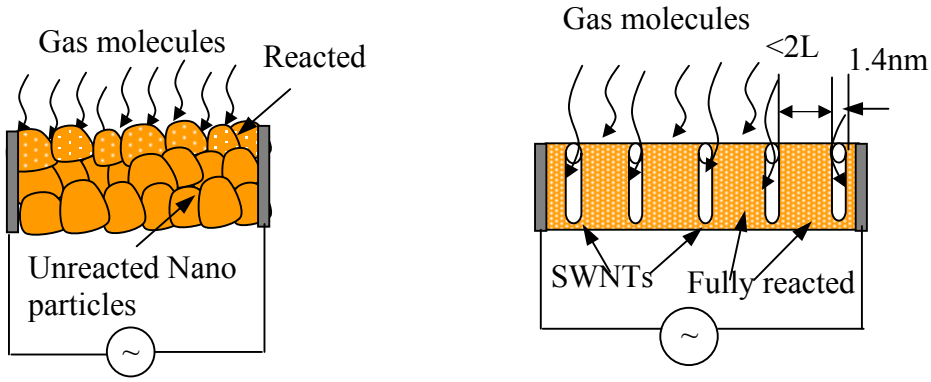


A: Sketch of dense nanograin sensing film that only top layer is reacted

B: Sketch of nano porous structured sensing film that all bulk material is reacted

Figure 76 Sketch of gas sensing mechanism between pure $SnO_2$film and $SnO_2$/SWNT film

Novel semiconductor sensing material consisting SMO/SWNT produces novel sensing mechanism[182]. SWNT will not only form nano gas passages, but also produce quantum effects between SWNT and nanostructured particles. In addition, surface to volume ratio of the SMO/SWNT will increase largely, as the tiny SWNT forms large quantity of additional surfaces. The enhanced sensitivity of nano $SnO_2$/SWNT thin film attributes to two aspects (as is sketched in Figure 76): 1) SWNT provides nano gas free

passages and 2) SWNT greatly reduces the distance between two adjacent reaction surfaces (wall-to-wall distance between two adjacent SWNT is less than Debye length --- 3nm for $SnO_2$). All film (not just the top surface) material will contribute to the response to gases.

## 6.4 Further Studies

As is mentioned in previous part, SWNT can be made semiconductive and metallic. For a batch of SWNT, metallic SWNT can be separated out from semiconductive SWNT by applying alternate electric fields[183]. The difference of using semiconductive and metallic SWNT for SWNT/$SnO_2$ need to be further studied. Besides, SWNT has proven gas sensor itself. Therefore, the synergistic function of SMO/SWNT as sensor could be further investigated.

In this research, the doped SWNT is in less than 0.1% weight percentage, however, the optimal doping concentration that can achieve the best sensitivity is still not known yet, and further systematic study should be conducted in this aspect.

# 7 DATA ANALYSIS MODEL FOR ELECTRIC NOSE

In this chapter, a data analysis model based on TSK Fuzzy Neural Network is brought out and the feasibility of using TSK Fuzzy neural network algorithm for Electric Nose has been exploited. Model construction and parameter identification through network learning is discussed in detail. Because of limited time and resources, this work is mainly focused on theoretical study and simulation. A training process of using TSK Fuzzy neural network with input/output pairs from individual gas sensor cell has been developed. The model has been proven valid by preliminary gas experimental results conducted. At last, further studies and efforts are discussed.

## 7.1 TSK Fuzzy Neural Network Modeling

### *7.1.1 System structure*

Without losing generality, we assume that there are S sensors in this gas measuring system, and G gases are to be measured based on the outputs of these sensors. The sensitivities of each sensor ($u_i$, i = 1~S) are fed into data processing system, which has a group of TSK FNN and each of them will generate a component gas concentration value ($o_j$, j = 1~G).

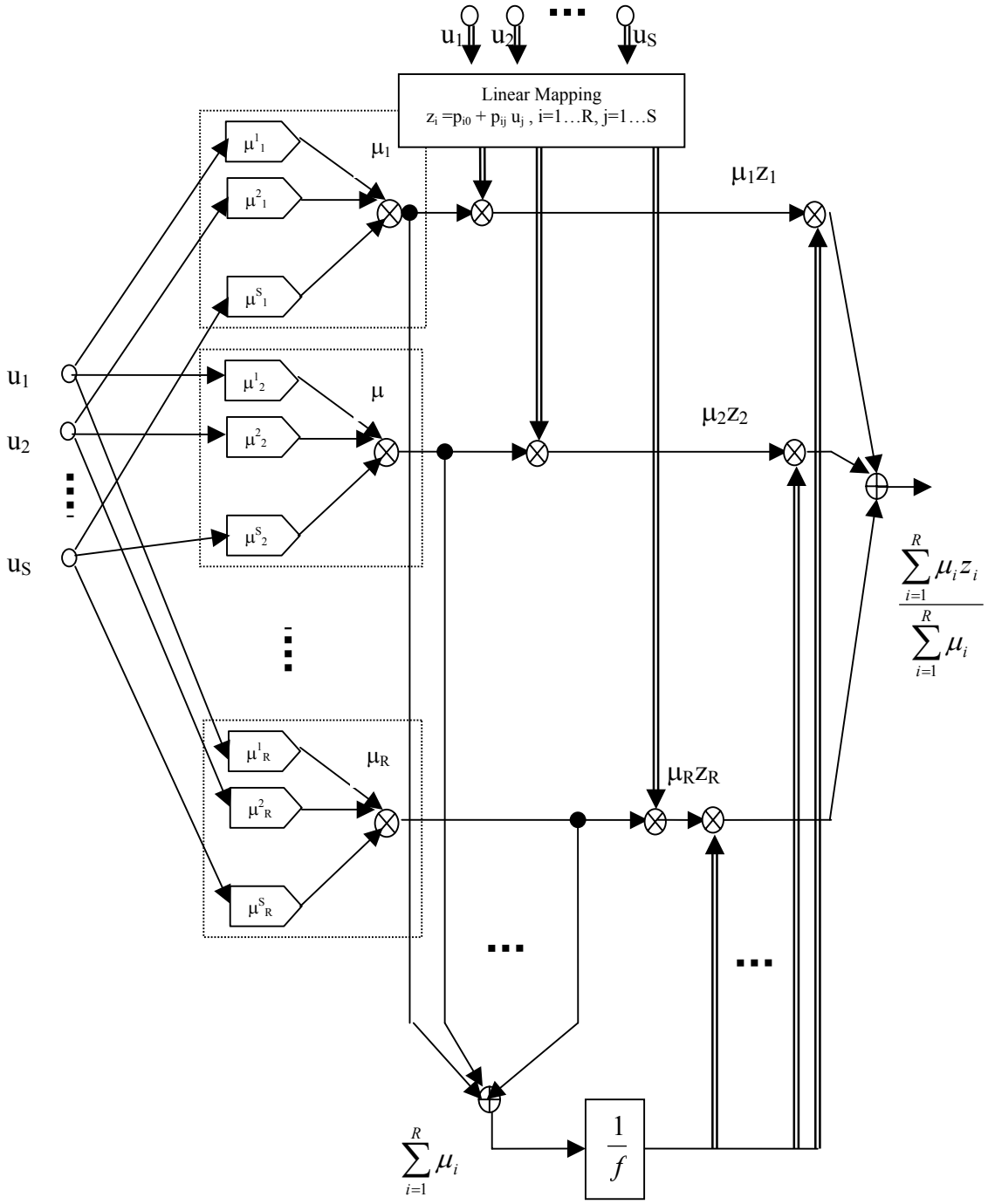


Figure 77 Individual TSK FNN structure

The multiplayer structure of an individual TSK FNN is shown in Figure 77. Each TSK fuzzy neural network in this data processing system is educated to respond in a specific gas and individually calculates a specific gas concentration. These TSK FNNs are actually independent of each other. This characteristic provides the gas measuring system some unique benefits like easy expansion with new measuring gases and possibility of concurrent learning. In addition to gas identification (distinguish the gases of interest), the output of the TSK FNN depends on gas concentration also. This can be considered as an improvement over the classical neural networks, which are trained to answer only with a simple 'yes' or 'no'.

The first layer is Input Layer. It consists of S input nodes and directly transmits the input variables (sensitivities $u_i$, i = 1,…,S) to the next layer.

The second layer is Fuzzification Layer which first performs the fuzzification according to the membership function $\mu_j(x_j)$, described by the Equation (8) [pp. 26]. Each node in this layer corresponds to one label of one of the input variables in Input Layer. Then layer aggregates the fuzzified results of the individual scalar variables and creates the membership function of the input vector u. This is the product type aggregation:

$$\mu_i = \prod_{j=1}^{S} \mu_i^j, i = 1, \cdots, R \tag{26}$$

Each node of this layer represents the firing strength of a rule.

The third layer, i.e. fuzzy rule layer, calculates the aggregated signals of the fuzzy inference for each inference rule (there are R rules of them). The output signal

corresponding to each rule is the product of the weighted firing strength of the rule ( $\mu_i \Big/ \sum_{j=1}^{R} \mu_j$ ) and the consequent membership value ($y_i$ from Equation (9) [pp. 26]), i.e.,

$$\text{ith rule signal} = y_i \cdot \mu_i \Big/ \sum_{j=1}^{R} \mu_j, i = 1, \cdots, R \tag{27}$$

The fourth layer, output layer, calculates only the sum of the signals of the third layer. According to the Equation (10) [pp. 26], this neuron computes the overall output signal, which after learning is expected to be the concentration of those to-be-measured gases.

*7.1.2 System preparation*

First we design and conduct N sets of measurements, whose results will be used as the training sample and validation data in the next phase. In the next step, parts of these N pair of data are presented to everyone of *G* (number of gases to be measured) TSK fuzzy neural network as the learning sample to construct the data processing system. Each pair of data consists of S sensitivity values, $\boldsymbol{u}$, and the specific component gas concentration values, *q*. We first determine the number of rules, R, of the TSK model. The number of rules of each TSK FNN depends on the way the input space is partitioned. Then we repeatedly feed the sensitivity values to TSK model and calculate the error between the output and the corresponding gas concentration value and adjust parameters of TSK model accordingly, until the TSK model yields a minimum error. This will automatically guarantee a minimum global modeling error defined in relation (28). Thus

the parameters in membership functions of each rule and those in linear mapping functions are determined. The construction of data processing system, as well as the identification TSK parameters is detailed in the following paragraphs.

Global Modeling Error: $$\|\varepsilon\|^2 = \sum_{i=1}^{N}\sum_{j=1}^{G}\left\|o_{i,j} - q_{i,j}\right\|^2 \quad (28)$$

where $o$ is the actual output of data processing system, $q$ is the expected output, $N$ is the number of training pairs, and $G$ is number of gases to be measured.

*7.1.3 Structure identification of the TSK fuzzy neural network model*

Construction of the data processing system can be divided into sub-tasks of constructing each individual TSK FNN structure. In general, construction of a FNN involves two phases: structure identification and parameter identification. In the first phase of structure identification, fuzzy rules are extracted from data set; then these fuzzy rules are further optimized in the second phase of parameter identification. As for the TSK neural network, we have to identify the number of TSK fuzzy rules in the structure identification phase and optimize the parameters of in both consequences ($p_{ij}$ of the linear mapping functions) and premises ($c$ and $\sigma$ of membership functions). Pairs of input and corresponding output are presented to neural network, and techniques are utilized to optimize the parameters of TSK.

It's obvious that less number of parameters to be tuned, the easier and faster the training procedure will be. In practical, the number of rules of each TSK FNN depends

on the way the input space is partitioned. In this model, we have 4 inputs and 2 membership functions (Yes or No) for each input, therefore, the total fuzzy rules should be $2^4$=16 rules and the number of nonlinear parameters is 16, and the number of linear parameters $p_{ij}$ is 16 x 5 x 7=560. The multiplayer structure of an individual TSK FNN is shown in Figure 77.

*7.1.4 Parameter identification through training*

After R initial rules are generated, a hybrid-learning algorithm will be applied for optimizing the parameters in both premise and consequent structures. In the forward pass, the premise parameters are fixed and the consequent parameters are identified by Recursive Singular Value Decomposition (RSVD) algorithm. In the backward pass, the consequent parameters are fixed, and the error signals are propagated backward to tune the premise parameters by the gradient decent method. The detail of this hybrid learning is reported in reference papers [72, 73].

7.1.4.1 Forward passing using RLSE

Let $(\vec{u}_v, q_v)$ be the $v$th training pair, where $\vec{u}_v = [u_{1v}, u_{2v}, \cdots, u_{sv}]$ is the sensitivity vector and $q_v$ is the corresponding component gas concentration value. The actual output $o_v$ of TSK model is, by equation (10) [pp. 26] above

$$o_v = w_{v1} z_{v1} + w_{v2} z_{v2} + \cdots w_{vR} z_{vR}, \tag{29}$$

where $w_{vj} = \dfrac{\mu_{vj}}{\sum_{i=1}^{R} \mu_{vi}}$, for $1 \le j \le R$, and $z_{vj} = p_{0j} + p_{1j} u_{v1} + \cdots + p_{sj} u_{vs}$.

The modeling error of individual TSK FNN can be expressed as $J = \sum_{i=1}^{N} \| q_i - o_i \|$, where N is the number of training pairs. The minimization of the global modeling error (28) can be achieved by minimize the error $J$ of each individual TSK. By introducing the equation (29), the error $J$ can be rewritten as

$$J(X) = \| B - AX \|, \tag{30}$$

where **B**, **A** and **X** are matrices of $N \times 1$, $N \times R(S+1)$, and $R(S+1) \times 1$ respectively,

$$B = [q_1, q_2, \cdots q_N]^T,$$

$$A = \begin{bmatrix} w_{11} & w_{21} & \cdots & w_{N1} \\ w_{11}u_{11} & w_{21}u_{21} & \cdots & w_{N1}u_{N1} \\ \vdots & \vdots & \ddots & \vdots \\ w_{11}u_{1S} & w_{21}u_{2S} & \cdots & w_{N1}u_{NS} \\ w_{12} & w_{22} & \cdots & w_{N2} \\ w_{12}u_{11} & w_{22}u_{21} & \cdots & w_{N2}u_{N1} \\ \vdots & \vdots & \ddots & \vdots \\ w_{12}u_{1S} & w_{22}u_{2S} & \cdots & w_{N2}u_{NS} \\ \vdots & \vdots & \ddots & \vdots \\ \vdots & \vdots & \ddots & \vdots \\ w_{1R} & w_{2R} & \cdots & w_{NR} \\ w_{1R}u_{11} & w_{2R}u_{21} & \cdots & w_{NR}u_{N1} \\ \vdots & \vdots & \ddots & \vdots \\ w_{1R}u_{1S} & w_{2R}u_{2S} & \cdots & w_{NR}u_{NS} \end{bmatrix}^T_{N \times S \times (R+1)} = \left[ \vec{g}_1, \vec{g}_2, \cdots, \vec{g}_N \right]^T,$$

$$X = [p_{01,} p_{11,} \cdots p_{S1}, p_{02,} p_{12,} \cdots p_{S2}, \cdots\cdots, p_{0R,} p_{1R,} \cdots p_{SR}]^T_{S \times (R+1)} \tag{31}$$

Note that for the matrix D, $\|D\|$ is defined to be $\sqrt{trace(D^T D)}$. In the forward passing, since **B** and **A** are constant, **X** is the only variable vector, and can be optimized using Recursive Least Squares Estimator.

For a matrix A of Equation (31), it can be decomposed as $A = U\Sigma V^T$, where U is an N x N orthonormal matrix, V is a S x S orthonormal matrix, and $\Sigma$ is an NxS diagonal matrix with each component $\Sigma_{ij}$ being:

$$\Sigma_{ij} = \begin{cases} 0, if\ i \neq j \\ e_i, otherwise \end{cases} \quad (32)$$

where $e_i^2$ are eigenvalues of $A^T A$, and $e_1 \geq e_2 \geq ....e_r$, with r=min(N, S). The corresponding eigenvectors of $AA^T$ form the columns of U, and the corresponding eigenvectors of $A^T A$ form the columns of V.

Now, (30) can be rewritten as $J(X) = \|B - U\Sigma VX\|$, and we since U is an orthonormal matrix, we have

$$J(X) = \|U^T B - U^T U\Sigma VX\| = \|U^T B - \Sigma VX\| \quad (33)$$

$\Sigma$ can be rewritten as: $\Sigma = \begin{bmatrix} \Sigma' \\ 0 \end{bmatrix}$, where $\Sigma'$ is an $h \times S$ matrix with h being the rank of A and all the diagonal components of $\Sigma'$ being greater than 0. Let $U^T B = \begin{bmatrix} B' \\ B'' \end{bmatrix}$, where $B'$ is a $h \times 1$ matrix and $B''$ is a $(N-h) \times 1$ matrix. Then (33) can be rewritten as

$$J(X) = \left\| \begin{bmatrix} B' \\ B'' \end{bmatrix} - \begin{bmatrix} \Sigma' \\ 0 \end{bmatrix} Y \right\| = \begin{Vmatrix} B' - \Sigma' Y \\ B'' \end{Vmatrix} \quad (34)$$

where $Y = V^T X$ . Apparently, (34) is minimized by Y* such that $B' - \Sigma' Y = 0$ , i.e. $\Sigma' Y^* = B'$, therefore, the optimal solution X* that minimize (30) is X*=VY*.

7.1.4.2 Backward passing using gradient decent method

As discussed above, parameters ($c_{ij}$, $\sigma_{ij}$) in premise are refined by gradient decent method. The error function we consider is

$$E = \frac{1}{2N}\sum_{v=1}^{N}(o_v - q_v)^2 , \qquad (35)$$

where $q$ is desired output and $o$ is the actual output of TSK FNN.

The learning rule for $c_{ij}$ is

$$c_{ij}^{new} = c_{ij}^{old} - \eta_1 (\frac{\partial E}{\partial c_{ij}}) , \qquad (36)$$

where $\eta_1$ is a predefined learning rate and

$$\begin{aligned}
\frac{\partial E}{\partial c_{ij}} &= \frac{1}{N}\sum_{v=1}^{N}[(o_v - q_v)\frac{\partial o_v}{\partial c_{ij}}] \\
&= \frac{1}{N}\sum_{v=1}^{N}[(o_v - q_v)\frac{z_j - o_v}{\sum_{r=1}^{R}\mu_r}\frac{\partial \mu_{vj}}{\partial c_{ij}}] \\
&= \frac{1}{N}\sum_{v=1}^{N}[(o_v - q_v)\frac{(z_j - o_v)\mu_{vj}}{\sum_{r=1}^{R}\mu_r}\frac{\partial\left[-(\frac{u_{iv} - c_{ij}}{\sigma_{ij}})^2\right]}{\partial c_{ij}}] \\
&= \frac{2}{N}\sum_{v=1}^{N}[(o_v - q_v)\frac{(z_j - o_v)\mu_{vj}(u_{iv} - c_{ij})}{(\sum_{r=1}^{R}\mu_r)\sigma_{ij}^{\ 2}}]
\end{aligned}$$

Similarly, the update rule of $\sigma_{ij}$ is derived as

$$\sigma_{ij}^{new} = \sigma_{ij}^{old} - \eta_2 (\frac{\partial E}{\partial \sigma_{ij}}), \qquad (37)$$

where $\eta_2$ is a predefined learning rate and

$$\frac{\partial E}{\partial \sigma_{ij}} = \frac{2}{N} \sum_{v=1}^{N} [(o_v - q_v) \frac{(z_j - o_v)\mu_{vj}(u_{iv} - c_{ij})^2}{(\sum_{r=1}^{R} \mu_r)\sigma_{ij}^3}]$$

where zj is from linear mapping polynomial.

*7.1.5 System validation*

As we can see in the system preparation step, only part of data is used as training sample. We will use the remaining part as the validation data to test the performance of the optimized data processing system. The mean absolute error (MAE) and mean absolute percentage error (MAPE) are defined as the validation criteria. For each *j*th (j = 1,…,G) component of the mixture the MAE error is defined as

$$MAE_j = \sum_{i=1}^{p} \left| z_i^{(j)} - r_i^{(j)} \right| \qquad (38)$$

where $r_j$ means the real concentration of the *j*th gas component, and $z_j$ is the predicted value. On the basis of MAE for individual components we have also defined the average MAE error for the whole testing set.

The second measure of errors introduced in this work is the relative one, defined as the mean absolute percentage error. For each jth component it is defined as following:

$$MAPE_j = \sum_{i=1}^{p} \frac{\left| z_j^{(k)} - r_j^{(k)} \right|}{r_j^{(k)}} \qquad (39)$$

## 7.2 Simulation

Simulation is necessary for parameter evaluation before the system is finalized. In this research, we only performed some experiments for a preliminary validation of system model. To be more specific, we plan to use this E-nose system for $H_2S$ analysis (not a very complex analysis system). The sensor array has employed 4 sensors, namely, UCF1 (quartz substrate device with $SnO_2$+Ag film), UCF2 (ceramic substrate device with $SnO_2$+Ag film), Figaro (Tin oxide) sensor TGS825 and Bacharach ($WO_3$) sensor. Seven gases, i.e. $CH_4$ (2.2%), HCL (10ppm), HCN (10ppm), CO (50ppm), $SO_2$ (9ppm), $NO_2$ (5ppm) was used as interference gases and 3ppm ~50ppm $H_2S$ as targeting gas. The array of these S (=4) sensors are tested in a gas chamber. All measurements are carried out with air as carrier gas and with $CH_4$ (2.2%), HCL (10ppm), HCN (10ppm), CO (50ppm), $SO_2$ (9ppm), $NO_2$ (5ppm) and (3ppm~50ppm) $H_2S$ as target gas, and therefore, the number of gas spices to be identified is G=7. The gas flux was kept constant. We recorded the responses of 4 sensors in each experiment. Figure 78 shows sensitivity of sensor array to different interference gases and a summary of Sensitivity $S_1$ shown in Table 16.

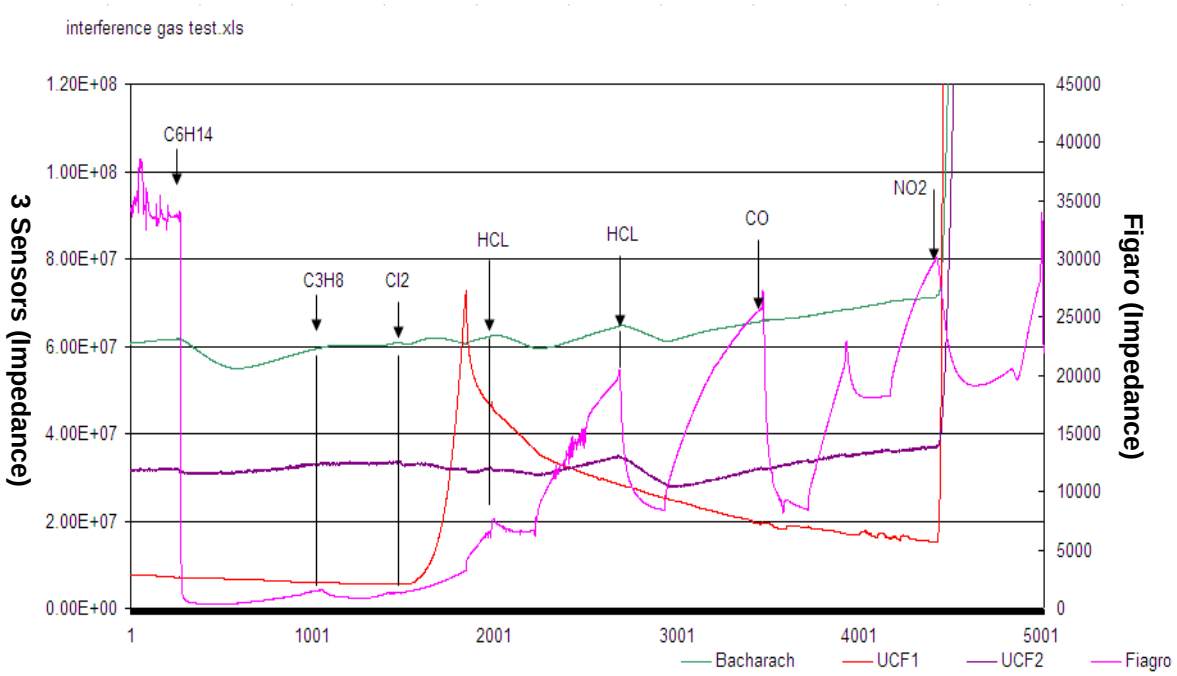


Figure 78 Sensitivity of sensor array to different targeting gases

Table 16 Sensitivity summary to interference gases (S1 = $(R_0-R_1)/R_0$)

| | $CH_4$ (2.2%) | HCL (10ppm) | HCN (10ppm) | CO (50ppm) | $SO_2$ (9ppm) | $NO_2$ (5ppm) |
|---|---|---|---|---|---|---|
| Bacharach | 0 | 0.0440 | 0.0910 | 0.9200 | -0.0800 | -1.8100 |
| Figaro | 0.8940 | 0.3800 | 0.5320 | 0.8940 | 0.4160 | 0.3450 |
| UCF-1 | 0.3780 | 0.0390 | 0.0720 | 0.1600 | -0.5260 | -130.57 |
| UCF-2 | 0.0450 | 0.0590 | 0.0490 | 0 | -0.0630 | -53.00 |

Data from 3 step concentration test of $H_2S$ is listed in Table 17 ~ Table 19. We used dataset1 for forward training, dataset2 for backward training and dataset 3 for validation. The sensitivity is defined as (S1 = $(R_0-R_1)/R_0$), which is in (0, 1) range.

Table 17 Sensitivity summary to $H_2S$ dataset 1 used for backward passing training

| | $H_2S$ (3ppm) | $H_2S$ (6ppm) | $H_2S$ (10ppm) | $H_2S$ (15ppm) | $H_2S$ (20ppm) | $H_2S$ (25ppm) | $H_2S$ (50ppm) |
|---|---|---|---|---|---|---|---|
| Bacharach | 0.4000 | 0.8500 | 0.9500 | 0.9800 | 0.9900 | 0.9900 | 0.9900 |
| Figaro | 0.1900 | 0.5400 | 0.7500 | 0.8200 | 0.8200 | 0.8200 | 0.8200 |
| UCF-1 | 0.9000 | 0.9800 | 0.9900 | 0.9900 | 0.9900 | 0.9900 | 0.9900 |
| UCF-2 | 0.4000 | 0.8200 | 0.9200 | 0.9600 | 0.9700 | 0.9800 | 0.9900 |

Note: Sensitivity test of $H_2S$ in range of 3ppm~50ppm can be found in Figure 59 [97]

Table 18 Sensitivity summary to $H_2S$ dataset 2 used for backward passing training

| | $H_2S$ (3ppm) | $H_2S$ (6ppm) | $H_2S$ (10ppm) | $H_2S$ (15ppm) | $H_2S$ (20ppm) | $H_2S$ (25ppm) | $H_2S$ (50ppm) |
|---|---|---|---|---|---|---|---|
| Bacharach | 0.4100 | 0.8600 | 0.9400 | 0.9900 | 0.9900 | 0.9900 | 0.9900 |
| Figaro | 0.1800 | 0.5200 | 0.7700 | 0.8400 | 0.8700 | 0.9100 | 0.9300 |
| UCF-1 | 0.8800 | 0.9700 | 0.9800 | 0.9900 | 0.9900 | 0.9900 | 0.9900 |
| UCF-2 | 0.3600 | 0.8400 | 0.9100 | 0.9500 | 0.9600 | 0.9700 | 0.9900 |

Table 19 Sensitivity summary to $H_2S$ dataset 3 used for validation

| | $H_2S$ (3ppm) | $H_2S$ (6ppm) | $H_2S$ (10ppm) | $H_2S$ (15ppm) | $H_2S$ (20ppm) | $H_2S$ (25ppm) | $H_2S$ (50ppm) |
|---|---|---|---|---|---|---|---|
| Bacharach | 0.3600 | 0.8400 | 0.9500 | 0.9800 | 0.9900 | 0.9900 | 0.9900 |
| Figaro | 0.1500 | 0.6600 | 0.7500 | 0.8500 | 0.8800 | 0.9000 | 0.9400 |
| UCF-1 | 0.8800 | 0.9700 | 0.9800 | 0.9900 | 0.9900 | 0.9900 | 0.9900 |
| UCF-2 | 0.3800 | 0.8500 | 0.9200 | 0.9600 | 0.9700 | 0.9800 | 0.9900 |

*7.2.1 Forward passing training*

Assume of sensitivity value taken from different test statistically follow Gaussian distribution, we choose Gaussian function as the membership function, as is given in Equation (8) [27]. First, we will train one TSK model that is specified for $H_2S$ output. In forward passing training, we will fix two member function parameter c and σ, from the data in the training dataset; we calculate c and σ using statistic knowledge as listed in Table 20.

Table 20 Membership function parameters c and σ

| | | $H_2S$ (3ppm) | $H_2S$ (6ppm) | $H_2S$ (10ppm) | $H_2S$ (15ppm) | $H_2S$ (20ppm) | $H_2S$ (25ppm) | $H_2S$ (50ppm) |
|---|---|---|---|---|---|---|---|---|
| Bach. | c | 0.3900 | 0.7367 | 0.9450 | 0.9833 | 0.9900 | 0.9900 | 0.9900 |
| | σ | 0.0265 | 0.0100 | 0.0071 | 0.0058 | 0.0001 | 0.0001 | 0.0001 |
| Figaro | c | 0.1733 | 0.5733 | 0.7600 | 0.8367 | 0.8567 | 0.8767 | 0.8967 |
| | σ | 0.0208 | 0.0757 | 0.0141 | 0.0153 | 0.0321 | 0.0493 | 0.0666 |
| UCF-1 | c | 0.8867 | 0.9767 | 0.9850 | 0.9900 | 0.9900 | 0.9900 | 0.9900 |
| | σ | 0.0115 | 0.0058 | 0.0071 | 0.0001 | 0.0001 | 0.0001 | 0.0001 |
| UCF-2 | c | 0.3800 | 0.8367 | 0.9150 | 0.9567 | 0.9667 | 0.9767 | 0.9900 |
| | σ | 0.0200 | 0.0153 | 0.0071 | 0.0058 | 0.0058 | 0.0058 | 0.0001 |

Let $(\vec{u}_v, q_v)$ be the $v$th training pair, where $\vec{u}_v = [u_{1v}, u_{2v}, \cdots, u_{sv}]$ is the sensitivity vector and $q_v$ is the corresponding component gas concentration value, therefore, we have the training vector:

$$(\vec{u},q)_1=(\begin{bmatrix}0.4000 & 0.8500 & 0.9500 & 0.9800 & 0.9900 & 0.9900 & 0.9900\\ 0.1900 & 0.5400 & 0.7500 & 0.8200 & 0.8200 & 0.8200 & 0.8200\\ 0.9000 & 0.9800 & 0.9900 & 0.9900 & 0.9900 & 0.9900 & 0.9900\\ 0.4000 & 0.8200 & 0.9200 & 0.9600 & 0.9700 & 0.9800 & 0.9900\end{bmatrix},[3\ 6\ 10\ 15\ 20\ 25\ 50])$$

First, we use dataset 1 for training, i.e. N=7, because there are 4 sensors, we choose rule number to be $R=2^4=16$, and the member function can be derived by Equation (8) [27]

$$\mu=\begin{bmatrix}
0.8673 & 0.0000 & 0.6090 & 0.7235 & 1.0000 & 1.0000 & 1.0000\\
0.0000 & 0.0000 & 0 & 0 & 0 & 0 & 0\\
0.0000 & 0.0000 & 0.0000 & 0.2633 & 1.0000 & 1.0000 & 1.0000\\
0.8673 & 0.0000 & 0.0000 & 0.0000 & 0 & 0 & 1.0000\\
0 & 0 & 0 & 0 & 0 & 0 & 0\\
0 & 0.0000 & 0.0000 & 0.0000 & 0.0000 & 0.0051 & 0.1405\\
0 & 0 & 0 & 0 & 0 & 0 & 0\\
0.0000 & 0.0000 & 0.0000 & 0.0000 & 0.0000 & 0.0124 & 0.1405\\
0.2625 & 0.7235 & 0.6090 & 1.0000 & 1.0000 & 1.0000 & 1.0000\\
0 & 0 & 0 & 0 & 0 & 0 & 0\\
0 & 0 & 0 & 0 & 0 & 0 & 0\\
0 & 0.0000 & 0.0000 & 0 & 0 & 0 & 1.0000\\
0 & 0 & 0 & 0 & 0 & 0 & 0\\
0 & 0 & 0 & 0 & 0 & 0 & 0\\
0 & 0 & 0 & 0 & 0 & 0 & 0\\
0.3679 & 0.3038 & 0.6090 & 0.7235 & 0.7235 & 0.7235 & 1.0000
\end{bmatrix} \quad (40)$$

From $w_{vj}=\frac{\mu_{vj}}{\sum_{i=1}^{R}\mu_{vi}}$, we can derive w:

$$w=\begin{bmatrix}
0.3667 & 0.0000 & 0.3333 & 0.2669 & 0.2686 & 0.2673 & 0.1592 \\
0.0000 & 0.0000 & 0 & 0 & 0 & 0 & 0 \\
0.0000 & 0.0000 & 0.0000 & 0.0972 & 0.2686 & 0.2673 & 0.1592 \\
0.3667 & 0.0000 & 0.0000 & 0.0000 & 0 & 0 & 0.1592 \\
0 & 0 & 0 & 0 & 0 & 0 & 0 \\
0 & 0.0000 & 0.0000 & 0.0000 & 0.0000 & 0.0014 & 0.0224 \\
0 & 0 & 0 & 0 & 0 & 0 & 0 \\
0.0000 & 0.0000 & 0.0000 & 0.0000 & 0.0000 & 0.0033 & 0.0224 \\
0.1110 & 0.7042 & 0.3333 & 0.3690 & 0.2686 & 0.2673 & 0.1592 \\
0 & 0 & 0 & 0 & 0 & 0 & 0 \\
0 & 0 & 0 & 0 & 0 & 0 & 0 \\
0 & 0.0000 & 0.0000 & 0 & 0 & 0 & 0.1592 \\
0 & 0 & 0 & 0 & 0 & 0 & 0 \\
0 & 0 & 0 & 0 & 0 & 0 & 0 \\
0 & 0 & 0 & 0 & 0 & 0 & 0 \\
0.1556 & 0.2957 & 0.3333 & 0.2669 & 0.1943 & 0.1934 & 0.1592
\end{bmatrix} \quad (41)$$

From Equation (31) [127], we got the matrix A as a 80 x7 matrix, and

$X = (p_{01,}p_{11,}\cdots p_{S1}, p_{02,}p_{12,}\cdots p_{S2}, \cdots\cdots, p_{0R,}p_{1R,}\cdots p_{SR})^T$ as a 1 x 80 vector. The error $J$ is $J(X) = \|B - AX\|$, We further do single value decomposition of A, and $J$ can be rewritten as $J(X) = \|B - U\Sigma VX\|$, we have $J(X) = \|U^T B - U^T U\Sigma VX\| = \|U^T B - \Sigma VX\|$, $\Sigma$ can be rewritten as: $\Sigma = \begin{bmatrix}\Sigma' \\ 0\end{bmatrix}$, where $\Sigma'$ is an $h \times S$ matrix with h being the rank of A, which is 7, and all the diagonal components of $\Sigma'$ being greater than 0.

We got $\begin{bmatrix}
1.8699 & 0 & 0 & 0 & 0 & 0 & 0 \\
0 & 0.51309 & 0 & 0 & 0 & 0 & 0 \\
0 & 0 & 0.29177 & 0 & 0 & 0 & 0 \\
0 & 0 & 0 & 0.27785 & 0 & 0 & 0 \\
0 & 0 & 0 & 0 & 0.15139 & 0 & 0 \\
0 & 0 & 0 & 0 & 0 & 0.034975 & 0 \\
0 & 0 & 0 & 0 & 0 & 0 & 0.0027538
\end{bmatrix}$

Considering $B = [q_1, q_2, \cdots q_N]^T = [3\ 6\ 10\ 15\ 20\ 25\ 50\ ]^T$,

$U^T B = \begin{bmatrix} B' \\ B'' \end{bmatrix} = \begin{bmatrix} -13.0712 \\ -8.5727 \\ 28.7223 \\ -15.8185 \\ -39.9908 \\ 31.1801 \\ 1.9988 \end{bmatrix}$, where $B'$ is a $h \times 1$ matrix and $B''$ is a $(N-h) \times 1$ matrix. To

minimize $J(X) = \left\| \begin{bmatrix} B' \\ B'' \end{bmatrix} - \begin{bmatrix} \Sigma' \\ 0 \end{bmatrix} Y \right\| = \left\| \begin{matrix} B' - \Sigma' Y \\ B'' \end{matrix} \right\|$, we want $B' - \Sigma' Y = 0$, i.e., $\Sigma' Y^* = B'$,

where $Y = V^T X$. Therefore, the optimal solution X* that minimize J(X) is X*=VY*.

We have $Y^* = \begin{bmatrix} -6.9903 \\ -16.7080 \\ 98.4415 \\ -56.9317 \\ -264.1578 \\ 891.4961 \\ 725.8304 \end{bmatrix}$

$$X^* = VY^* = \begin{bmatrix} 295.3492 & 0 & 274.6741 & 113.3788 \\ 0 & 17.2737 & 0 & 18.9979 \\ 280.3696 & 0 & 0 & 114.4040 \\ 0 & 0 & 0 & 245.9181 \\ 0 & 232.8814 & 0 & 0 \\ 0 & 0 & 0 & 94.7588 \\ 0 & 0 & 279.5545 & 0 \\ 0 & 0 & 0 & 203.3183 \\ 0 & 0 & 0 & 114.4040 \\ 0 & 0 & 0 & 0 \\ 0 & 0 & 0 & 0 \\ 0 & 0 & 0 & 245.8927 \\ 0 & 0 & 0 & 0 \\ 0 & 0 & 0 & 0 \\ 0 & 0 & 0 & 0 \\ 0 & 0 & 0 & 244.6883 \end{bmatrix} \quad (42)$$

Result (42) shows the polynomial parameters $p_{RS}$ after training process (dataset N=7).

Similarly, other TSK structure for interference gases can be trained following the same process.

*7.2.2 Backward passing training*

When polynomial parameters $p_{RS}$ are determined by forward passing training, parameters ($c_{ij}$, $\sigma_{ij}$) in premise are refined by gradient decent method, which is discussed in the previous section [129]. Dataset2 [133] is used for this backward passing training. We can choose the learning rate $\eta$ to be 1.05, goal to be 0.001, epochs to be 500, and the original membership function parameter as defined in the previous section. The detail steps of training process are not listed here. The final parameters c and σ are:

$$c = \begin{bmatrix} 0.3900 & 0.8400 & 0.9450 & 0.9800 & 0.9900 & 0.9900 & 0.9900 \\ 0.1800 & 0.5500 & 0.7400 & 0.8200 & 0.8800 & 0.9000 & 0.9600 \\ 0.9000 & 0.9800 & 0.9800 & 0.9900 & 0.9900 & 0.9900 & 0.9900 \\ 0.3900 & 0.8300 & 0.9200 & 0.9700 & 0.9750 & 0.9800 & 0.9900 \end{bmatrix}$$

$$\sigma = \begin{bmatrix} 0.0265 & 0.0200 & 0.0271 & 0.0058 & 0.0101 & 0.0101 & 0.0101 \\ 0.0208 & 0.0657 & 0.0141 & 0.0153 & 0.0321 & 0.0493 & 0.0666 \\ 0.0215 & 0.0158 & 0.0071 & 0.0011 & 0.0101 & 0.0101 & 0.0101 \\ 0.0220 & 0.0253 & 0.0161 & 0.0158 & 0.0158 & 0.0158 & 0.0001 \end{bmatrix}$$

*7.2.3 Validation*

Dataset3 [133] is used for validation. A result comparison of TSK Fuzzy Neural network and common Backpropagation Neural Network with Widrow-Hoff learning rule is listed in Table 21.

Table 21 Comparison of TSK FNN and Backpropagation NN

(a) Output of trained TSK fuzzy neural network

| Actual | 3ppm | 6ppm | 10ppm | 15ppm | 20ppm | 25ppm | 50ppm |
|---|---|---|---|---|---|---|---|
| Output | 1.8683 | 7.8611 | 10.3768 | 22.6773 | 26.9786 | 29.8722 | 33.8099 |

(b) Output Backpropagation neural network with Widrow-Hoff learning rule

| Actual | 3ppm | 6ppm | 10ppm | 15ppm | 20ppm | 25ppm | 50ppm |
|---|---|---|---|---|---|---|---|
| Output | 1.2433 | 8.8162 | 17.4715 | 26.7189 | 29.2726 | 30.5482 | 32.0408 |

(c) Comparison of MAE and MAPE

MAE: mean absolute error: $MAE = \frac{1}{p}\sum_{i=1}^{p}\left|z_i^{(j)} - r_i^{(j)}\right|$

MAPE: mean absolute percentage error: $MAPE = \frac{1}{p}\sum_{i=1}^{p}\frac{\left|z_i^{(j)} - r_i^{(j)}\right|}{r_i^{(k)}}$

Table 22 Comparison of MAE and MAPE

| $MAE_{FC}$ | $MAPE_{FC}$ | $MAE_{BP}$ | $MAPE_{BP}$ |
|---|---|---|---|
| 4.7ppm | 27% | 5.8ppm | 47.65% |

From the comparison shown in Table 22, we can see that TSK Fuzzy Neural network obtained more accuracy, which indicates that it has better ability dealing with non-linear classification problems. However, it also can be seen that MAE and MAPE is still large, the reasons for that is, since all 4 four sensor have good sensitivity to $H_2S$ at higher concentration, which make sensor works at its saturation stage, therefore, it is very difficult to differentiate.

For all the other interference gases classification, we will use the same strategy as is discussed above and will not be explained in detail here.

## 7.3 Further Studies and Efforts

Further Electric Nose system studies and development include hardware implementation and data processing. Hardware implementation will be focused on DSP based system design which includes DSP processor, A/D converter, D/A converter, Temperature feedback control circuit, power supply, display panel and wireless communication part. The finalized algorithm will be burned into DSP build in ROM in hardware realization. The to-be-developed Electric Nose System is sketched in Figure 79.

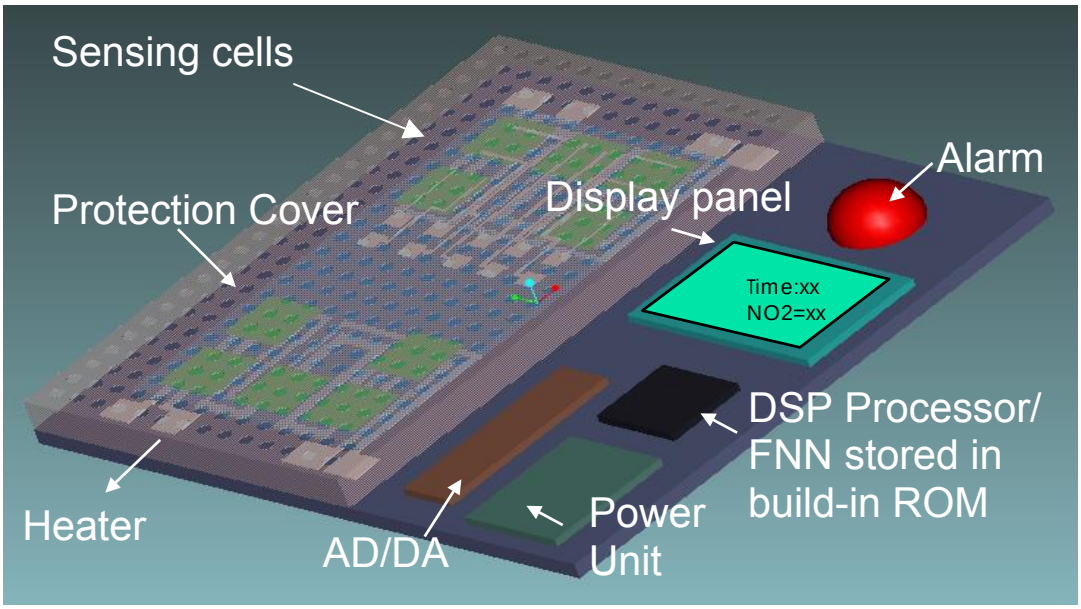


Figure 79 Future electric nose system sketch

In this research, Data processing was focused on improvement of fuzzy neural network algorithm, besides of TSK FNN, other neural network models or Fuzzy neural network models are worth examining programming. For example, a popular neural network model architecture called Fuzzy ARTMAP[184] has the ability to solve any classification problem quickly, and at the same time provide explanations for its answers in terms of fuzzy-if-then rules of similar nature as the ones provided by the TSK FNN model. More systematic experiments are also needed for better Fuzzy Neural Network training and model evaluation.

# 8 CONCLUSIONS AND OUTLOOKS

## 8.1 Conclusions

In this dissertation, a systematic study has been conducted on non-silicon Semiconductor Metal Oxide (SMO) gas sensors, in terms of design and fabrication, nano material preparation and characterization, thermal characterization, gas sensitivity, environmental influence on sensors, etc. A feedback temperature control circuit is invented to eliminate temperature influence on SMO sensors. This research also explored the feasibility of using TSK Fuzzy neural network algorithm for Electric Nose system smart enough to measure gas concentration in a gas mixture environment. The model has been proven valid by preliminary gas experimental results conducted.

In a summary, this study leads to the following conclusions:

- Nanocrystalline tin oxide ($SnO_2$) was obtained from by a chemical sol gel route, the SEM picture shows the grain size of acquired $SnO_2$ film in 10~20nm, depending on the annealing temperature. Nanocrystalline tungsten oxide ($WO_3$) and indium oxide ($In_2O_3$) can also be obtained by sol gel route.
- Two types of non-silicon of gas sensor were designed and fabricated in this stage of research; both of them have good performance as SMO gas sensor. However,

the power consumption is still high for commercial purpose application. Thermal characterization shows that silicon based gas sensor with membrane type design has more advantages in reducing power consumption. Additionally, packaging of final gas sensor device should include housing cap, which will provide protection and prevent air convections.

- Relative humidity has big influence on SMO sensors and it makes SMO sensor resistance decrease its value in both pure air (baseline resistance) and gas presence ambiences. Humidity sensor could be incorporated to measure the environmental R.H. and compensate adjusting value to sensor resistance by either software algorithm or hardware instrumentation. Another possible solution could be using data processing method like Fuzzy Neural Network to eliminate this effect.

- The invented temperature feedback control circuit has significantly improved the sensor's stability by eliminating ambient temperature influences on SMO sensor. However, further efforts are still needed to optimize designs parameters like feedback gain, thermal mass and thermal distributions.

- The author and his colleagues found that light has influence on SMO sensor, $SnO_2$/Ag sensor for example. Sensor resistance increase when light is on and decrease when light is off. This phenomenon can be explained by Bohr Model. This discovery hasn't appear in relative technique papers or literatures based on the author's knowledge.

- The author and his advisor also found that $SnO_2$/SWNT sensor has improved sensitivity to targeting gas (Hydrogen for example), compared to pure $SnO_2$ sensor. This novel semiconductor gas sensing material produces novel sensing mechanism[185]. SWNT not only forms the nano gas passages, but also produces quantum effects between SWNT and nanostructured particles. In addition, surface to volume ratio of the SMO/SWNT increases largely, as the tiny SWNT forms large quantity of additional surfaces.

- Gas sensor with nanocrystalline $SnO_2$ thin film doped with Ag/Pt has very good performance on Hydrogen detection. Fairly good sensitivity can be achieved at 100°C, and better results have been achieved at higher temperatures such as 200°C and 250°C. It also has faster response time and quicker recovery time compared to other reported $H_2$ gas sensors.

- Gas sensor with nanocrystalline $SnO_2$ thin film doped with Ag has excellent performance on Hydrogen Sulfide detection. Ultrahigh sensitivity can be achieved at working temperature as low as 70°C. Compared to some commercial available $H_2S$ sensors, this sensor has merits such as better sensitivity, fairly good response time and recovery time, less effects from interference gases.

- The quartz based $SnO_2$ gas sensor doped wtih Pt as catalyst has good performance on Carbon Monoxide detection. This CO sensor has a fast response time (1s) and quick recovery time (3s) to 100ppm CO, as well as very good sensitivity to as low concentration as 0.1ppm of CO.

- The feasibility of using TSK Fuzzy neural network algorithm for gas sensor array has been exploited during the research. The training process is studied and developed. TSK Fuzzy neural network is a powerful model that make Electric nose smart enough to measure gas concentrations in a gas mixture. The model has been proven valid by preliminary gas experimental results conducted.

## 8.2 Outlooks

Many avenues for further research remain for extending the current work, some of which are suggested and described below:

- The influence of semi conductive or metallic SWNT used in SWNT/$SnO_2$ gas sensor in terms of sensitivity, response and recovery time etc. need to be further examined. Besides, SWNT has proven gas sensor itself. Therefore, the synergistic function of SMO/SWNT as sensor should be further investigated.

- As is discussed in the Chapter 3, two aspects need to be considered in order to further minimize gas sensor's power consumption: optimized microhotplate structure and housing package. There are a lot of challenges for optimization design of microhotplate structure, both in thermal and mechanical aspects. Improvement for better temperature feedback control should also be considered during design stage. FEM analysis is good tool in helping to achieve this goal.

- Sensor characterization work is far from enough, many other parameters that may affect sensor's performance still need to be tuned; these parameters include

concentration and amount of doping materials, sintering temperature and sintering time of gas sensing thin film, thin film geometry and sensor working temperature etc.

- There are still a lot of works to do to develop an Electric Nose system including hardware implementation and data processing. Hardware implementation will be focused on DSP based circuit design which includes A/D converter, D/A converter, Amplifier, power supply, display and communication. The finalized algorithm will be burned into DSP build in ROM in hardware realization. Data processing will be focused on improvement of fuzzy neural network algorithm. Besides TSK FNN, other neural network models or Fuzzy neural network models are worthy further examining. More systematic gas test experiments are also needed for training and model evaluation of TSK Fuzzy Neural Network.

# APPENDIX A
# LIST OF PUBLICATIONS

***Journal***

Jian-Wei Gong, Quan-Fang Chen, Ming-Ren Lian, Nen-Chin Liu, Roberts G. Stevenson and Fatos Adami, "Micromachined Nanocrystalline Silver doped SnO2 H2S Sensor", Sensors and Actuators B, Accepted. 2005

Jian-Wei Gong, Quan-Fang Chen, Ming-Ren Lian, Nen-Chin Liu, Claude Daoust, "Temperature Feedback Control for Improving Stability of SMO (Semiconductor Metal Oxide) Gas Sensor", IEEE Sensors Journal, In Press 2005.

Jianwei Gong, Quanfang Chen, Weifeng Fei, and Sudipta Seal, "Micromachined Nanocrystalline SnO2 Chemical Gas Sensors for Electric Nose", Sensors and Actuators B: Chemical, Volume 102, Issue 1, 1 September 2004, Pages 117-125

Jianwei Gong and Quanfang Chen, "Novel Nanocomposite MEMS based chemical sensors with Single Walled Carbon Nanotube and Sol-gel SnO2", Nano Letters, In View

Jian-Wei Gong, Quan-Fang Chen, Ming-Ren Lian, Nen-Chin Liu, "Environmental Influences on SMO Sensors' Performance", Sensors and Transducers, In View

***Conference***

Jianwei Gong, Quanfang Chen, Ming-Ren Lian, Nen-Chin Liu, "Micromachined Nanocrystalline Silver doped SnO2 H2S Sensor", 2005 NSTI Nanotechnology Conference and Trade Show, Anaheim, California, U.S.A. May 8-12 2005

Jianwei Gong and Quanfang Chen, "Sol-Gel Prepared Single Wall Carbon Nanotube SnO2 Thin Film for Micromachined Gas Sensor", Technical Proceedings of the 2004 Nanotechnology Conference and Trade Show, Volume 3 (Nanotech 2004 Vol. 3), Boston, March 7-11, 2004, pp 232 - 235

Jianwei Gong , Weifeng Fei, Sudipta Seal, Quanfang Chen, "Nanocrystalline SMO Thin Films Prepared by Sol Gel Process for MEMS Based Hydrogen Sensor", SPIE Photonics West 2004/Micromachining and Microfabrication, San Jose, California USA, 25-29 January 2004

Jianwei Gong, Weifeng Fei, Zheng Xia, Quanfang Chen, Sudipta Seal, Louis C. Chow, "Development of Micromachined Nanocrystalline Mesoporous SnO2 Gas Sensor for Electric Nose", IEEE Sensors 2003 Toronto, Canada, October 22-24, 2003.

Quanfang Chen, Bo Li, Jianwei Gong, Min Hu, Robust microvalves for hydraulic actuators, SPIE Photonics West 2003: Micromachining and Microfabrication, 25 - 31 January 2003, San Jose, California USA

# APPENDIX B
# LIST OF PATENTS

Jian-Wei Gong, Quan-Fang Chen, Ming-Ren Lian, Nen-Chin Liu, Claude Daoust,, Temperature Feedback Control for Solid State Gas Sensor. U.S. Patent Application No. 11/074,385

# APPENDIX C
# RESEARCH FACILITIES

Laurell™ Programmable Spin Processor

Quintel™ mask aligner

Bausch & Lomb™ MicroZoom® microscope

Olympus™ BH2umA microscope

Agliant™ programmable power supply

Tektronix ™ TDS 224 oscilloscope

Gas testing system (gas chamber, Omega™ 2cc mass flow controller, National Instrument™ data acquisition interface etc.)

Photolithography and Wafer Handling: Karl Suss™ Mask Aligner; Photoresist spinners; Blue M ™ Ovens; Gas cabinets; Wire saw machine; Two furnaces for diffusion (boron and phosphorous) and two Oxidation furnaces (dry and wet); Hydrogen, argon and nitrogen annealing furnace.

Thin Film Deposition Equipment: Multi station, multi source, Cryo™ pumped vacuum system; Edward evaporation system; D.C. magnetron sputtering gun; R.F. magnetron sputtering gun; Reactive Ion Etching System (Drytek™); Plasma Enhanced Chemical Vapor deposition (PECVD) System; Electron beam evaporation system with 4 crucible Turret; Ion Milling.

Analytical and Test Equipment: HP semiconductor parameter analyzer; HP network analyzer; Four point probe sheet resistivity; Micro Manipulator probe stations; Thin film thickness measuring interferometer; Ultrasonic wire bonder;; DekTak™

Profilometer; Laser Scriber; Photomask Designing Capability; Metallurgical microscope with DIC and TV monitor (Nikon); Scanning Electron Microscope (JEOL™).

# .LIST OF REFERENCES


1. Marc Madou, Fundamentals of Microfabrication, 2nd Edition, CRC, 2002.

2. Gregory Kovacs, Micromachined Transducers Sourcebook, McGraw-Hill, 1998.

3. Nadim Maluf, An Introduction to Microelectromechanical Systems Engineering, Artech House, 2000

4. Stephen Senturia, Microsystem Design, Kluwer, 2001.

5. http://www.imtek.de/simulation/benchmark/wb/38868/DiplomaThesisHildenbrand.pdf

6. Stetter, J. and Penrose, W., 2002, Sensors Update, Vol 10 189-229

7. Gardner, J. W. 1991, Sensors and Actuators B, vol. 4, pp 109-115.

8. Nakamoto, T. and Moriizumi T., 1988, IEEE Ultrasonics Symposium, 613-616

9. Nakamoto, T. at al, 1993, Sensors and Actuators B, 10 85- 90

10. Kraus P. R. et al, 2001, Sicon'01 Sensors for Industry Conference, Rosemount, Illinois, USA 5-7 November 2001

11. Kurosawa, S. et al., 2001, 2001 IEEE International Frequency Control Symposium and PDA exhibition

12. D'Amico, A., et al., 1982, Applied. Physics. Letter. 41 300,

13. D'Amico, A., et al., 2nd Int. Meeting on Chemical Sensors (Bordeaux) p 7431985

14. Caliendo, C., et al., IEEE Ultrasonic Symposium Proceedings (Chicago, IL, 1988) (New York: IEEE) p 569

15. Simone, H., 2002, $SnO_2$ thick film sensors at ultimate limits: Performance at low $O_2$ and $H_2O$ concentrations; Size reduction by CMOS technology, Dissertation.

16. Haugen, J. E. and Kvaal, K., 1998, Electronic Nose and Artificial Neural Network, Meat Science, Volume 49, Supplement 1, 1998, Pages S273-S286

17. Siyama, T., et al., 1962, Anal. Chem. 34 1502-1503.

18. N. Taguichi, 1962, Japan. Patent 45-38200

19. Mielle, P. and Marquis, F., 2000, Sensors and Actuators B 68 9–16

20. Lee, D. D. and Lee, D. S., 2001, IEEE Sensors Journal, Vol.1, No. 3

21. Lim, J. W., et al, 2001, Sensors and Actuators B, 77 pp 139-144

22. Najafi, N. et al., 1994, IEEE transactions on electron devices, Vol. 41 No. 10

23. Yan, G.Z. at al., 2002, Proceeding of the first IEEE Sensors Conference, Orlando, Florida, USA.

24. Moseley P., Norris, J. and Williams, D., 1991, Techniques and mechanisms in gas sensing, Bristol, Adam Hilger

25. Figaro Technique Manual, 1998, General Information for TGS Sensors, p. 2

26. Schierbaum, K. et al., 1990, Sensors and Actuators B 2 71-78.

27. Wide, P., et al., 1998, IEEE Transactions on Instrumentation and Measurement, Vol. 47, No. 5

28. Kappler, J., 2001, Characterization of high-performance $SnO_2$ gas sensors for CO detection by in situ techniques, PhD Thesis, University of Tubigen, Shaker Verlag (D) ISBN3-8365-9040-6

29. Schweizer-Berberich, M., 1998, Gas sensors based on stannic oxide, PhD Thesis, University of Tubigen, Shaker Verlag (D) ISBN3-8265-4182-0

30. Yamazoe, N., 1991, Sensors and Acutuators B, 5 P.7-19

31. Matsushima, S., 1992, Sensors and Actuators B, 9 p.71-78

32. Lee, D. D., 1987, Sensors and Actuators B, 12 p.441-447

33. Hubner, H.P., 1989, Sensors and Actuators B, 17 p.351-354

34. Maeda, M., 1993, Japanese Journal of Applied Physics Pat1-Regular Papers Short Notes & Review Papers 32 p. 4136-4140

35. Yoon, K. H., 1995, Journal of Materials Science, 30 p.3415-3420

36. Xu, C., 1991, Sensors and Actuators B, 3 p.147-155

37. Mizsei, J., 1993, Sensors and Actuators B, 15-16 p.328-333

38. Barsan, N., et al., 1999, Anal. Chem 365 287–304

39. Milton Ohring, Materials Science of Thin Films, second edition, Academic Press, ISBN: 0-12-524975-6, 2002

40. Maissel L. I. and Glang R., Handbook of Thin Film Technology, McGraw-Hill, ISBN 07-039742-2, 1970

41. Gurlo, A. et al., 1997, Thin Solid Films 307 288

42. Sakai, G., et al., Sensors and Actuators B 77 (2001) 116-121

43. Diéguez, A., et al., 1999, *Structural analysis for the improvement of SnO2-based gas sensors*, Ph.D. Thesis, Universitat de Barcelona

44. Capone, S. et al., 2001, Thin Solid Films 391 314

45. Klein, L., 1988, Sol-gel technology for thin films, fibers, preforms, electronics, and speciality shapes, Part II, Park Ridges, NJ.

46. Park, S. S. and Mackenzie, J.D., 1996, Thin Solid Films, 274 154-159.

47. Sakai, G. et al., 2001, Sensors and Actuators B 77

48. Seal, S. and Shukla, S., 2002, JOM 54 (9) 35-38,60.

49. Jarzebski, Z. M., 1976, Journal of the Electrochemical Society, 123, Iss.7 p. 199-205

50. Barbarat, P., 1997, Journal of Material Chemistry, 7 (12) p. 2547-2550

51. Kittel, C., 1995, Introduction to solid state physics, 7th edition, New York: Wiley

52. Blakemore, J. S., 1985, Solid State Physics, 2nd ed. Cambridge, England: Cambridge University Press

53. Fonstad, C. G. and Rediker, R. H., 1971, Journal of Applied Physics, 42 p.2911-2918

54. Samson, S. and Fonstad C. G., 1973, Journal of Applied Physics, 44 p. 4618-4621

55. Barsan, N. and Weimar, U., 2001, Journal of Electroceramics, Volume 7, Issue 3, 143-167

56. Barsan, N., 1994, Sensors and Actuators B, 17, P. 241

57. Miiller, R. and Lange, E. 1986, Sensors and Actuators, 9 39.

58. Martens, H. and Naes, T., *Multivariate Calibration*, J. Wiley & Sons, Chich-ester, 1989.

59. Weimar, U. et al, 1990, Sensors and Actuators, Bl 93-96

60 Corcoran, P. and Lowery, P., Neural processing in an electronic odor sensing system, Fourth International Conference on Artificial Neural Networks“, Cambridge 1995, IEE. London 1995, p. 415-420

61 Hong, H. K. et al., 1996, Sensors and Actuators B 33 68-71

62. Sundic, T., et al., 2003, Chemometrics and Intelligent Laboratory Systems 64 103–122

63. Oliveros, C. C. et al., 2002, Analytica Chimica Acta, Volume 459, Issue 2, 22 May 2002, Pages 219-228

64. Huyberechts, G. et al., 1997, Industrial Electronics, 1997. ISIE '97., Proceedings of the IEEE International Symposium on ,Volume: 1 , 7-11 July 1997 Pages:SS134 - SS139 vol.1

65. Osowski, S. and Brudzewskil, K., 1999, Hybrid neural network for gas analysis measuring system, in IMTC 99, Venice, Italy, 1999.

66. Medsker, L.R, 1995, Hybrid Intelligent Systems, Kluwer Academic Publishers, USA

67. Lin, C.T, 1994, Neural fuzzy control systems structure and parameter learning, World Scientific Co. Ltd

68. Osowski, S. and Brudzewskil, K., 2000, IEEE Transactions on Instrumentation and Measurement, Vol. 49, No. 2, April 2000

69. Osowski, S., 2001, Metrologia i systemy pomiarowe, vol. 8, No. 1, pp. 3-23.

70. Yen, J. et al., 1998, IEEE Transactions on Fuzzy Systems, Vol. 6, No. 4.

71. Cordon, O. and Herrera, F., 1999, IEEE Transactions on System, Man, and Cybernetics B: Cybernetics, Vol. 29, No. 6.

72. Lee, W.J., et al., 2002, FUZZ-IEEE'02, Proceedings of the 2002 IEEE International Conference on fuzzy systems, vol. pp.1174 -1179.

73. Ouyang, C.S. and Lee, S. 2001, Proceedings of International Fuzzy System Association World Congress, pp. 787-791.

74. Simon, I. et al, Sensors and Actuators B 73 1-26 (2001)

75. Meixner, H. and Lampe, U., Sensors and Actuators B 33, 198 (1996)

76. Gardner, J.W. et al., 1990, Measurement Science and Technology, vol. 1

77. Gardner, J. W. 1994, A brief history of electronic noses, Sensors and Actuators 8, 18-19 pp 211-220 211

78. Stetter, J.R., et al., Sensors and Actuators B 69 410–419

79. Chou, J., Hazardous Gas Monitors, McGraw-Hill Book Company, New York, ISBN 0-07-135876-5

80. www.epa.gov

81. Zee, F. and Judy, J. W., 2001, Sensors and Actuators B 72 120-128

82. Lee D. S. et al., 2000, Sensors and Actuators B 71 90-98

83. Marquis, B. T. and Vetelino, J. F., 2001, Sensors and Actuators B: Chemical, Volume 77, Issues 1-2, 15, Pages 100-110

84. Pisanelli, A. M., et al., 1994, Life Chemistry Reports, vol. 11, pp. 303-308.

85. Rebecca C. Young, et al., 2000, Sensors and Actuators B: Chemical, Volume 93, Issues 1-3, 1 August 2003, Pages 7-16

86. Nakamoto, T. at al, 1992, Sensors and Actuators B, 8 181-186

87. Haugen, J. E. and Kvaal, K. 1998, Meat. Science Vol. 49, No. Suppl. 1, S273-S286

88. McEntegart, C. M. et al., 2000, Sensors and Actuators B 70 170–176

89. Penza, M. et al., 2001, Sensors and Actuators B 81 115-121

90. Kalman E. L. et al., 2000, Analytica Chimica Acta 403 31–38

91. Morvan, M. et al., 2000, Sensors and Actuators B 69 384–388

92. Gardner J. W. and Persaud K. C. 2000, Electronic Noses and Olfaction, IOP Publishing Ltd. Bristol ISBN 0-7503-0764-1

93. Schierbaum, K.D., et al., 1993, Sensors and Actuators, B 1314 143–147.

94. Capone, S. et al., 2000, Sensors and Actuators B 69 230–235

95. Chambon, L. et al, 1999, Sensors and Actuators B 60 138–147

96. Gardner, J. W., Microsensors—Principles and Applications, John Wiley & Sons Ltd. ISBN 0-471-94135-2; 0-471-94136-0

97. Hatfield, J.V. et al., 1994, Sensors and Actuators B, 18-19 pp 221-228 221

98. Williams, D. E., 1999, Semiconducting oxides as gas-sensitivities resistors, Sensors and Actuators B 57 pp1-16

99. Sberveglieri, G. et al., 1999, Recent Progress on Gas Sensors Based on Semiconducting Thin Films, 0-7803-4513-4/99, IEEE

100. Henkel, K., 2001, micro hotplate sensors, http://www.physik.tucottbus.de/physik/ap2/hotplate.pdf

101. Ho, C. K. et al., 2001, Review of Chemical Sensors for In-Situ Monitoring of Volatile Contaminants, SANDIA REPORT, SAND2001-0643

102. Hunter, G. W. et al., 1998, IEEE, 0-7803-5086-3

103. Jang, E. T. and Chung, W. Y. 2002, Proceedings of IEEE Sensors 2002, Orlando, Florida

104. Johnson, C.L. et al., 1994, Sensors and Actuators B 20 55-62

105. Gong, J. W., et al., Sensors and Actuators B: Chemical, Volume 102, Issue 1, 1 September 2004, Pages 117-125

106. Choi, W.K. et al., 1997, Sensors and Actuators B 40 21

107. Gopel, W. and Schierbaum, K. D. 1995, Sensors and Actuators B 26-27 1-12

108. Chaudhary, V.A., et al., Sensors and Actuators B 55 (1999) 154–160

109. Hyodo, T. et al, 2003, Sensors and Actuators B 93 590–600

110. Yamaura, H. et al, 1996, Sensors and Actuators B 35-36 325-332

111. Gong, J. et al, SPIE Photonics West 2004/Micromachining and Microfabrication, San Jose, California USA, 25-29 January 2004

112. Matko, I. et al., 1999, Sensors and Actuators B, 59, 210-215

113. Tournier, G. et al., 1995, Sensors and Actuators B 26. 24-28

114. More, P.S. et al., 2003, Materials Letters 57 2177– 2184

115. Baraton, M.I. et al., 2002, Materials Science and Engineering C 19 315–321

116. Ivanovskaya, M. et al, 2000, Sensors and Actuators B 68 344–350

117. Esfandyarpour B. et al., IEEE Sensors Journal, Vol. 4, No. 4, AUGUST 2004

118. Maekawa, T., et al., 1994, J. Mater. Chem. **4,** 1259

119. Yoo D. J., et al., 1995, Jpn. J. Appl. Phys. **34,** L455

120. Chowdhuri, A. et al., IEEE sensors 2002, June Orlando, FL, USA

121. Zhou, X., et al., Materials Science and Engineering B99 (2003) 44 - 47

122. Liu, C. H., et al, 1997, Thin Solid Films 304 13-15

123. Tao, W.H. and Tsai, C.H.,2002, Sensors and Actuators B 81, 237-247

124. Penza, M., et al., 2001, Sensors and Actuators B 81, Issue 1, 15 115-121

125. Solis, J. L. et al., 2001, Sensors and Actuators B 77, Issues 1-2, 15 316-321

126. Antonik, M. D. et al., 1995, Thin Solid Films, 256, Issues 1-2, 1 247-252

127. Zhang, G. and Liu, M., 2000, Sensors and Actuators B 69 144-152.

128. Santos, J. et al., 1997, Sensors and Actuators B 43 154–160

129. Jiménez, I. et al., 2002, IEEE Sensors Journal , 2 (4), 329-335

130. National Instruments, LabVIEW Support, http://www.ni.com/support/lvsupp.htm

131. Bishop, R. H., 2001, Learning with LabVIEW 6i, 2nd Edition, Addison-Wesley.

132. Götz, A. et al., 1997, *J.* Micromech. Microeng. **7**, pp. 247–249

133. Rossi, C., et al., 1997, Sensors and. Actuators A **63**, pp. 183–189

134. Mo, Y., et al., 2001, Sensors and Actuators B: Chemical, Volume 79, Issues 2-3, pp. 175-181

135. Lee, S. M., et al., 2003, Microelectronics Journal 34, pp115-126, 2003

136. Friedberger, A., et al., 2003, Sensors and Actuators B 93, pp.345–349, 2003

137. Jaeger, R.C., Introduction to Microelectronic Fabrication, Second Edition, 2002, Prentice Hall

138. Weast, R. C., et al, *Handbook of Chemistry and Physics* , 66th Edition, CRC Press, INC. ISBN-0-8493-0466-0, 1985-1986, pp F-120

139. CRC Materials Science and Engineering Handbook, p.281

140. Sberveglieri, G. et al., Microsystem Technology. 3 (1997) 183-190.

141. Air Property Calculator, http://users.wpi.edu/~ierardi/FireTools/air_prop.html

142. http://www.engineeringtoolbox.com/19_156.html

143. Karlekar, B. V., and Desmond, R. M. Engineering Heat Transfer, West Publishing Co, 1977.

144. Mechanics of Materials, Beer and Johnson, McGraw-Hill, Second Edition, 1992

145. Esch, H., et al., 2000, Sensors and Actuators B: Chemical, Volume 65, Issues 1-3, pp.190-192

146. Figaro Technical Information Mamul for TGS203, http://www.figarosensor.com/.

147. Sheng, J., et al, 1997, Sensors and Actuators B: Chemical, Volume 41, Issues 1-3, pp131-136

148. Capteur Technical Information for G Series Low Power GL07 Carbon Monoxide Sensor, http://www.investigacion.frc.utn.edu.ar/sensores/gases/gl07.pdf

149. Singh, D. W., 2001, Semiconductor Devices: Basic Principles, Wiley, ISBN 0-417-36245-X.

150. Gong, J. W., et al., Temperature Feedback Control for Improving Stability of SMO (Semiconductor Metal Oxide) Gas Sensor, patent pending.

151. Williams, D.E., et al., Solid State Gas Sensors, Chapter. 5.1, Adam Hilger IOP, Publishing, 1987, 71

152 Ihokura, K. and Watson, J., The Stanic Oxide Gas Sensor, CRC Press, Boca Raton, FL, 1994

153. Gallardo, I. J., "Tungsten oxide nanocrystalline powders for gas sensing applications", PhD Dissertation, Barcelona, June, 2003

154. Madou, M. J. and Morisson, S. R., Chemical Sensing and Solid State Devices, Academic Press, New York, 1989 p. 493

155 Kuse, T. and Takahashi, S., Sensors and Actuators, B 67 (2000) 36–42

156 Jiménez, I. et al., Sensors and Actuators B 93 (2003) 475–485

157 Ling, Z. and Leach, C., Sensors and Actuators B 102 (2004) 102–106

158 Ionescu, R. et al., Sensor and Actuators, B 61 (1999) 39–42

159. Kohl, D, 1989, Sensors and Actuators B18 71–113

160. Yannopoulos, L. N., Sensors and Actuators, Volume 12, Issue 1, July 1987, Pages 77-89

161. Bârsan, N. and Ionescu, R., Sensors and Actuators B: Chemical, V.12, Issue 1, 15 March 1993, Pages 71-75

162. Miremadi, B. K. and Colbow, K.,1998, Sensors and Actuators B46 30–34

163. Arya, S. P. S. et al., 1988, Thin Solid Films, Volume 157, Issue 1, 15, Pages 169-174

164. Ansari, Z. A. et al, 2002, Sensors and Actuators B 87 105–114

165. Roland, P. et al., 2001, Proceedings of the 2001 DOE Hydrogen Program review NREL/ CP-570-30535

166. K. Wada and M. Egashira, 2000, Sensors and Actuators B 62 211

167. Gaidi, M. et al, 2000, Sensor and Actuators B 62 43

168. Ansari, S. G. et al, 1997, Thin Solid Films 295 (1–2) 271–276

169. Blaser, G., et al., 1999, Physics A 266 218-223

170. Bai, N. S., et al, 2000, Sensors and Actuators B 63, 74

171. Shukla, S. and Seal, S., 2003, Encyclopedia of Nanoscience and Nanotechnology, edited by H. S. Nalwa (American Scientific Publishers, Stevenson Ranch, California)

172. Penza, M. et al., 2001, Sensors and Actuators B 81 115-121

173. Hammond, J. W. and Liu, C. C., 2001, Sensors and Actuators B 81, 25

174. Delph, C. et al., Sensors and Actuators B 59 1999 255–259

175. Geloven, P. V. et al., Sensors and Actuators B: Chemical, Volume 4, Issues 1-2, May 1991, Pages 185-188

176. Huyberechts, G. et al., Sensors and Actuators B 45 (1997) 123–130

177. Sensor Industry Developments and Trends, Sensor Business Digest, August 2004 http://www.sensorsmag.com/resources/

178. Bienfait, M. et al., 2000, Surface Science. 1–3 243–248

179. Kong, J. et al, 28 January 2000, VOL 287 SCIENCE

180. Ong, K.G., et al., 2002, IEEE Sensor Journal. 2 82–88

181. Gong, J. W., et al, October 22-24, 2003, IEEE Sensors 2003, Toronto, Canada

182. Gong, J. W. and Chen, Q., Technical Proceedings of the 2004 Nanotechnology Conference and Trade Show, Volume 3 (Nanotech 2004 Vol. 3), Boston, March 7-11, 2004, pp 232 - 235

183. Krupke et al., Separation of Metallic from Semiconducting Single-Walled Carbon Nanotubes, *Science* 2003 0: 10865341-0

184. Carpenter, G. et al., 1992, IEEE Trans. Neural Networks*, 3(5):698-712.*

185. Gong, J. W. and Chen, Q., Technical Proceedings of the 2004 Nanotechnology Conference and Trade Show, Volume 3 (Nanotech 2004 Vol. 3), Boston, March 7-11, 2004, pp 232 - 235